Observational signature of Black Hole (BH). BH mass determination

Lev Titarchuk

(University of Ferrara/ICRANET/NRL/GSFC/GMU)

TALK@7th Agile meeting, Rome, September 30 2009

X-ray Binary (artistic conception)

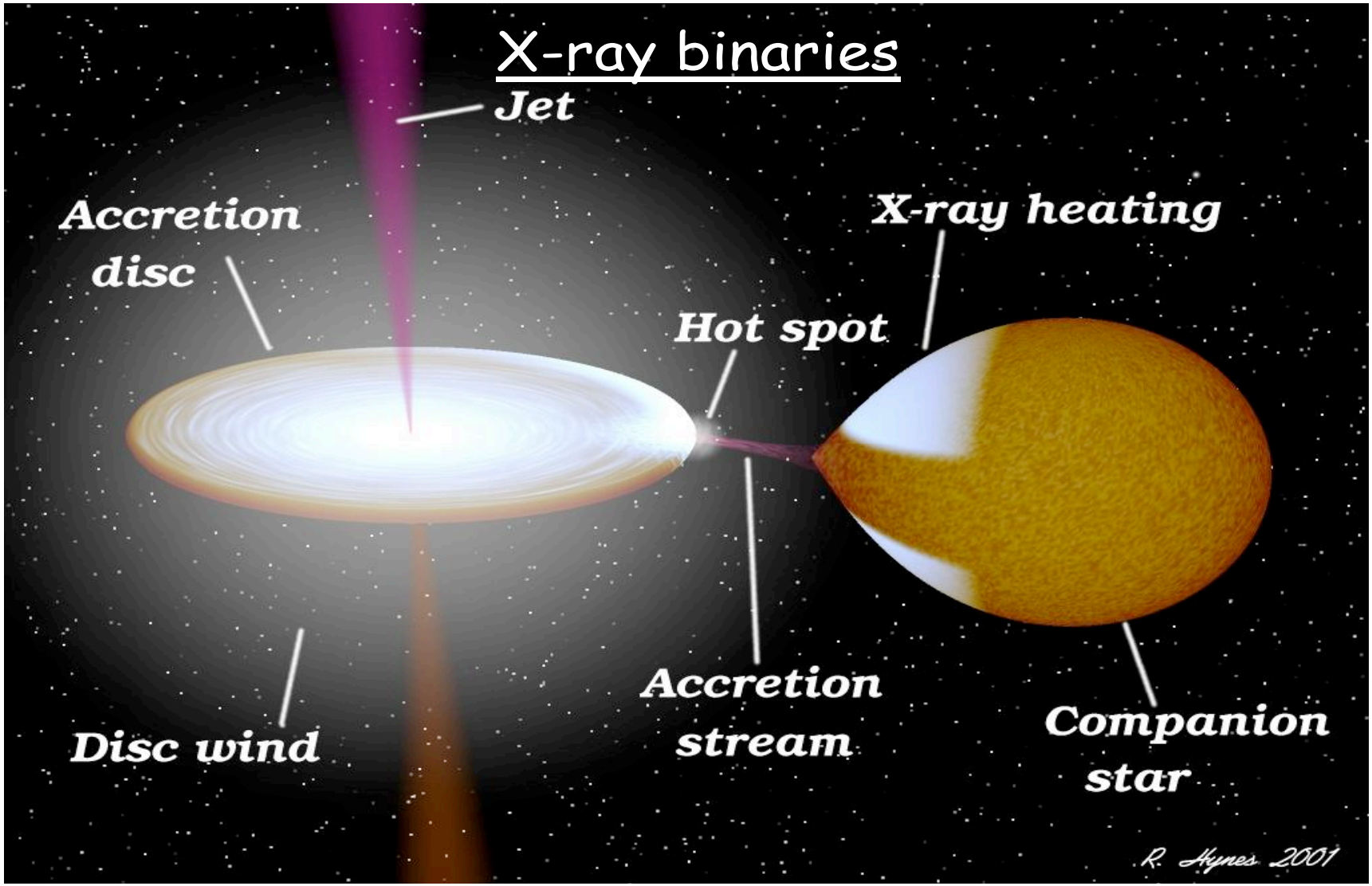

Model of Accretion Process Surrounding a Compact Object (NS or BH)

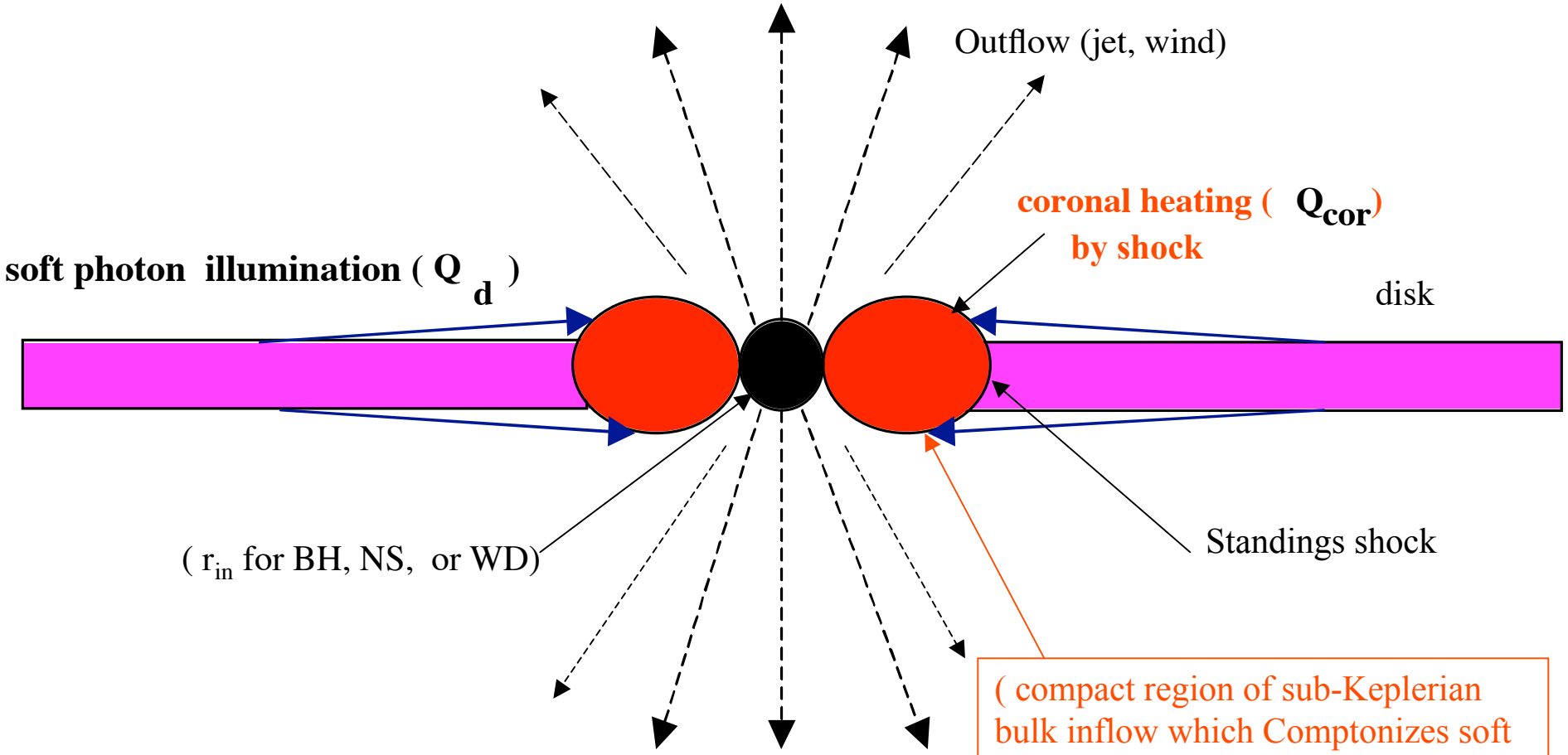

Composite spectrum of Cyg X-2

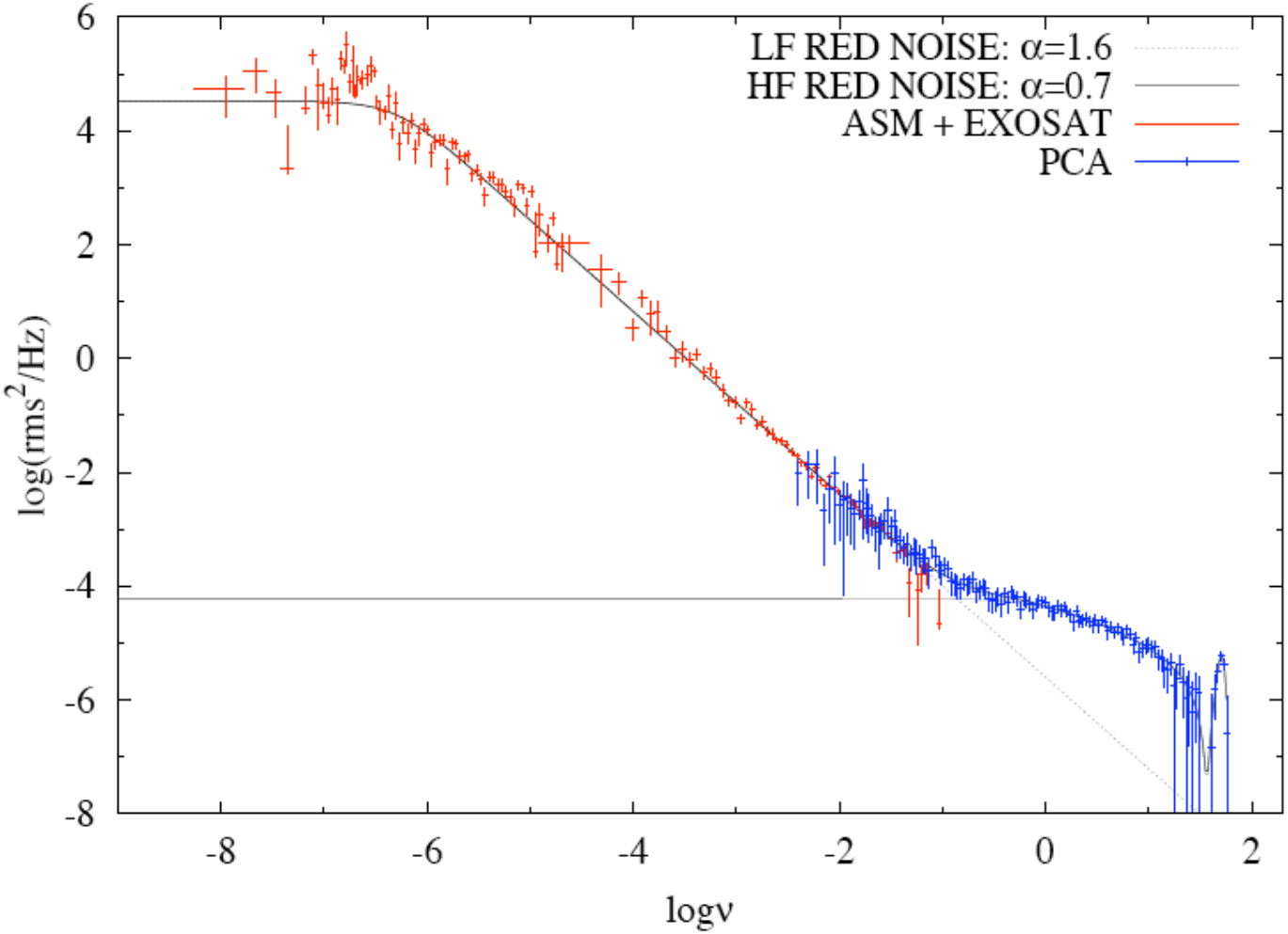

EXOSAT-ASM-PCA (RXTE) power spectrum of Cyg X-2 in frequency range that covers 10 orders of magnitude. One can clearly see low and high frequency (LF and HF) white-red noise components in PDS, related to the extended Keplerian disk and relatively compact, innner disk-like configuration (sub-Keplerian Compton corona) respectively. Each of these two components is perfectly fitted by our white-red noise model (dotted and solid lines are for LF and HF best-fit models respectively.

Soft state power spectrum of Cyg X-1

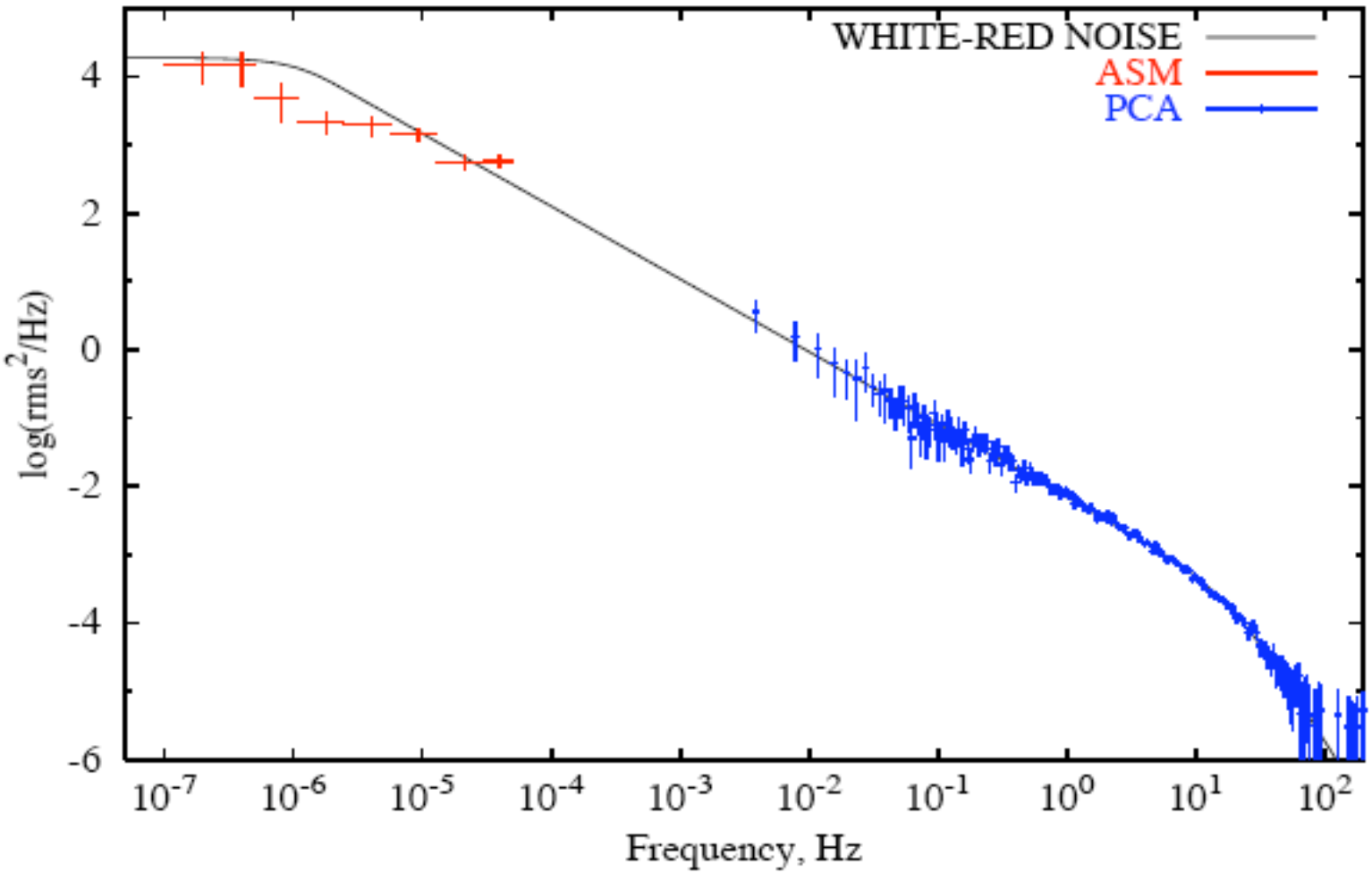

The composite soft state PDS is made by PCA (blue) and ASM (red) PDSs.
The PCA PDS is for ObsID 50110-01-52-00. Data are fitted by LF-HF diffusion model:
χ_2/N_{dof} = 184/228 = 0.81, the best -fit parameters $t_{0,D} = (6 \pm 1.7) \times 10^5$ s, $\psi_D = 2.93 \pm 0.01$.

LF QPOs in Black Holes

Cygnus X-1

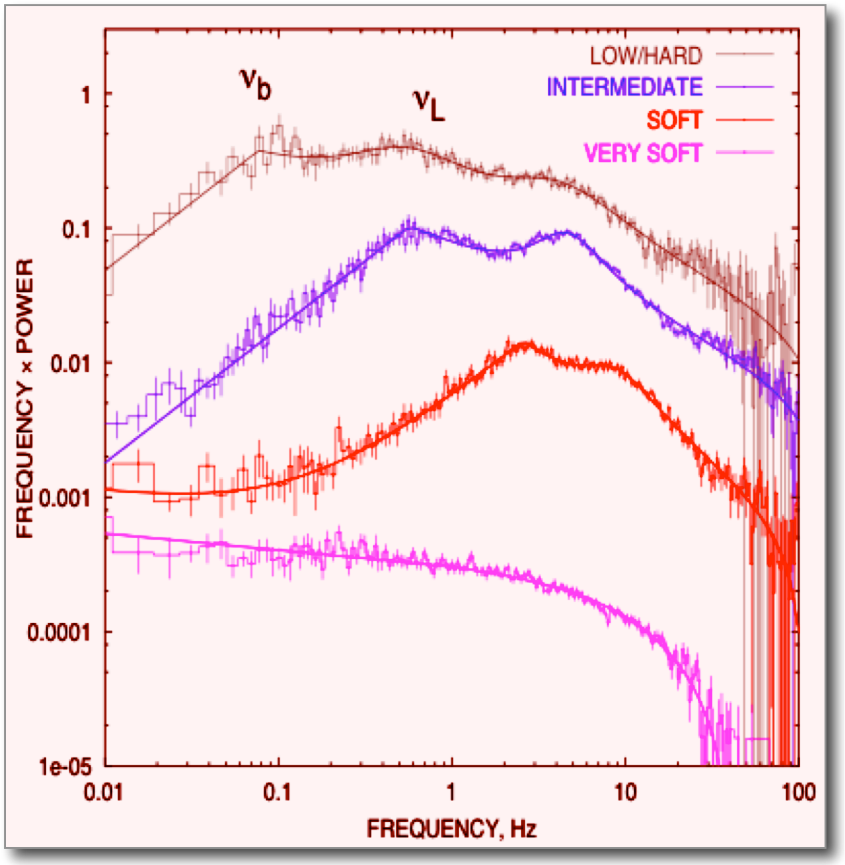

Shaposhnikov & T 2006, ApJ, 643,1098

GRO J1655-40

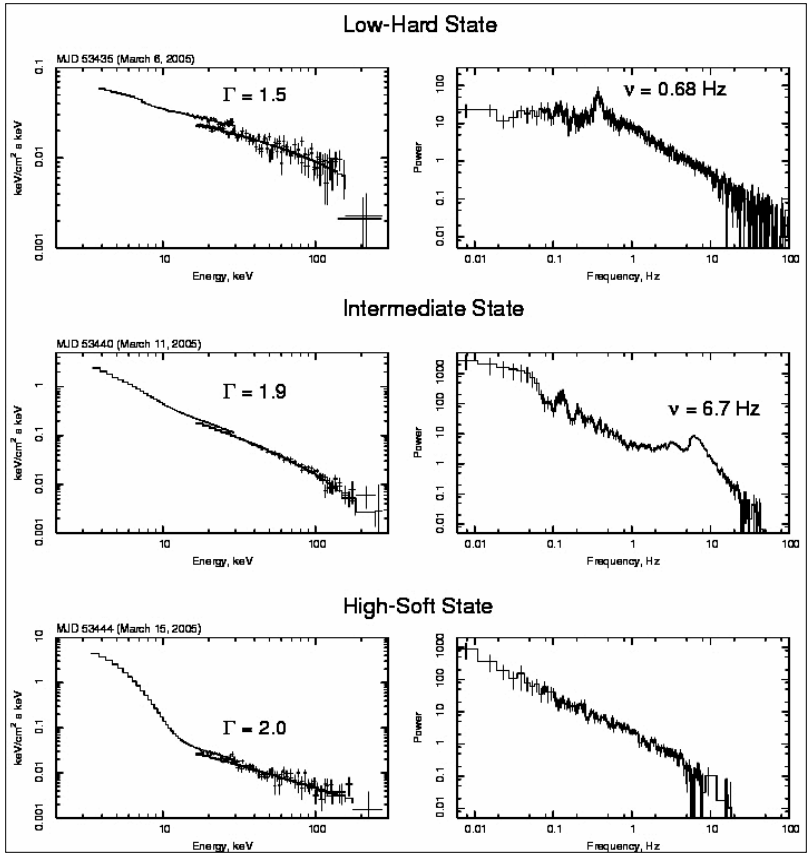

(**Shaposhnikov**, Swank, Rupen, Shrader, Beckmann, Markwardt & Smith 2007, ApJ, 655,434)

Spectral index of the converging inflow spectrum

- Main idea of the power law formation:

$$I_\nu \propto p^\kappa ,$$

where p is a probability of single scattering .

$$\nu / \nu_0 = 1 + \eta,$$

after k scatterings

$$\nu_k / \nu_0 = (1+\eta)^k .$$

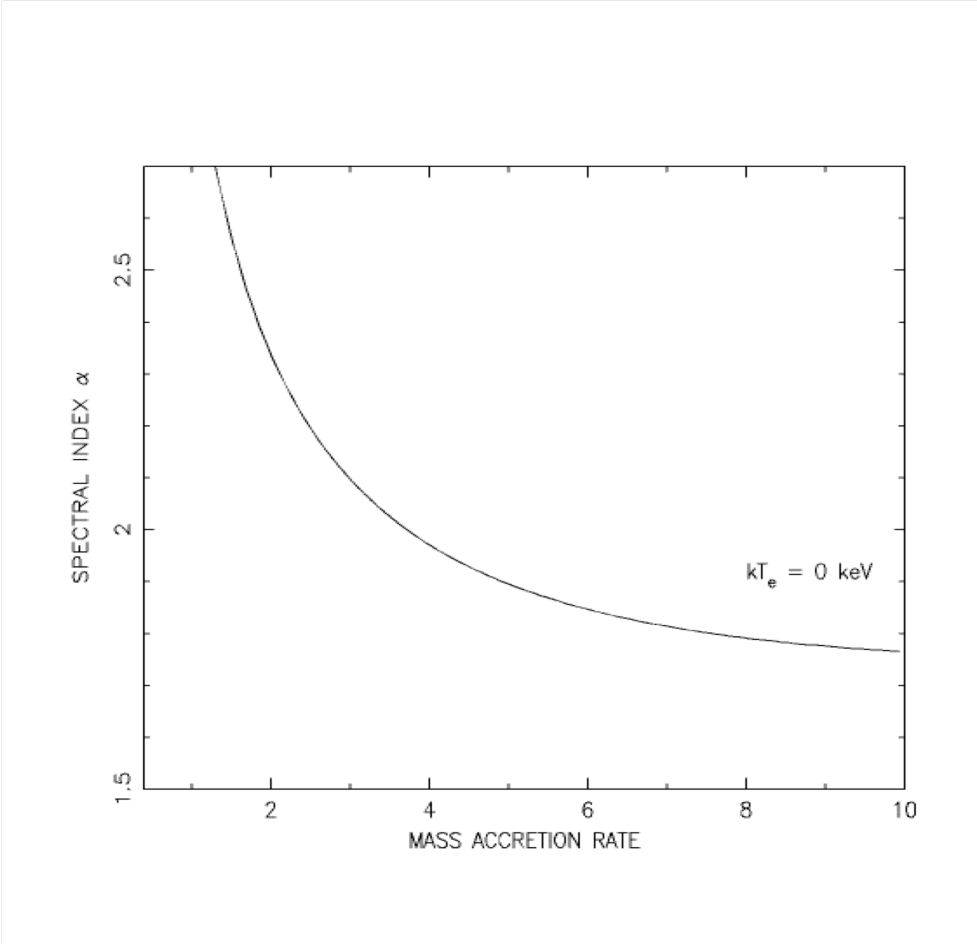

Thus $I = (\nu / \nu_o)^{-\alpha}$ where $\alpha = \ln(1/p)/\ln(1+\eta)$


ELSEVIER

Physica A 299 (2001) 213–221

PHYSICA A

www.elsevier.com/locate/physa

Exponential and power-law probability distributions of wealth and income in the United Kingdom and the United States

Adrian Drăgulescu, Victor M. Yakovenko*,[1]

Department of Physics, Center for Superconductivity Research, University of Maryland, College Park, MD 20742-4111, USA

Abstract

We present the data on wealth and income distributions in the United Kingdom, as well as on the income distributions in the individual states of the USA. In all of these data, we find that the great majority of population is described by an exponential distribution, whereas the high-end tail follows a power law. The distributions are characterized by a dimensional scale analogous to temperature. The values of temperature are determined for the UK and the USA, as well as for the individual states of the USA.

Exponential and power-law probability distributions of wealth and income in the United Kingdom and the United States

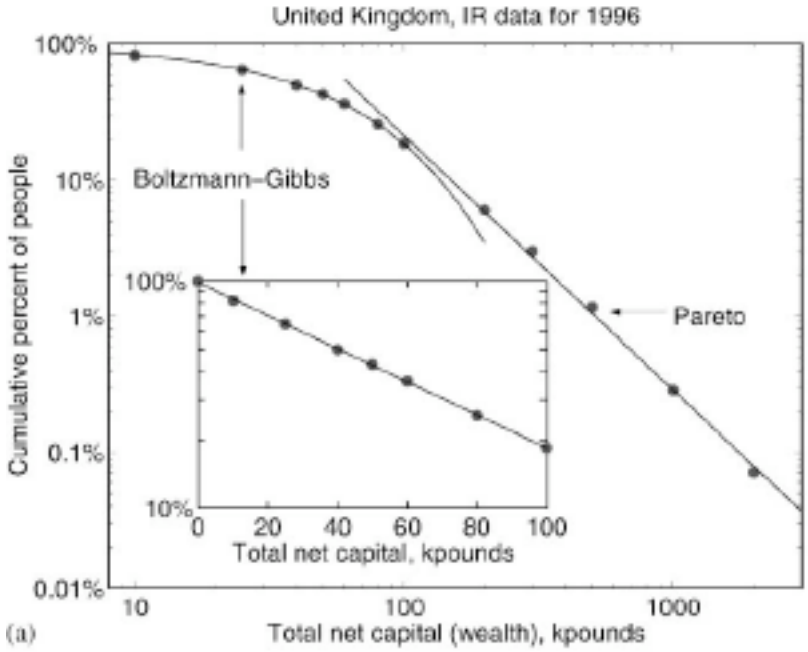

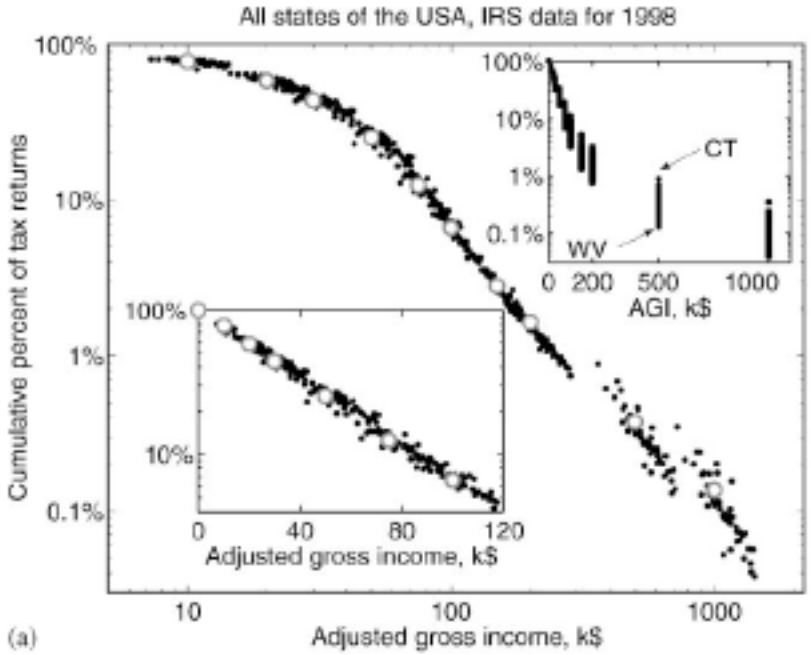

Dragulescu, & Yakovenko Physica A **299**, 213 (2001))

Simultaneous Power and energy spectra evolution

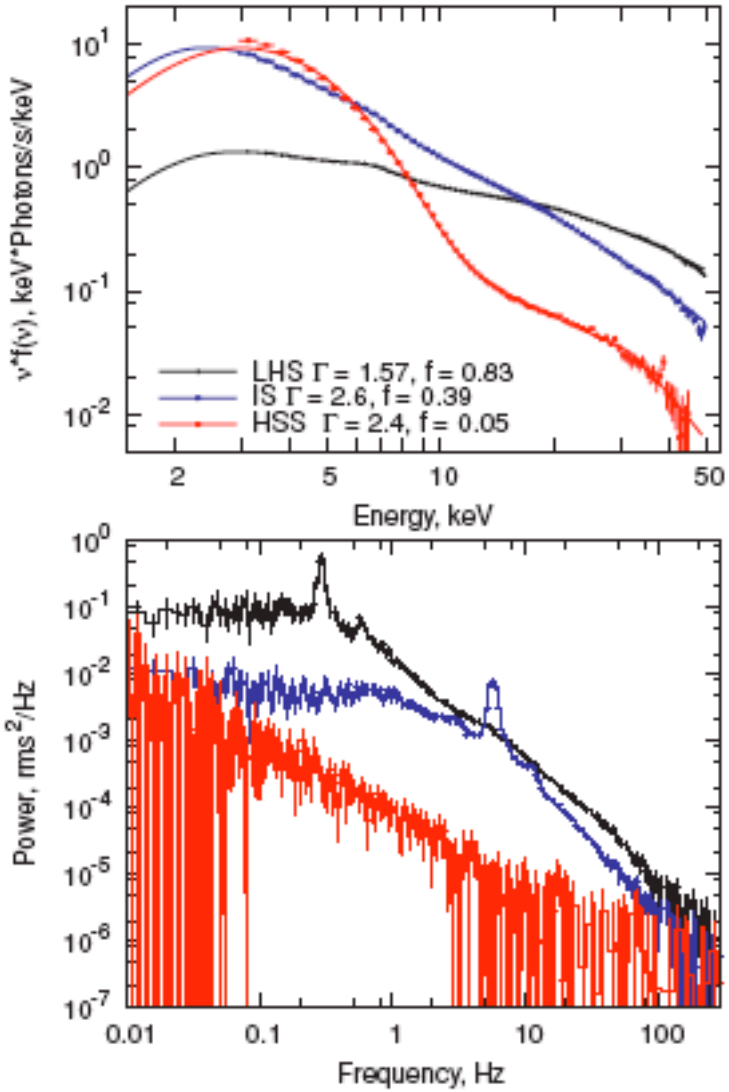

Figure 1. Three representative energy (top) and power (bottom) spectra during the rise part of the 1998 outburst of XTE J1550−564. Data are taken from *RXTE* observations 30188-06-01-00 (red), 30188-06-01-00 (blue), and 30191-01-05-00 (black). In the top panel, the solid curves correspond to the best-fit model spectra.

The inferred scenario of the spectral transition in Cyg X-1. Strength of disk and outflow (wind) increase towards the soft states

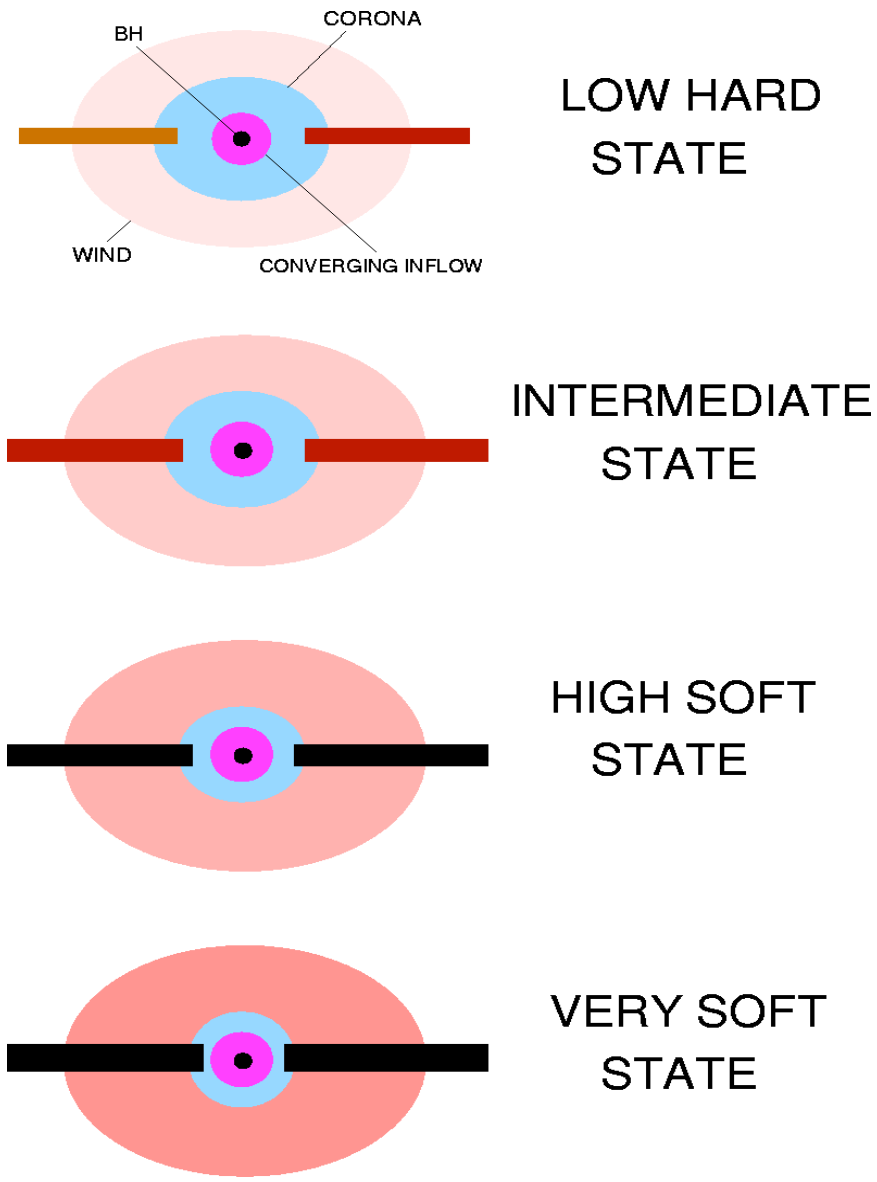

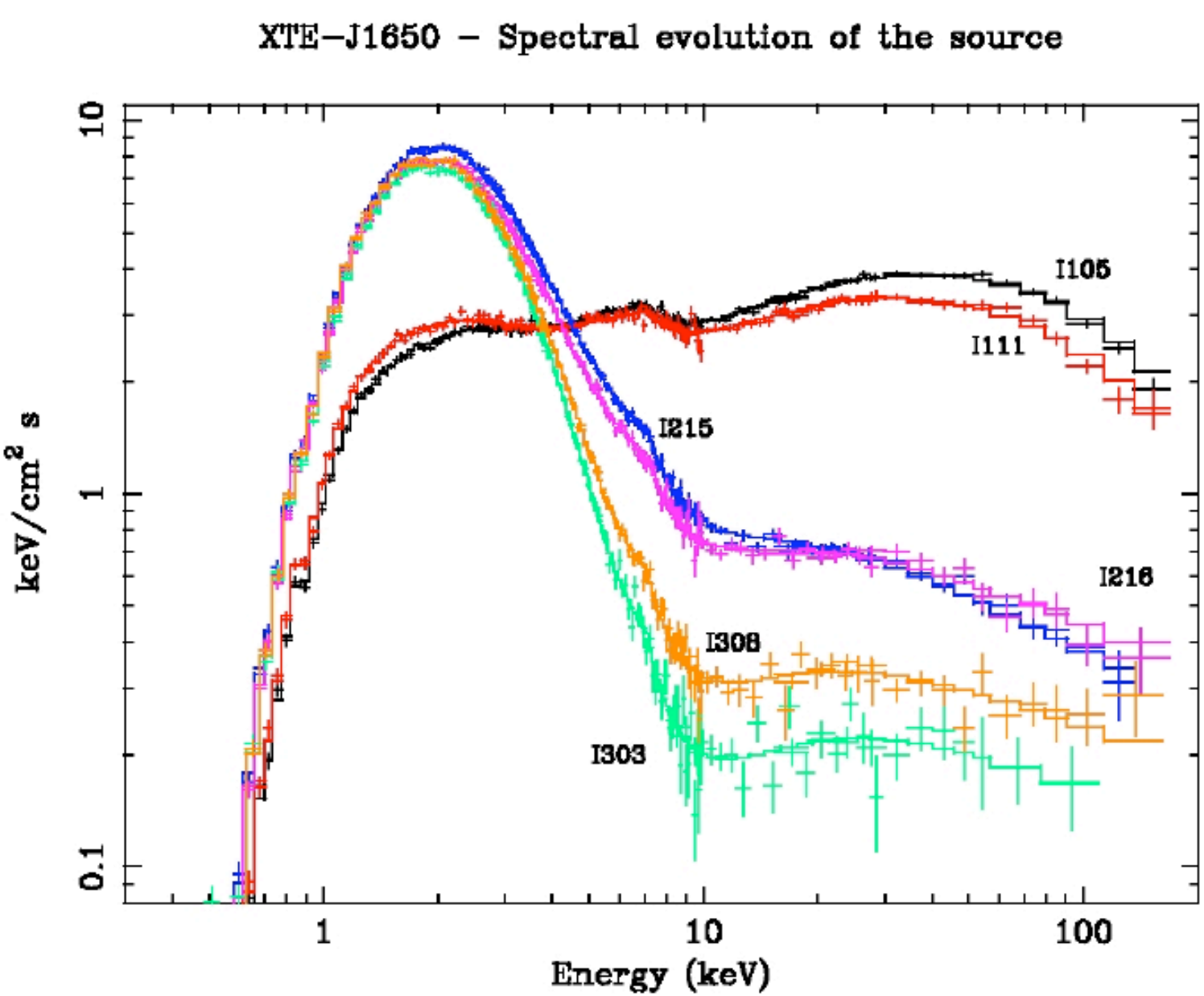

Montanari, T & Frontera 2006

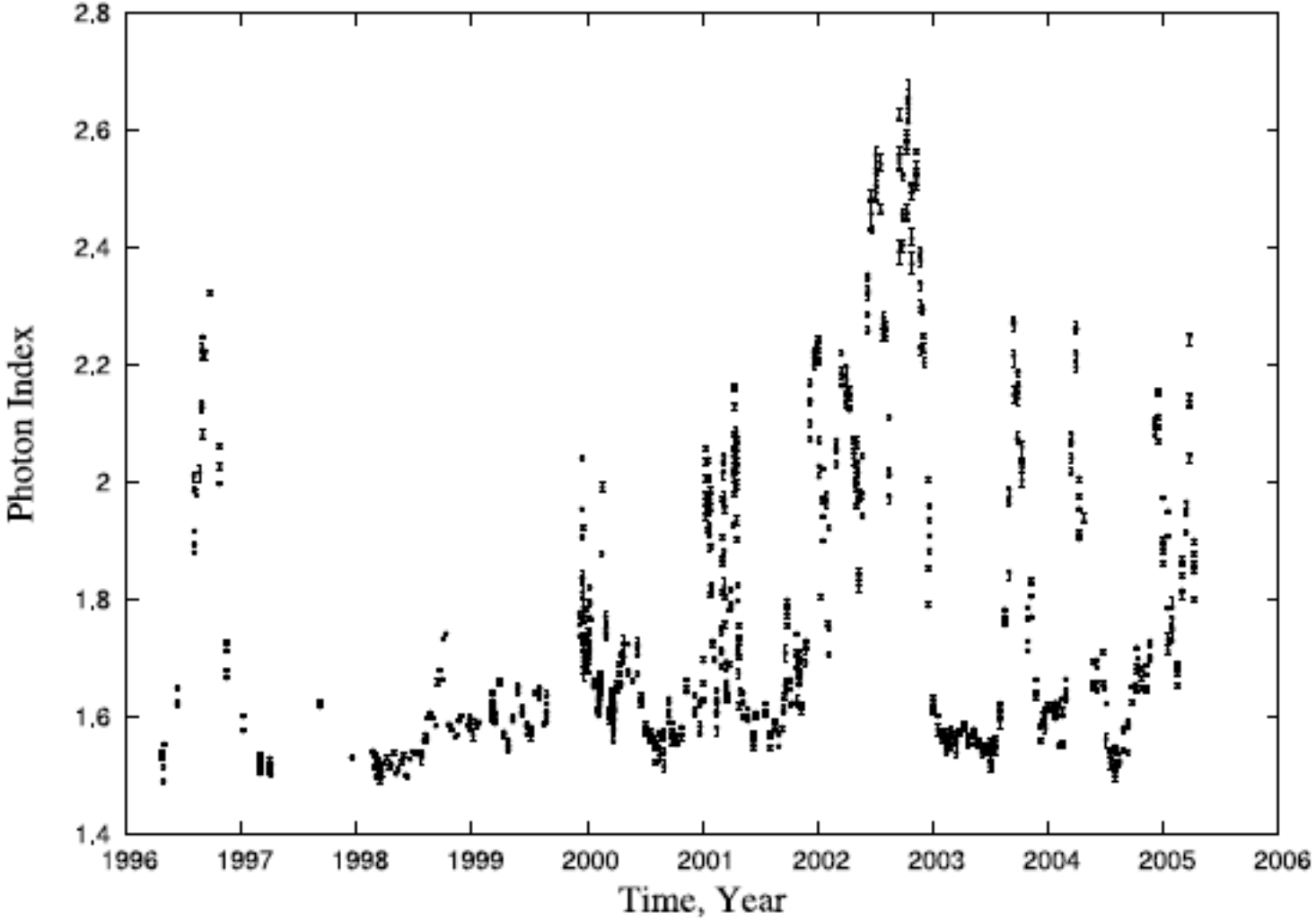

FIG. 15.—The variation of the photon index in Cyg X-1 throughout the entire *RXTE* mission.

PDS - harder part (blue) and softer part (red) of Hard State of XTE-J1650 (TOO1)

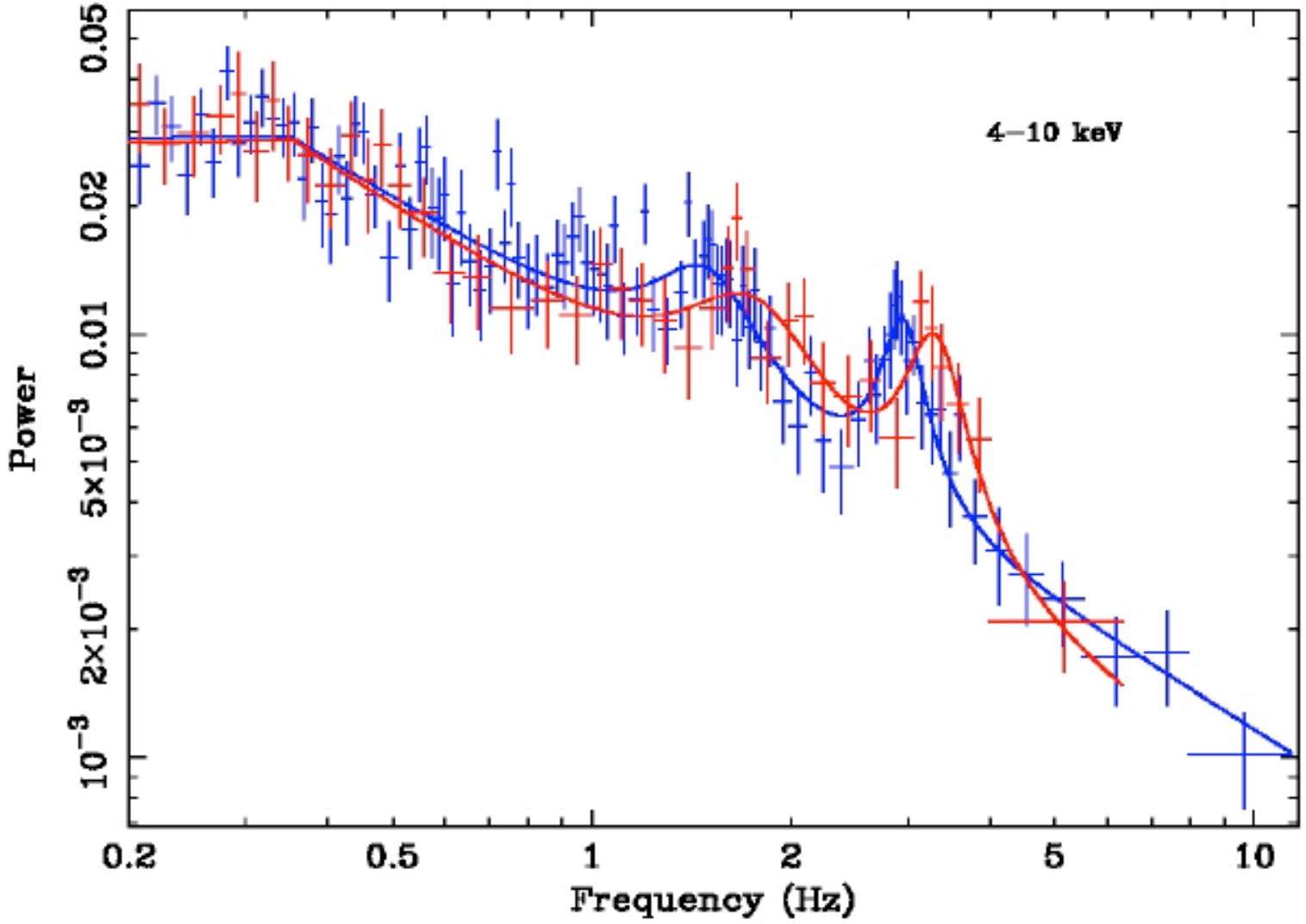

Montanari, T & Frontera 2006

BH XTE J1650-500. BeppoSAX

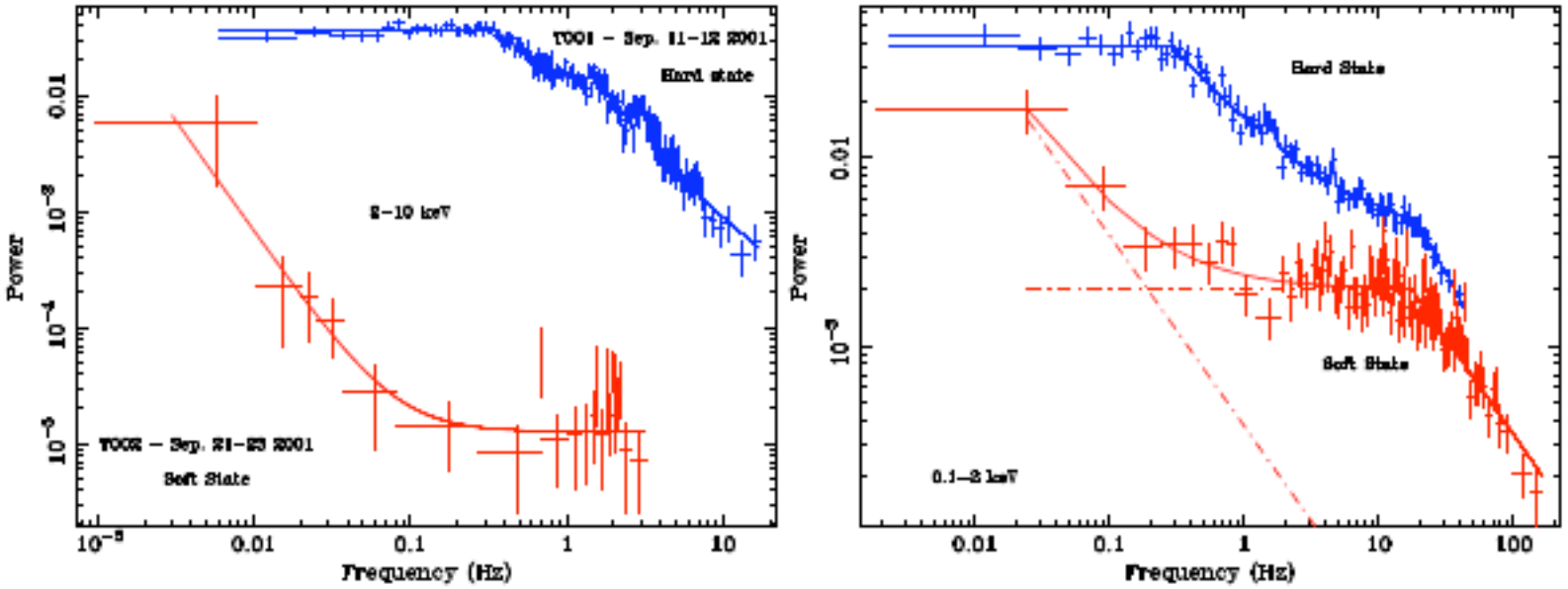

Fig. 7.— LHS PS (blue) vs that of HSS PS (red) for two different energy bands: 2-10 keV (*left panel*) and 0.12-2 keV (*right panel*). The HSS PS are fit with the sum of two broken power–laws in the case of the 0.1–2 keV energy band, while it is fit with the sum of a power-law and a constant in the 2-10 keV energy band. It is apparent that the relative power of the HSS PS (with respect to LHS PS) strongly depends on the energy band.

Montanari, T & Frontera 2008

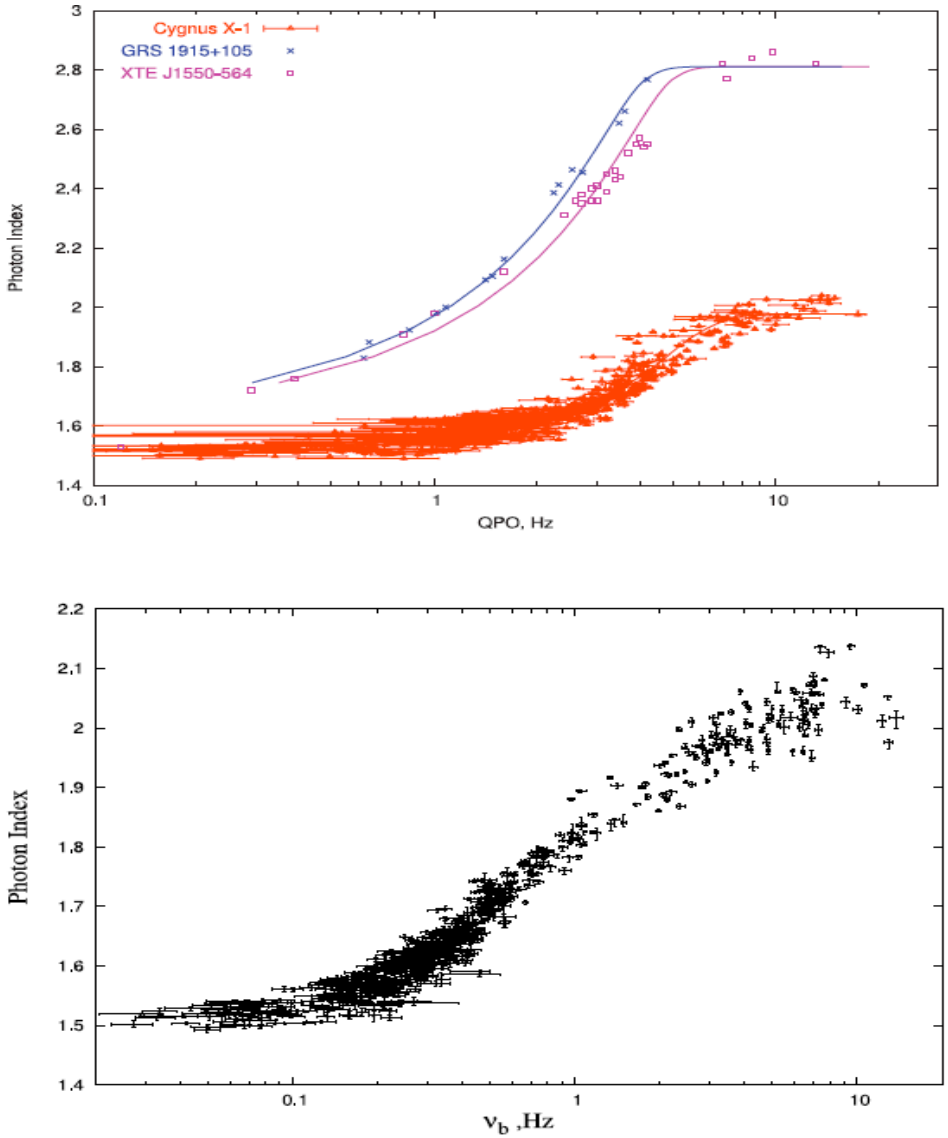

FIG. 8.—*Top*: Observed correlations between photon index Γ and low frequency ν_L (*red points*) compared with those in two other BHC sources, XTE J1550−564 and GRS 1915+105. The saturation value of the index varies from source to source, but it does not exceed the theoretically predicted value of 2.8 for the converging flow of nonrelativistic temperature (see TZ98). Presumably, the saturation value of the index depends on the plasma temperature of the converging flow (LT99). *Bottom*: Observed correlation between photon index Γ and break frequency ν_B for Cyg X-1.

Index- low QPO frequency correlation in BH candidates

Shaposhnikov & T (2006)

Ratio of sub-harmonic frequency to the low frequency

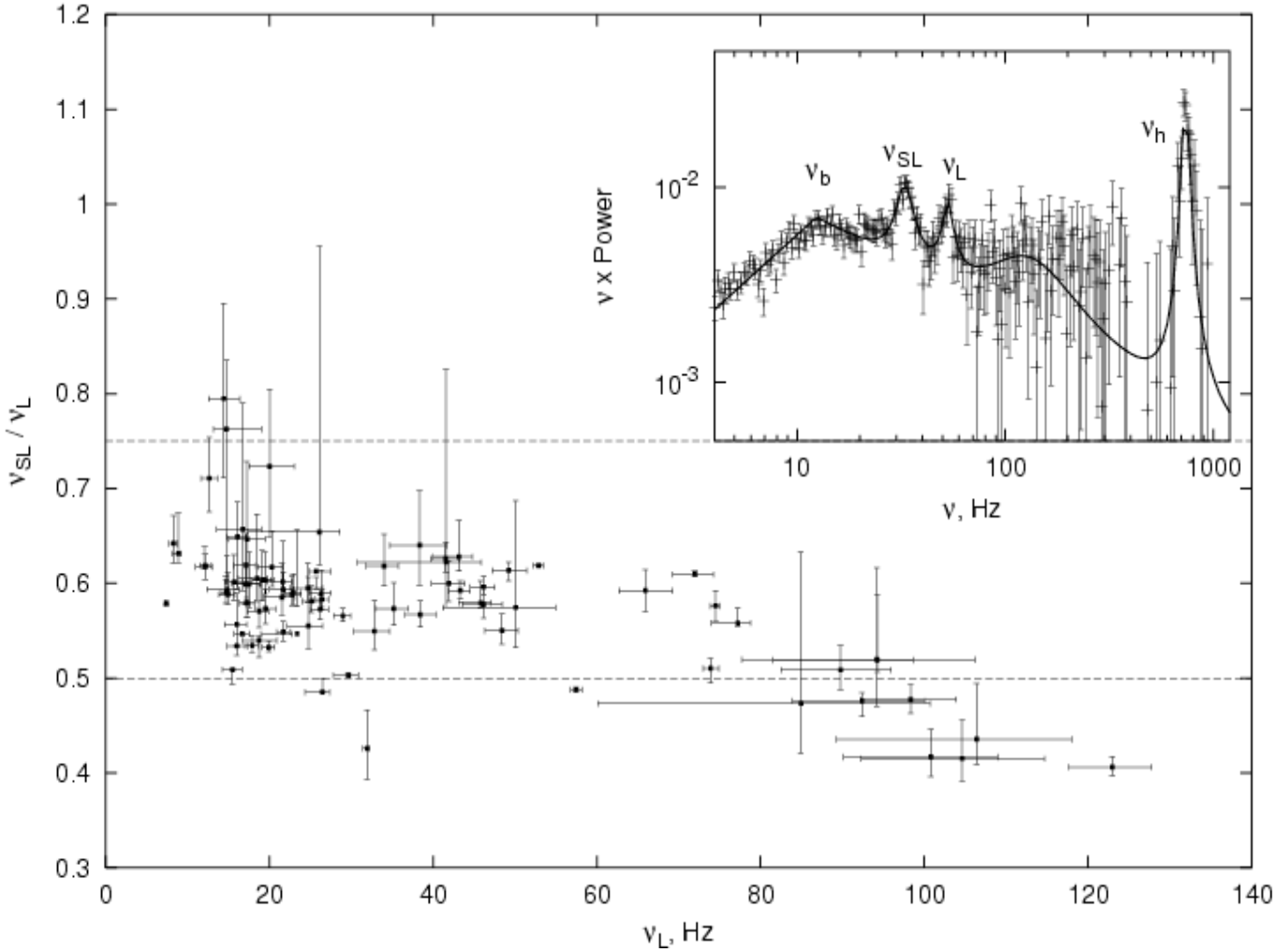

Observed ratio of sub-harmonic frequency of the low frequency ν_{SL} to low frequency ν_L as a function of ν_L . Two horizontal lines indicate the corridor where the most of ratio points are situated.

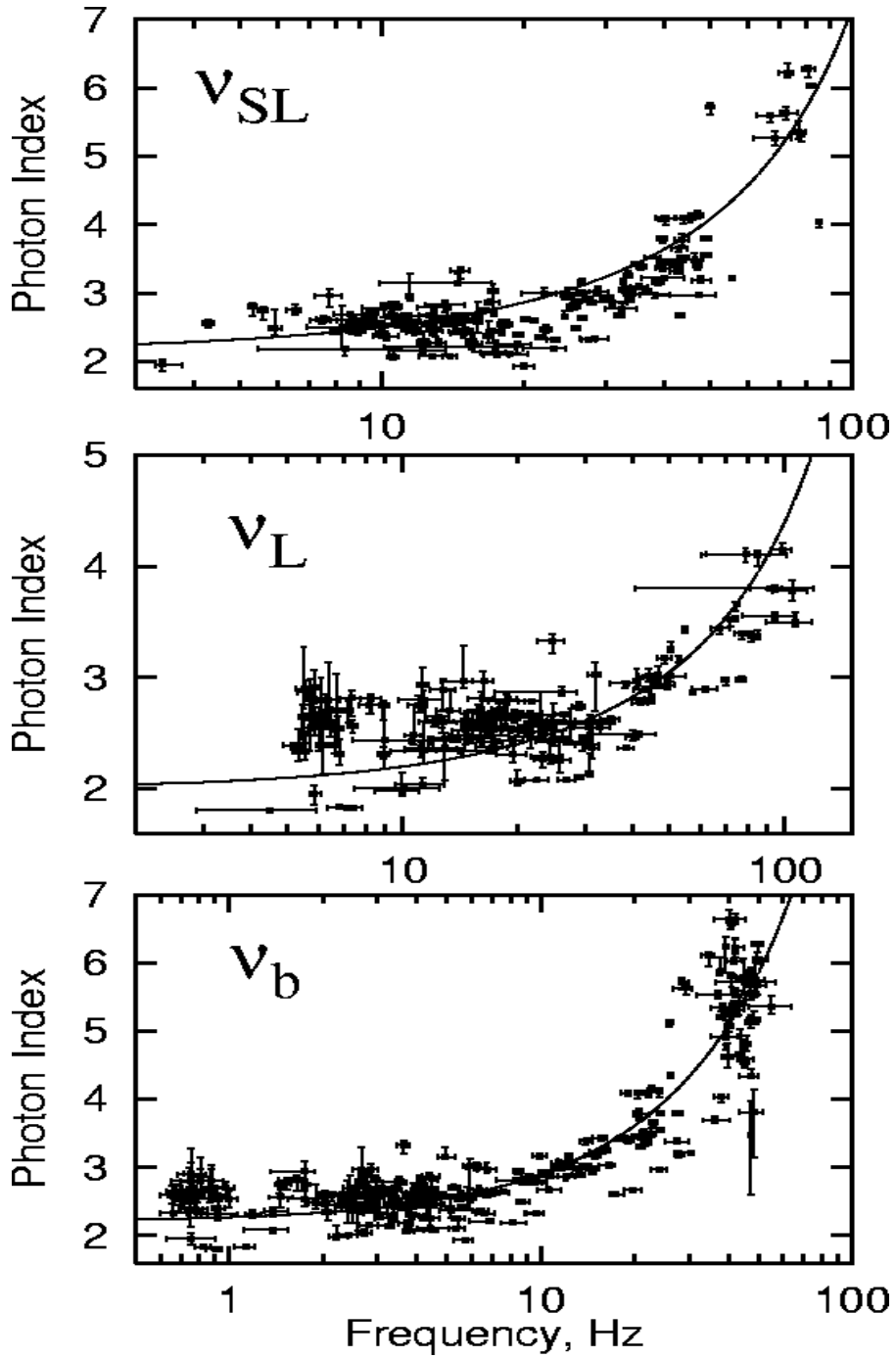

Index-QPO frequency correlation for NS source 4U 1728-34

T & Shaposhnikov (2005)

XTE-J1650 (BH)

4U 1728-34 (NS)

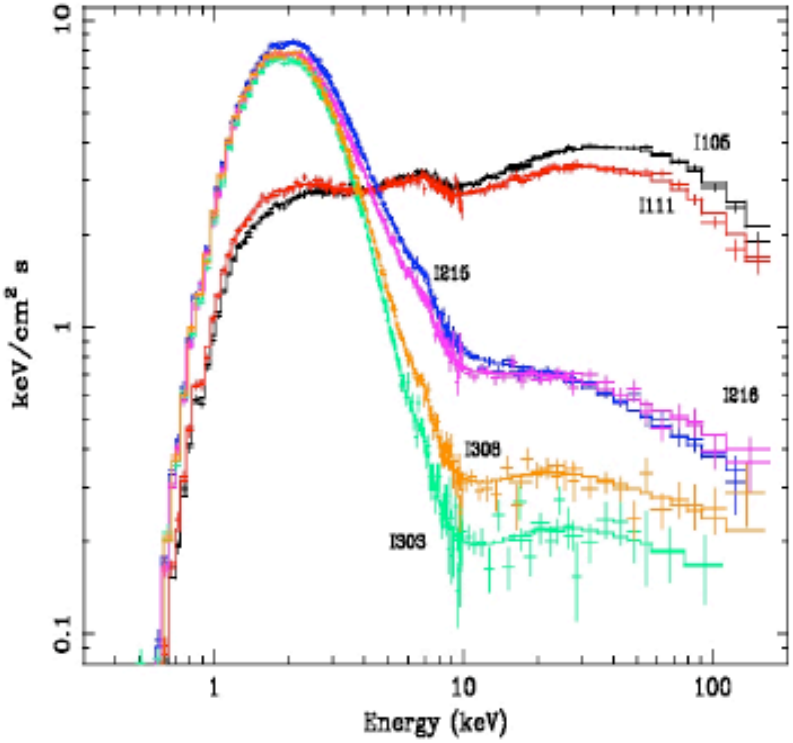

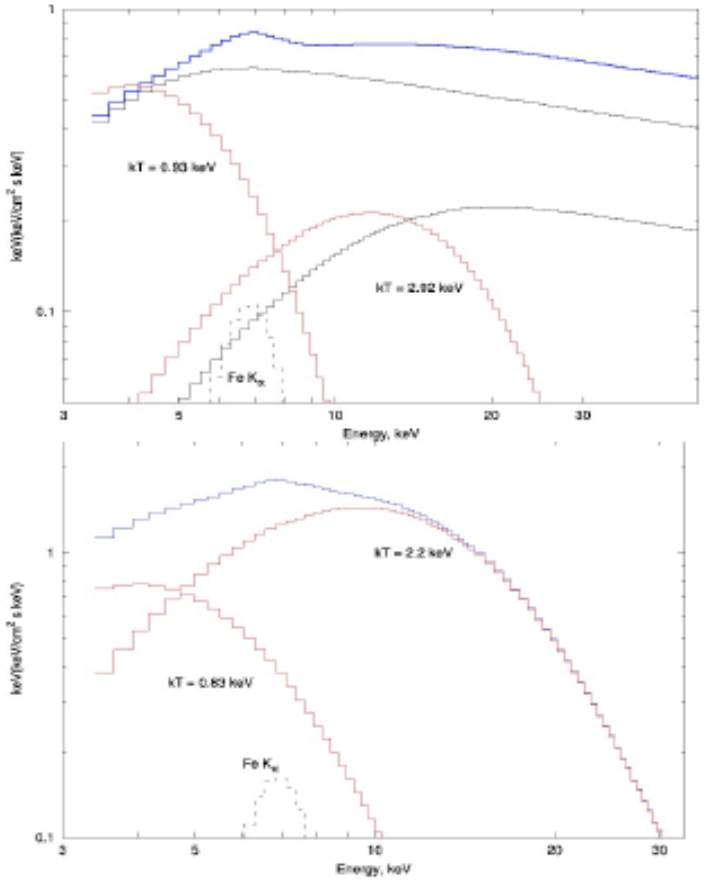

Titarchuk & Shaposhnikov (2005) ApJ 626, 298

Transition Layer. Scaling method I.

The radial motion in the disk is controlled by friction and the angular momentum exchange between adjacent layers, resulting in the loss of the initial angular momentum by accreting matter. The corresponding radial transport of the angular momentum in a disk is described by the following equation [see e.g. Shakura & Sunyaev (1973)]:

$$\dot{M}\frac{d}{dR}(\omega R^2) = 2\pi\frac{d}{dR}(W_{r\varphi}R^2), \tag{1}$$

where $\dot{M}$ is the accretion rate in the disk and $W_{r\varphi}$ is the component of a viscous stress tensor that is related to the gradient of the rotational frequency $\omega = 2\pi\nu$, namely,

$$W_{r\varphi} = -2\eta H R\frac{d\omega}{dR}, \tag{2}$$

where H is a half-thickness of a disk and η is turbulent viscosity. The nondimensional parameter that is essential for equation (1) is the Reynolds number for the accretion flow,

$$\gamma = \dot{M}/4\pi\eta H = RV_r/D, \tag{3}$$

where V_r is a characteristic velocity, and D is the diffusion coefficient. D can be defined as $D = V_t l_t/3$ using the turbulent velocity and the related turbulent scale, respectively or as $D = D_M = c^2/\sigma$ for the magnetic case where σ is the conductivity [e.g. see details of the D-definition in Lang (1998)].

Transition Layer. Scaling method II.

Equations $\omega = \omega_0$ at $R = R_{in} = bR_S$ (at the inner TL radius), $\omega = \omega_K$ at $R = R_{out}$ [the radius where the transition layer adjusts to the Keplerian motion for which $\omega_K = (GM/R^3)^{1/2}$], and $d\omega/dR = d\omega_K/dR$ at $R = R_{out}$ were assumed by TLM98 to be the boundary conditions. Note that here we set the inner boundary at $R_{in} = bR_S$ with b of 3. This value of R_{in} can valid for a BH which spin a is less than 0.8.

Thus, the profile $\omega(R)$ and the outer radius of the transition layer are uniquely determined by the boundary conditions and the angular momentum equation (1-2) for a given value of the Reynolds number γ (see Eq. 3).

The solution of angular momentum equation (1-2) satisfying the above boundary conditions is equation (10) in TLM98 and the equation (see TLM98, Eq. 11)

$$3\theta_{out}/2 = D_1\gamma r_{out}^{-\gamma} + 2(1 - D_1)r_{out}^{-2} \tag{4}$$

determines $r_{out} = R_{out}/R_{in}$ as a function of $\gamma-$parameter, where $\theta_{out} = \omega_k(r_{out})/\omega_0$ and $D_1 = (\theta_{out} - r_{out}^{-2})/(r_{out}^{-\gamma} - r_{out}^{-2})$. The adjustment of the Keplerian disk to the sub-Keplerian inner boundary creates conditions favorable for the formation of a hot plasma outflow at the outer boundary of the transition layer (TLM98), because the Keplerian motion (if it is followed by sub-Keplerian motion) must pass through a super-Keplerian centrifugal barrier region.

Transition Layer. Scaling method III.

The TLM98 numerical calculations of Eq. (4) (see Fig. 2 there) showed that the value of dimensionless outer radius r_{out} strongly depends on $\gamma-$parameter ($Re-$number) and independent of θ_{out} for $\theta_{out} >> 1$, i.e when the rotational velocity of central of object ω_0 is less of that at the TL outer boundary $\omega_{\rm K}$. In fact, one can see that the right hand side of Eq. (4) is linearly proportional to θ_{out} if $\theta_{out} \gg 1$ because $D_1 \propto \theta_{out}$ and $|D_1/r_{out}^2| \gg 1$ for $\theta_{out} \gg 1$ and $\gamma > 2$. As a result θ_{out} can be canceled from left and hand sides of Eq. (4) when $\theta_{out} \gg 1$.

It implies the CC dimensionless size $l_{cc} = (R_{out} - R_{in})/R_{in} = r_{out} - 1$ is a function $\gamma-$parameter ($Re-$number) only in the case of $\theta_{out} \gg 1$. Namely, given that $Re-$number determines the spectral state (see TLM98 and TL04) *that CC dimensionless size l_{cc} is the same for any given spectral state of BH even if BH masses differ by orders of magnitude.* Thus the CC dimensional size $L_{cc} = bR_{\rm S}l_{cc}(\gamma) \approx 9l_{cc}(\gamma)m$ km is just proportional to BH mass $m = M/M_\odot$ for a given spectral state (or γ).

It is worth noting that in the general case of non-dimensional frequency θ $(= \omega_{\rm K}/\omega_0)$ the size l_{cc} is a function of γ and ω_0 (or a BH spin a) too. The direct scaling of $L_{cc} = bR_{\rm S}l_{cc}(\gamma, a)$ with BH mass m is not possible anymore. There is a systematic shift of the values of $l_{cc}(\gamma, a)$ for a given γ because of BH spin a.

Black Hole Mass Determination.

The Main Idea

QPO frequency ν_L by definition is a ratio:

$$\nu_L \propto V/L$$

where **V** is a characteristic (acoustic) velocity in a given configuration and **L** is a size of the configuration.

But velocity **V** and dimensionless size $L_{DS} = L/R_S$ are funcition of the spectral Hardness (photon index Γ) (*T, Lapidus & Muslimov 1998)*

Thus for a given index (spectral state) and for two black hole sources of masses $M_1 = M_1/M_\odot$, $M_2 = M_2/M_\odot$

$$\text{Log } \nu_1 - \text{Log } \nu_2 = \text{LOG } (M_2/M_1)$$

Verification of the Scaling Method

GRS 1915+105 & GRO J1655-40

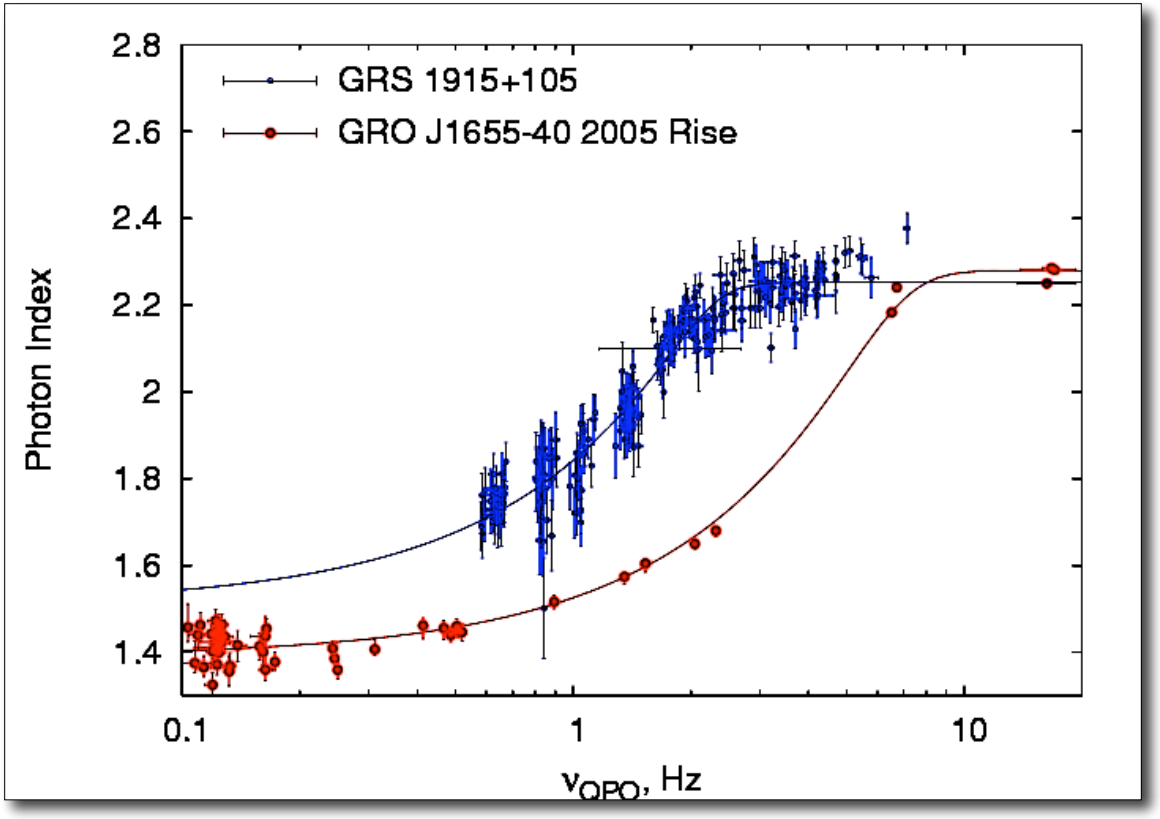

- Scaling Coefficient

$M_{1655}/M_{1915}=0.41\pm0.01$

- Given that

$M_{GRO\ J1655+40}=(6.3\pm0.5)$ solar masses

we obtain that

- $M_{GRS\ 1915+105}=$

(15.6±1.5) solar masses

Optical: 10.0-18.0 M_Sun

(Griener et al. 2001)

Shaposhnikov & T (2007)

BH Mass Determination in Cygnus X-1

Cygnus X-1 & GRO J1655-40

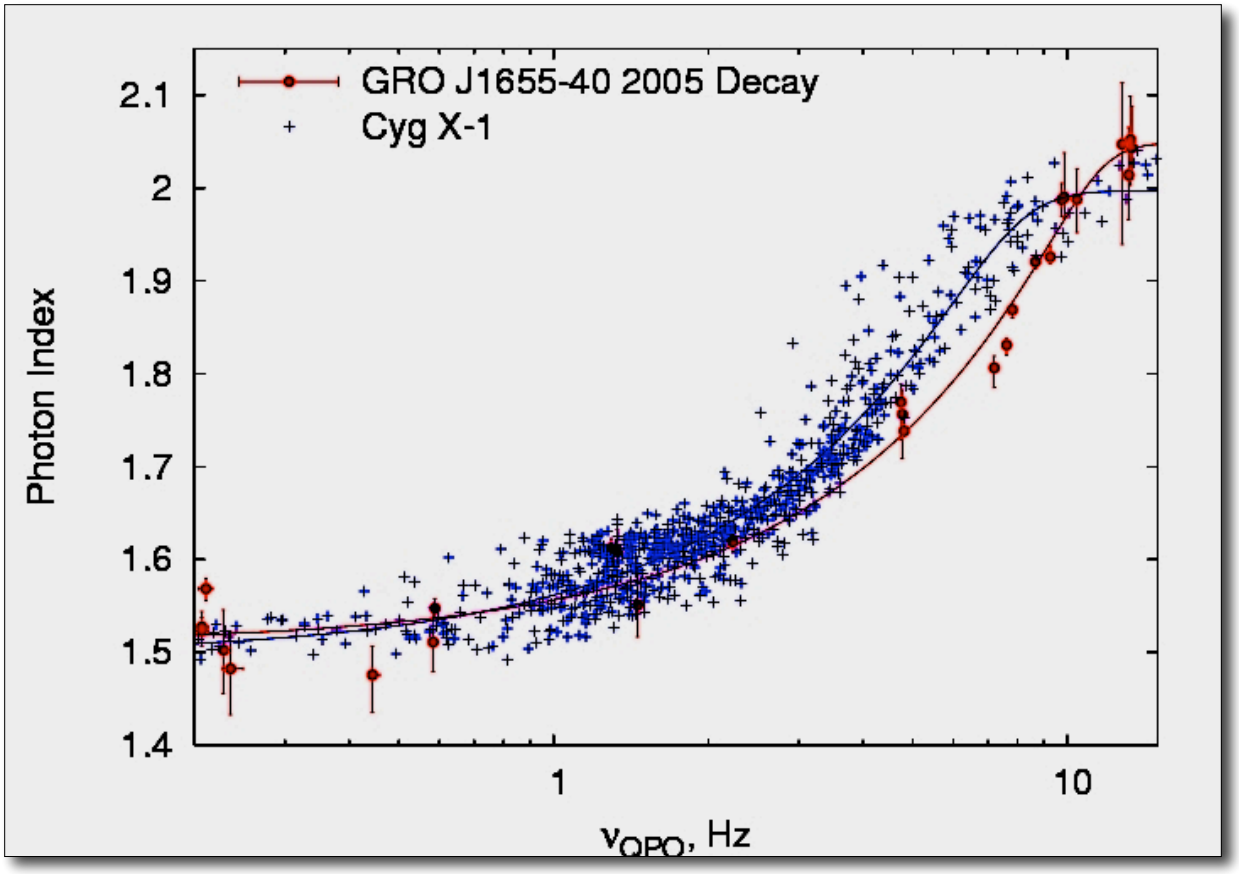

- $M_{\text{Cyg X-1}}$ =

8.7 ± 0.8 solar masses

Optical: 6.85-13.25 M_{sun}

Shaposhnikov & T (2007)

NASA PRESS RELEASE

NASA Scientists Pioneer Technique for "Weighing" Black Holes
05.09.07

Two astrophysicists at NASA's Goddard Space Flight Center in Greenbelt, Md., Nikolai Shaposhnikov and Lev T, have successfully tested a new method for determining the masses of black holes.

This elegant technique, which Lev T. first suggested in 1998, shows that the black hole in a binary system known as Cygnus X-1 contains 8.7 times the mass of our sun, with a margin of error of only 0.8 solar mass.

Working independently, Tod Strohmayer and Richard Mushotzky of Goddard and four colleagues used T's technique to estimate that an ultra-luminous X-ray source in the small, nearby galaxy NGC 5408 harbors a black hole with a mass of about 2,000 suns.

Observable Index-QPO and Index-Mdot correlations

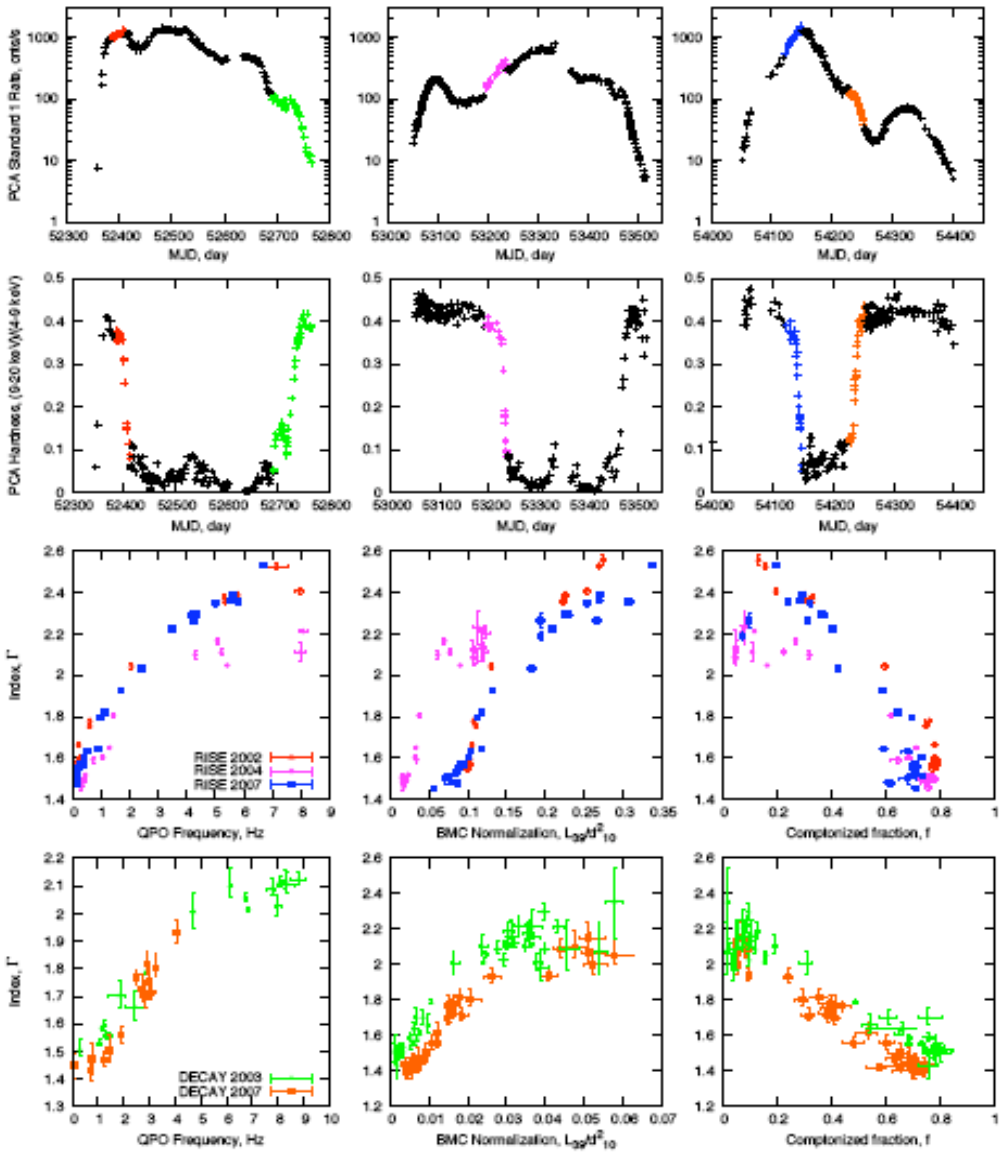

PCA Standard1 count rate (top row) and hardness (second row) for three outbursts from GX 339-4 on 2002 (left), 2004 (middle) and 2007 (right). Third and bottom rows: Index versus QPO frequency (left), and Mdot normalization (middle) and Comptonized fraction (right) for transitions in GX 339-4 (each transition is indicated by different color).

Shaposhnikov & T (2008)

Index-Mdot saturation. GRS 1915+105

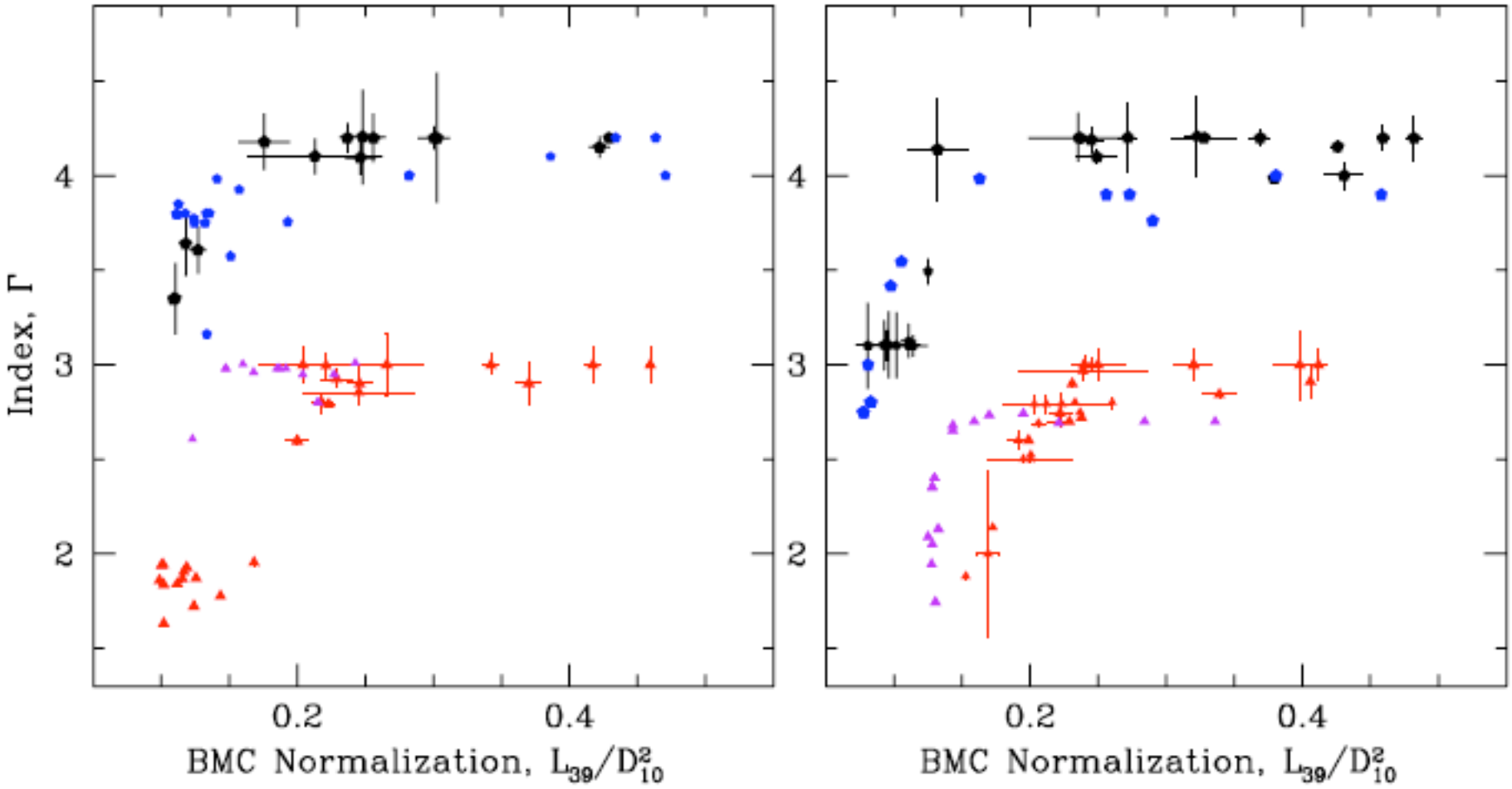

T & Seifina (2009)

The index saturation is a BH signature

Spectral index $\alpha=\Gamma$-1

$$\alpha \approx (\eta N_{sc})^{-1} = Y^{-1}.$$

Number of scatterings

$$N_{sc} \propto L/l = \tau$$

average fractional energy change per scattering

$$\eta \propto 1/\tau \text{ when } \tau \gg 1$$

spectral index saturates when CF optical depth increase!

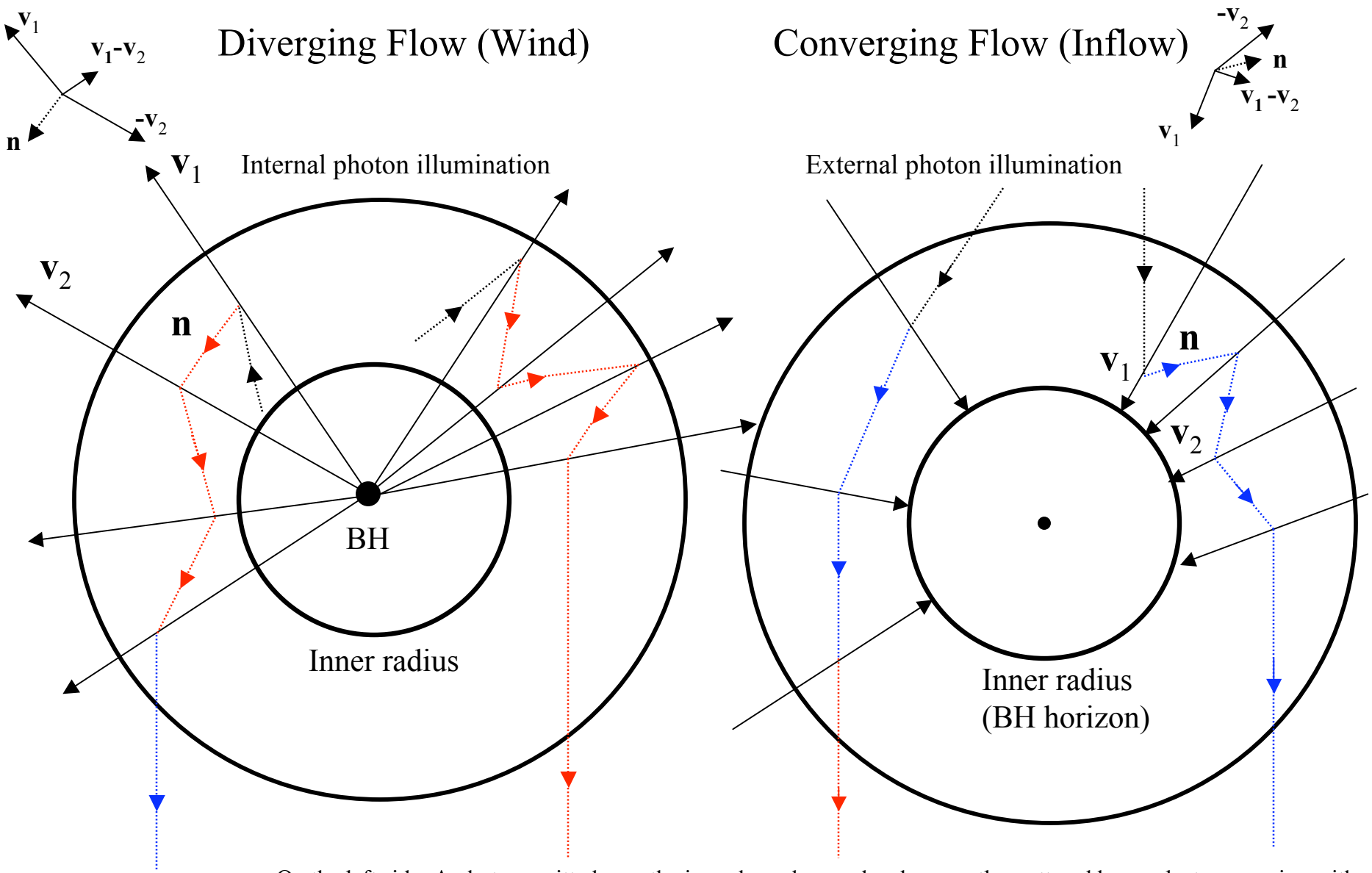

On the left side: A photon emitted near the inner boundary and subsequently scattered by an electron moving with velocity $\mathbf{v}_1$, impinges on an electron moving with velocity $\mathbf{v}_2$ as shown. The change in frequency is $\nu_2 = \nu_1 [1 + (\mathbf{v}_1 - \mathbf{v}_2\} \bullet \mathbf{n}/c]$. In a diverging flow $(\mathbf{v}_1 - \mathbf{v}_2\} \bullet \mathbf{n}/c<0$ and photons are successively redshifted, until scattered to an observer at infinity. The color of photon path indicates the frequency shift in the rest frame of the receiver (electron or the Earth observer). On the right side: In a converging flow $(\mathbf{v}_1 - \mathbf{v}_2\} \bullet \mathbf{n}/c>0$ and photons are blueshifted.

BH mass and distance determinations

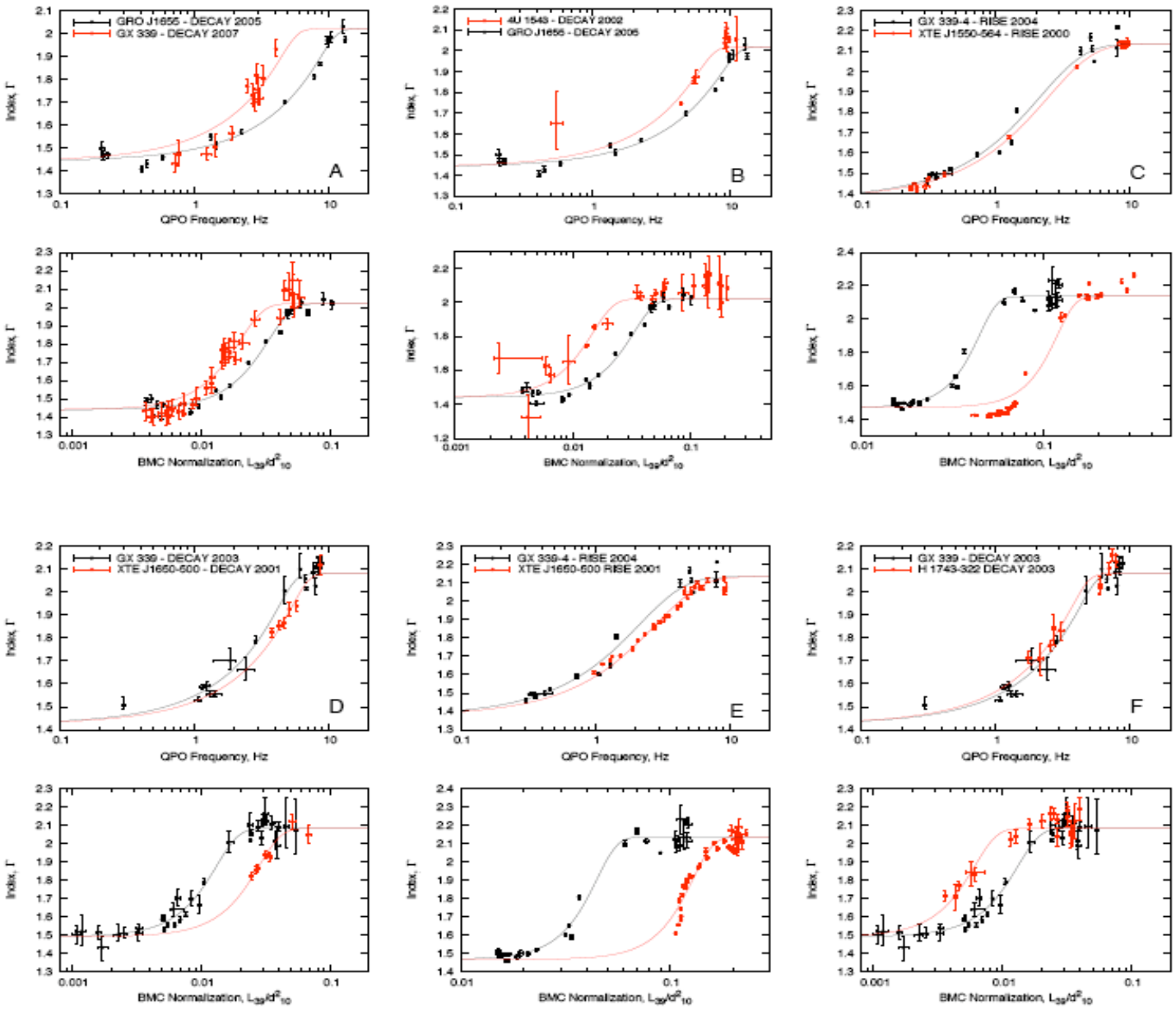

Shaposhnikov &T (2008)

The scaling method vs other methods BH masses and distances

Source	M_{dyn}[a], $M_\odot$	i,[a] deg	d,[b] kpc	M_{ST03}[c] $M_\odot$	M_{scal} $M_\odot$	d_{scal}, kpc	Refs.
GRO J1655-40[d]	6.3±0.3	70±1	3.2±0.2				1,2
GX 339-4	> 6	-	7.5±1.6	9.0±3.8(4)	12.3±1.4	5.75±0.8	5,6
4U 1543-47	9.4±1.0	20.7± 1.5	7.5±1.0	14.8±1.6 (6.4)	9.4±1.4	9.4±1.8	7,8
XTE J1550-564	9.5±1.1	72±5	∼2.5,∼6	9.4±2.1 (5)	10.7±1.5	3.3±0.5	9,10,11
XTE J1650-500	$2.7 - 7.3$	> 50	2.6±0.7	10.6±4.0 (5)	9.7±1.6	3.3±0.7	12,13
H 1743-322	∼11	~ 70	∼10	-	13.3±3.2	9.1±1.5	14
XTE J1859-226	7.6 - 12.0	-	11	12.3±1.7 (11)	7.7±1.3	4.2±0.5	15,16
Cygnus X-1	6.8 - 13.3	35± 5	2.5±0.3	-	7.9±1.0	2.2±0.3	3,4

[a]Dynamically determined BH mass and system inclination

[b]Source distances found in literature

[c]$M_i = M \cos_i$. Source distances used by ST03 are given in paranthesis.

[d]GRO J1655-40 is a primary reference source. All masses and distances given in columns 9 and 10 are determined with respect to the best measured parameters for this source.

References. — [1]Green, Bailyn & Orosz (2001),[2]Hjellming & Rupen (1995),[3]Herrero et al. (1995),[4]Ninkov et al. (1987),[5]Muñoz-Darias et al. (2008),[6]Hynes et al. (2004),[7]Orosz (2003),[8]Park et al. (2004),[9]Orosz et al. (2002),[10]Sánchez-Fernández et al. (1999),[11]Sobczak et al. (1999),[12]Orosz et al. (2004),[13]Homan et al. (2006),[14]McClintock et al. (2007),[15]Filippenko & Chornock (2001),[16]Zurita et al. (2002)

Index-Mdot saturation and BH mass determination in SS 433

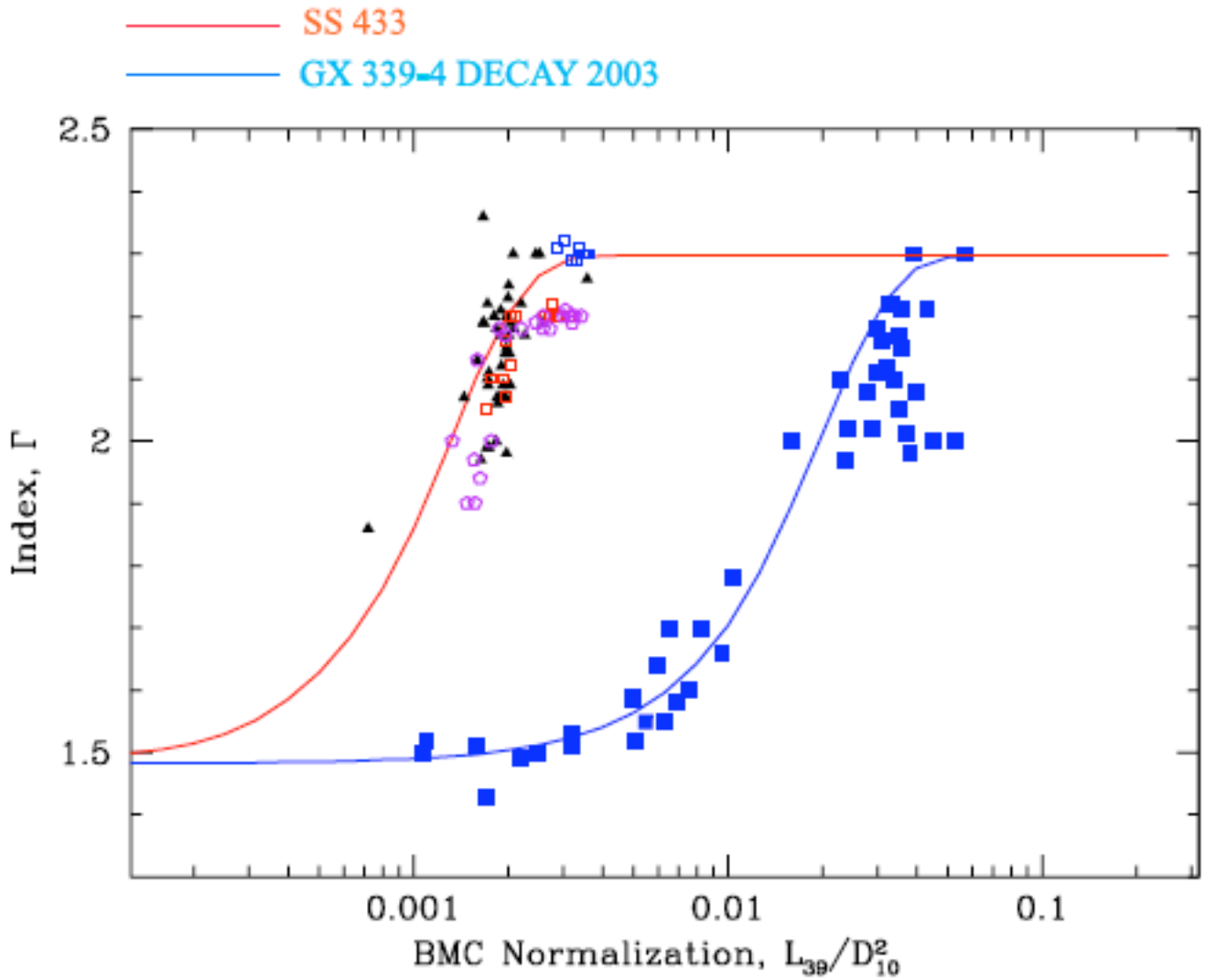

Seifina & T (2009)

Index-Mdot saturation and BH mass determination in Cyg X-3

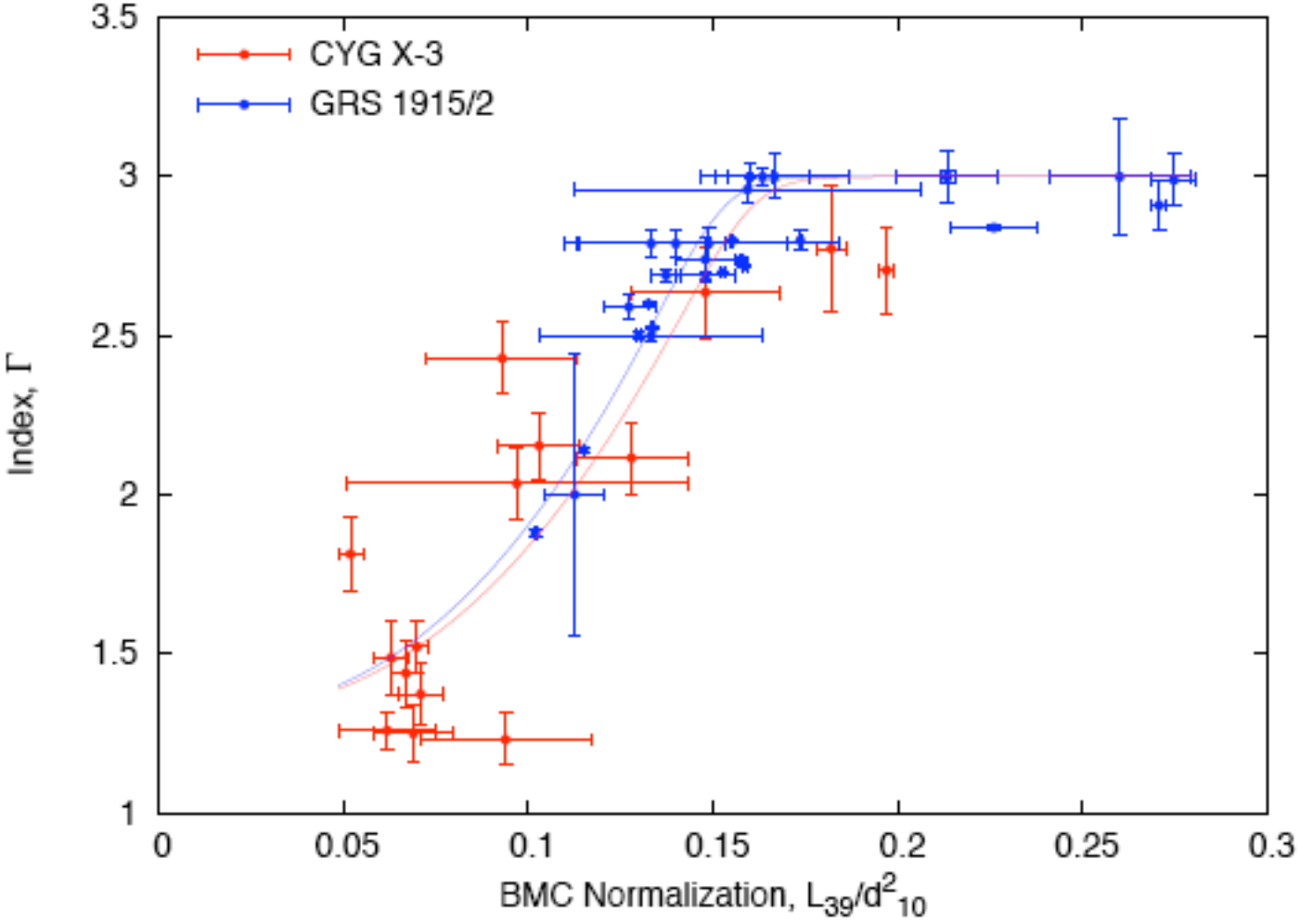

Shrader & T (2009)

Index vs High energy cutoff

XTE J1550-564

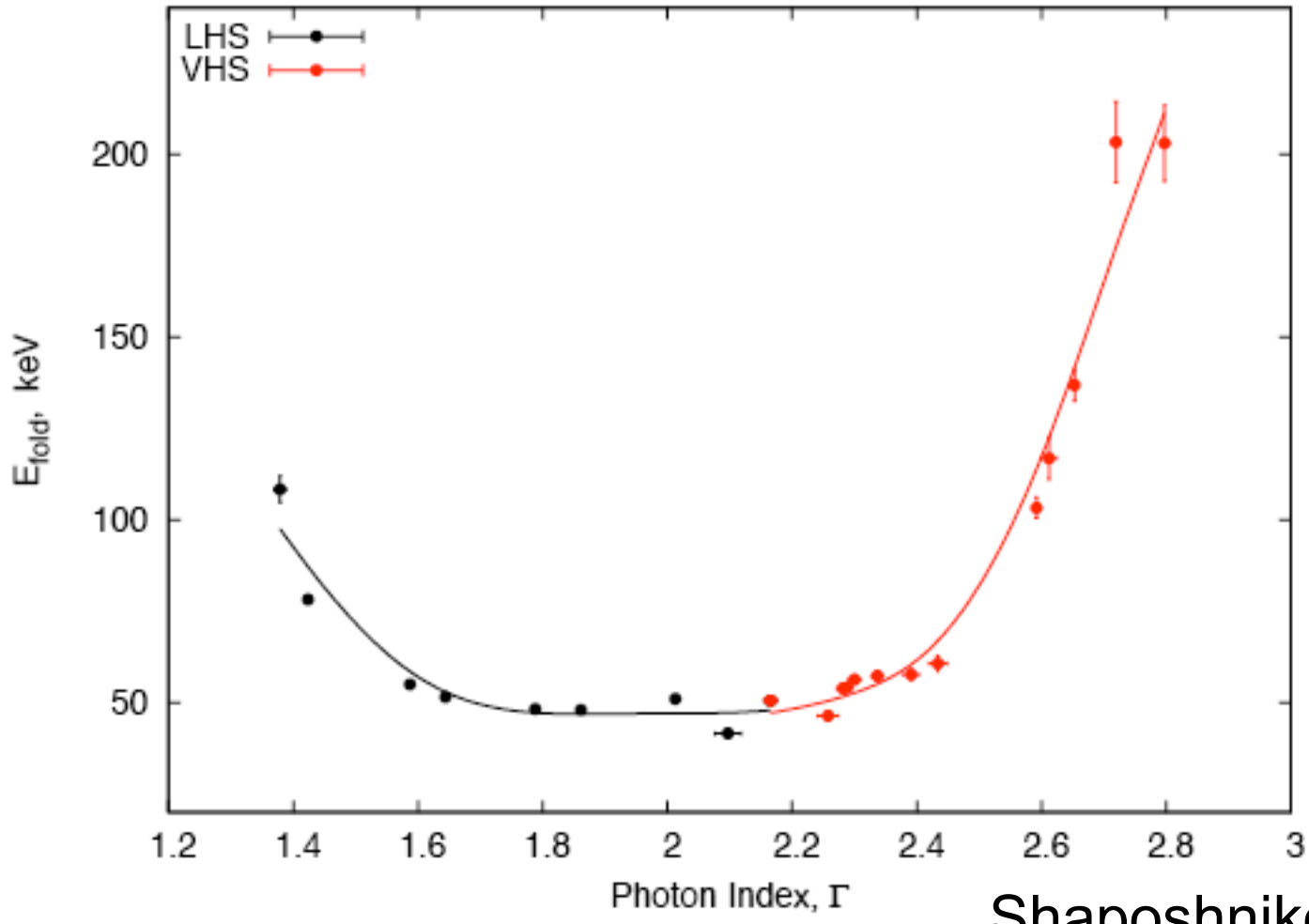

Shaposhnikov & T 2009

- What is the nature of the observed correlations?
  - Observed properites
    - QPO requency is correlated with power law index
    - Index saturates for high values of QPO frequency
    - QPO frequency is correlated with source luminosity (~dM/dt)
  - Physics: first principles
    - QPO frequency is inversely proportional to size
    - Index is inverse proportional to Comptonization efficiency (parameter)
    - Photon trapping effect in the converging flow suppresses the Comptonization efficiency for higher dM/dt
- What does it mean?
  - Correlation curves should scale as $1/M_{BH}$
  - Saturation is a BH signature

K_α line formation in the wind.

Direct component

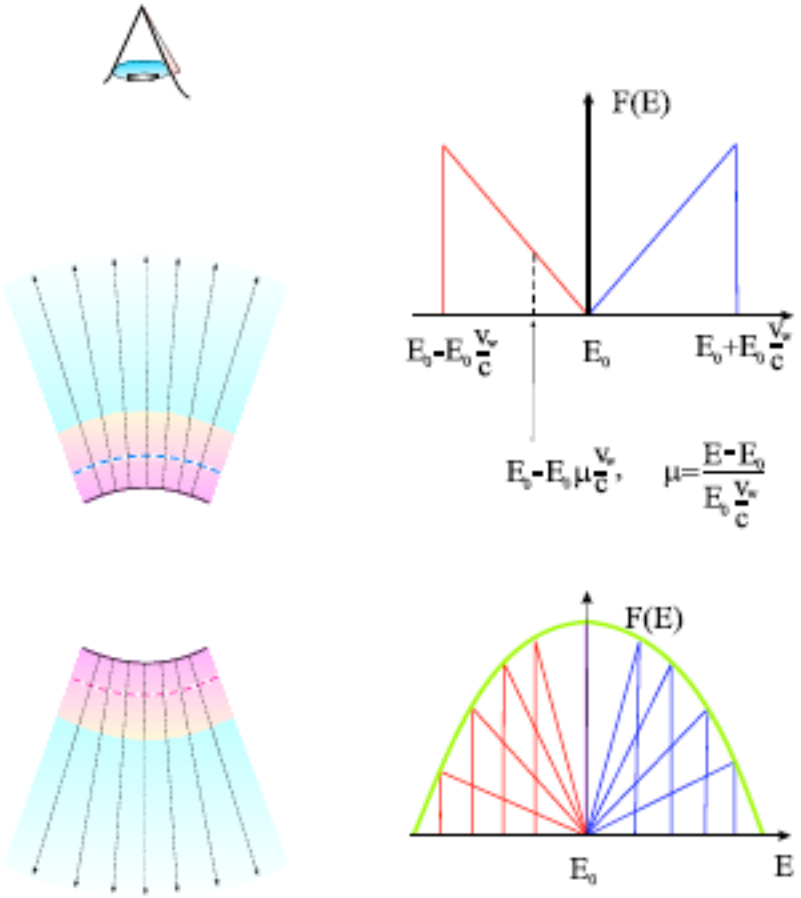

Fig. 9.— Spherical wind geometry and wind line profiles of direct component.

Observational evidence of wind.
I. Main idea of smearing out a pulsed signal

The emergent signal is a convolution

$$W(R,t) = \int_0^t \varphi(t')X(R,t-t')\,dt'$$

where $\varphi(t)$ is a pulsed signal and $X(R, t) \propto \exp(-t/t_0)$) is a scattering reprocessing function

The resulting power spectrum

$$||F_W(\omega,R)||^2 = ||F_\varphi(\omega)||^2 ||F_X(\omega,R)||^2$$

II. POWER SPECTRUM

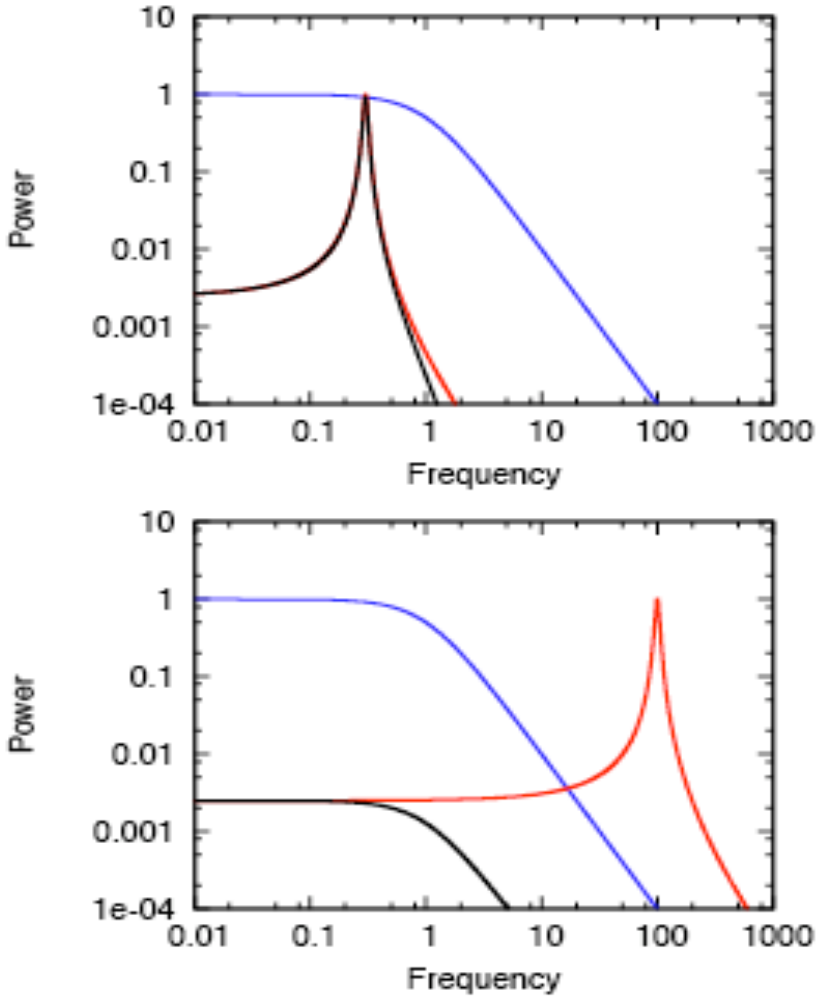

BLUE, RED AND BLACK LINES PRESENT POWER SPECTRA OF REPROCESSING FUNCTION, PULSED SIGNAL AND RESULTING PDS RESPECTIVELY

T, LAURENT & SHAPOSHNIKOV (2008)

GK Per XMM Spectrum

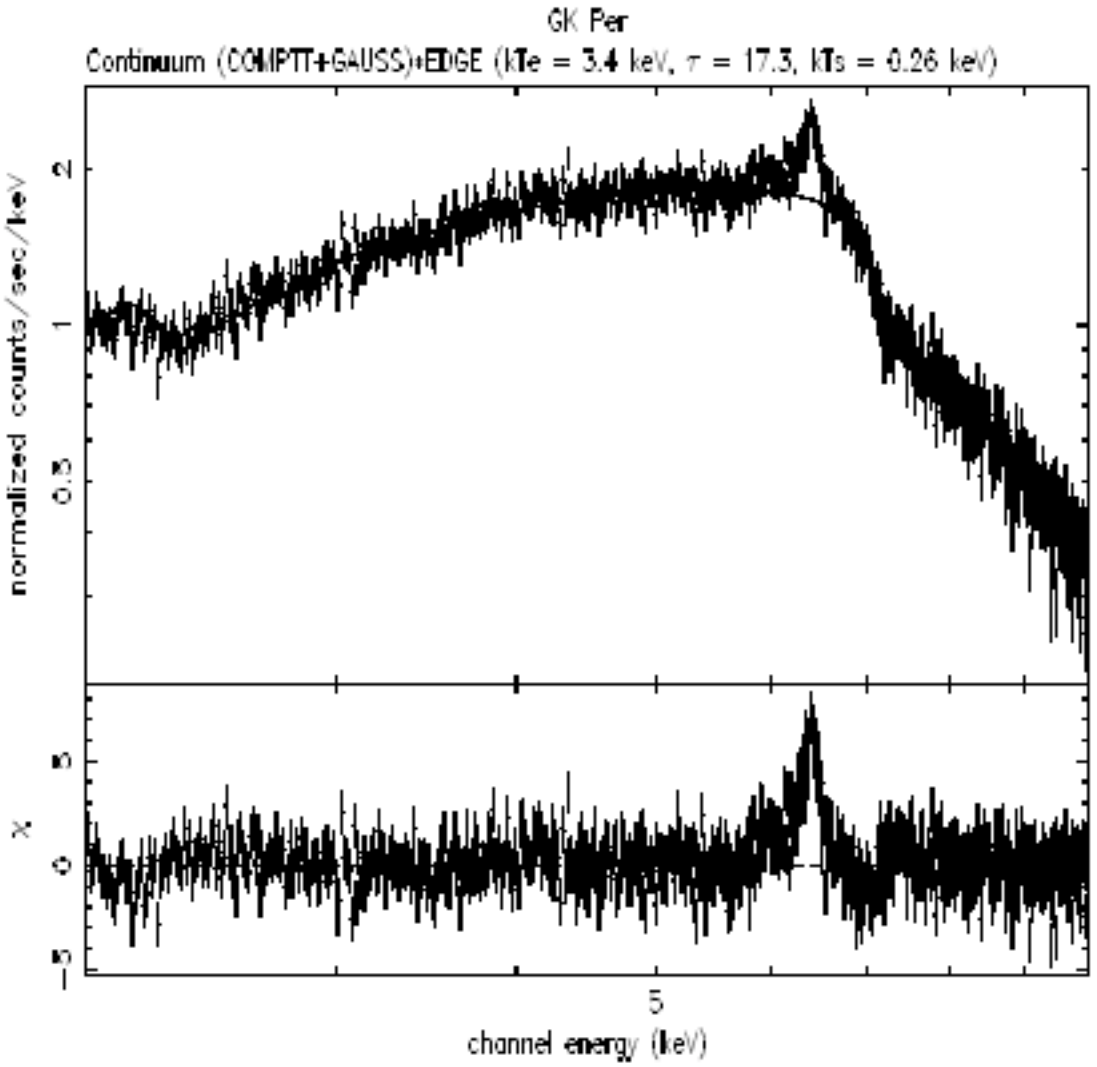

The XMM- *Newton* observation of GK Per on March 9 2002 (revolution 412)

T, Laurent & Shaposhnikov (2009)

Fit quality (GK Per). ``Relativistic model''

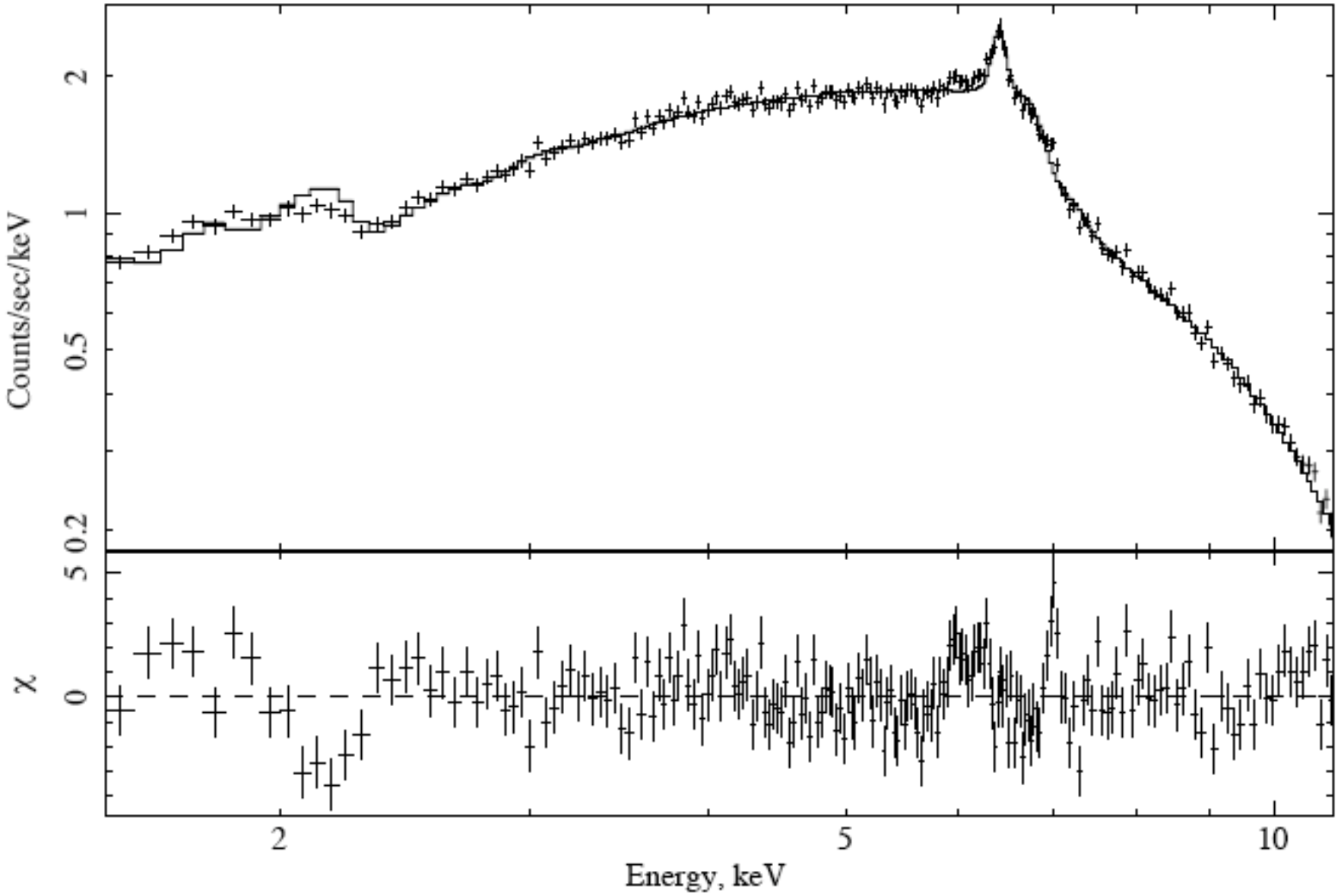

T, LAURENT & SHAPOSHNIKOV (2009)

BH GX 339-4

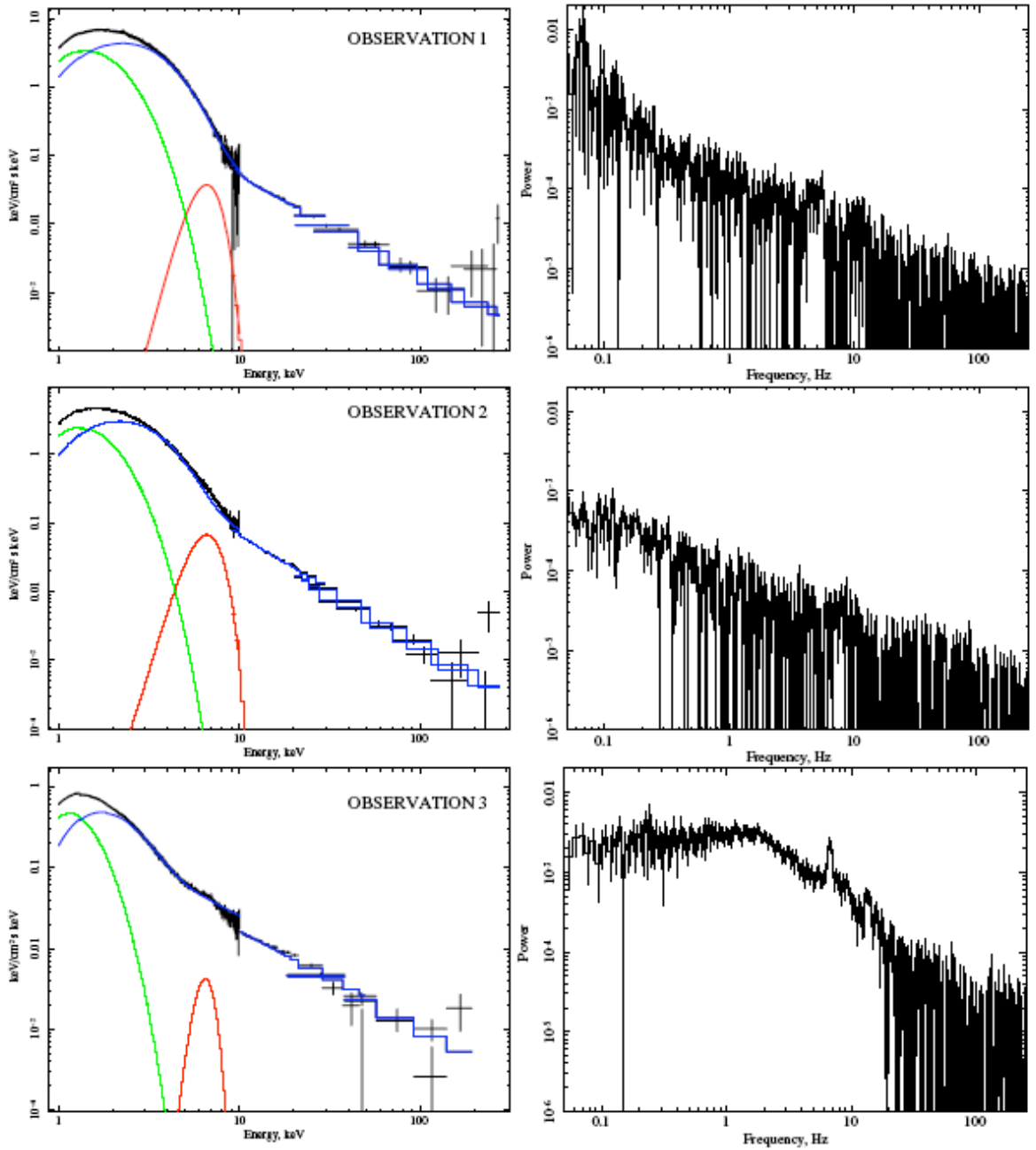

Figure 5. X-ray spectra (left panels) and PDS (right panels) for the *XMM-Newton/RXTE* observations. Note that PDSs shows the variability features (white-red noise, QPO and break frequencies) when the line is weak (see bottom panels). On the other hand PDSs are featureless when the line is strong (see top and middle panels).

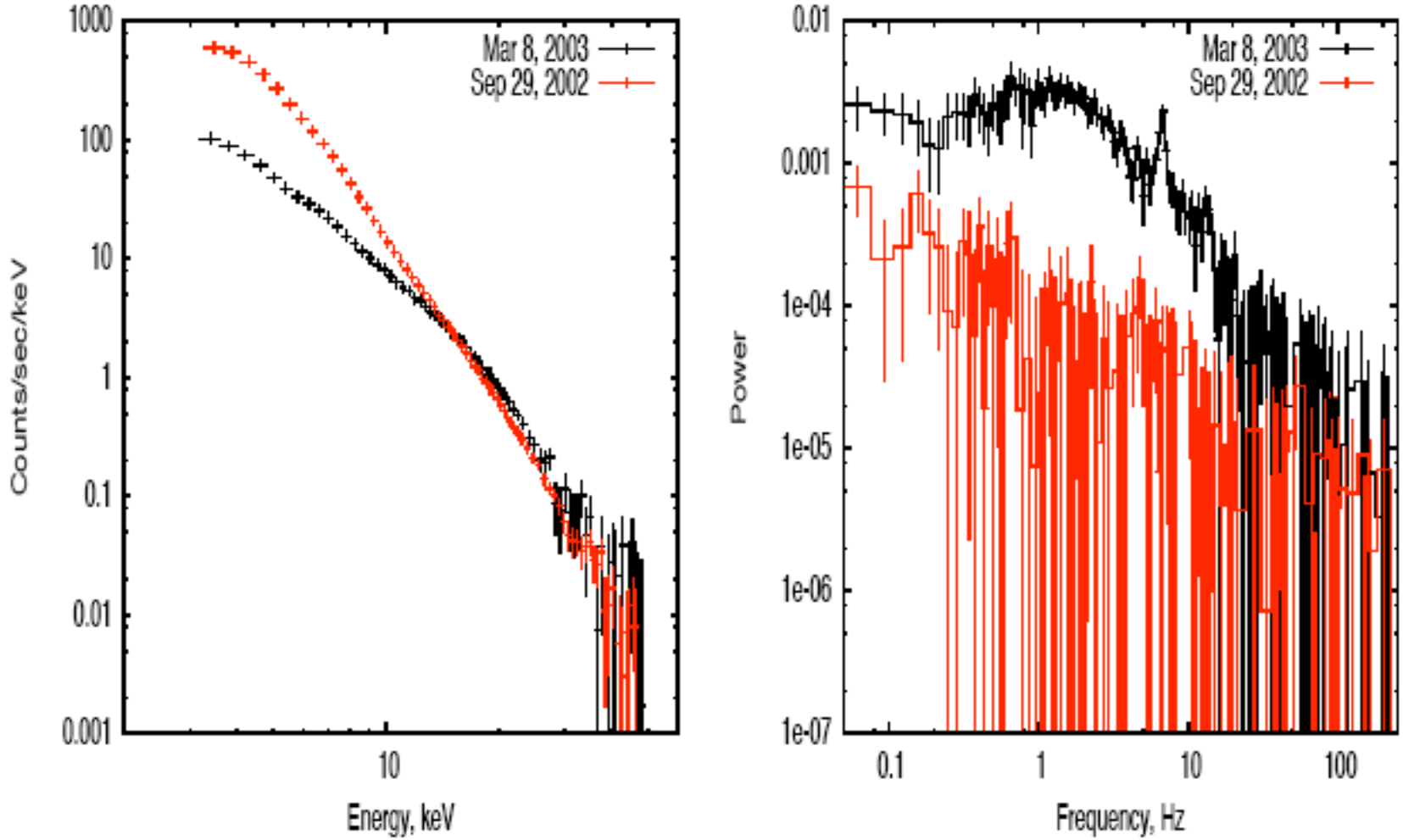

Fig. 7.— *Left:* X-ray continuum spectra of BH GX 339-4 observed with RXTE on September 29, 2002 related to XMM rev. 594 (black points) and that observed on March 8, 2003 related to XMM rev. 514 (red points). *Right:* RXTE power spectra (PDS) related to corresponding X-ray spectra. It is evident that PDS related to the strong iron line appearance (red) is featureless and noisy while in the case of the weak iron line the broken power-law continuum (white-red noise) and break frequency of 2 Hz and QPO frequency of 8 and 16 Hz are clearly seen in the PDS.

Red skewed line in GX 339-4 (rev. 514). XMM-RXTE observations

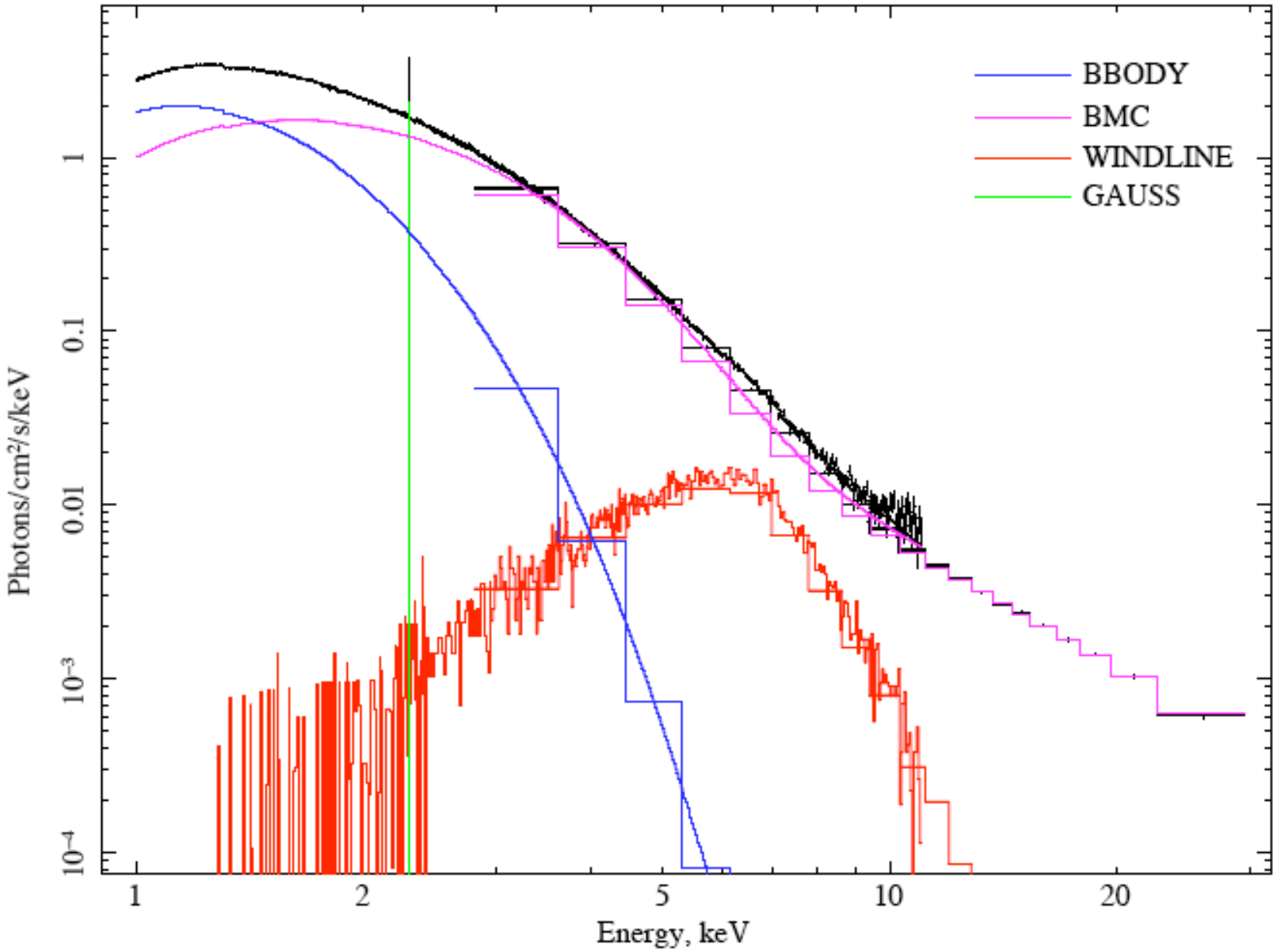

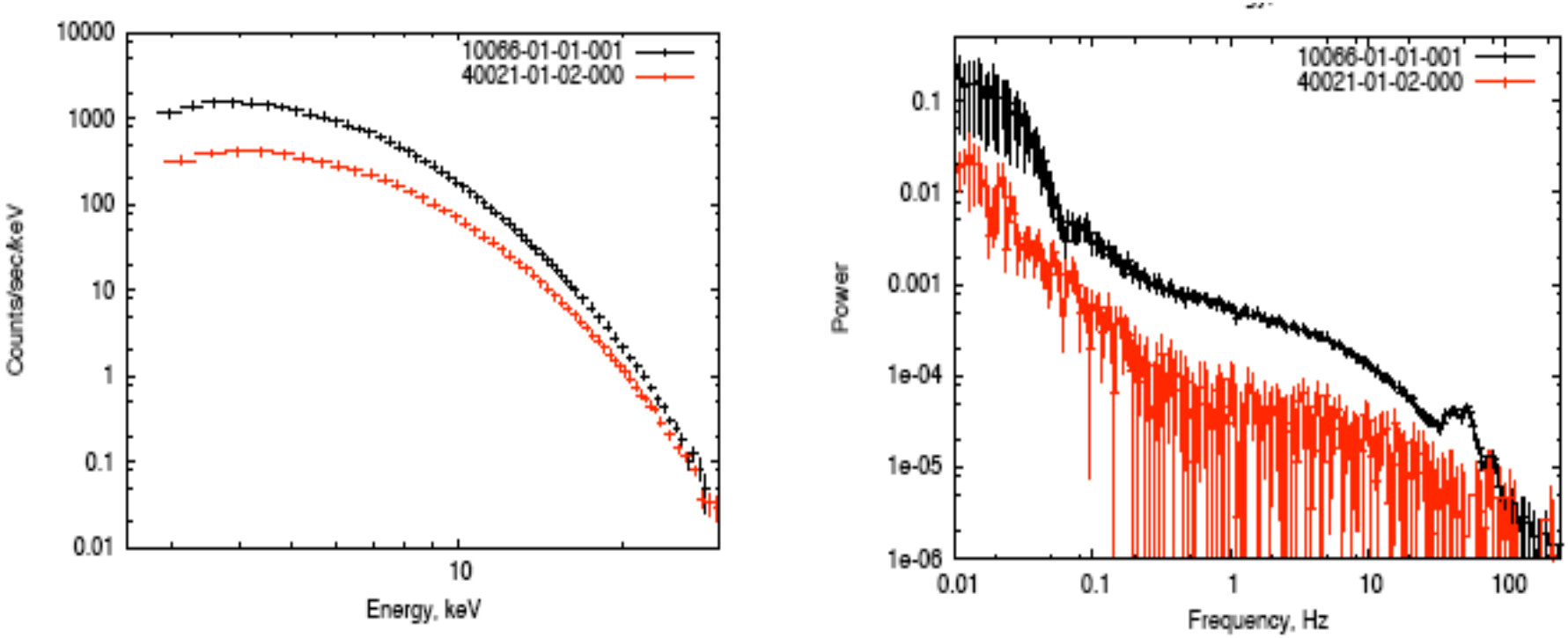

Fig. 2.— Energy and Power Density spectra as observed by *RXTE* during observation 10066-01-01-001 (black) and 40021-01-02-000 (red) . Spectral parameters during observation 40021-01-02-000 are similar to those measured during *Suzaku* observation. Timing analysis shows that high frequency variability during this particular observation is strongly suppressed.

Shaposhnikov, T & Laurent (2008)

Red skewed line in Cyg X-2. Suzaku observations

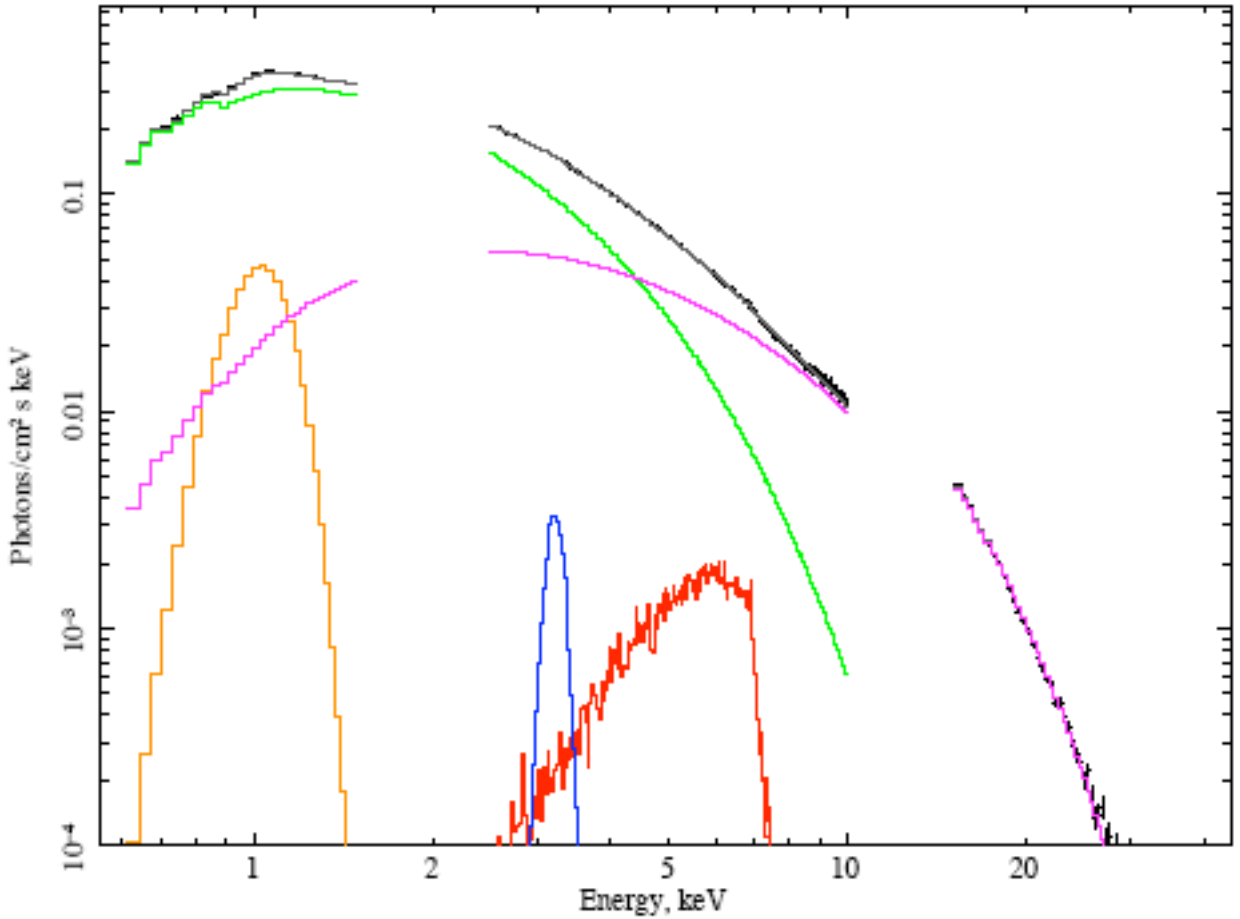

Fig. 2.— Unfolded model fit to the *Suzaku* Cyg X-2 spectrum with the Model 4. The best-fit model of the source spectrum consist of `comptt` (magenta), `diskbb` (green), `windline` (red) and two `gaussians` at 1 keV (brown) and 3.2 keV (blue).

Redskewed iron line profiles in CV (GK Per). Wind model

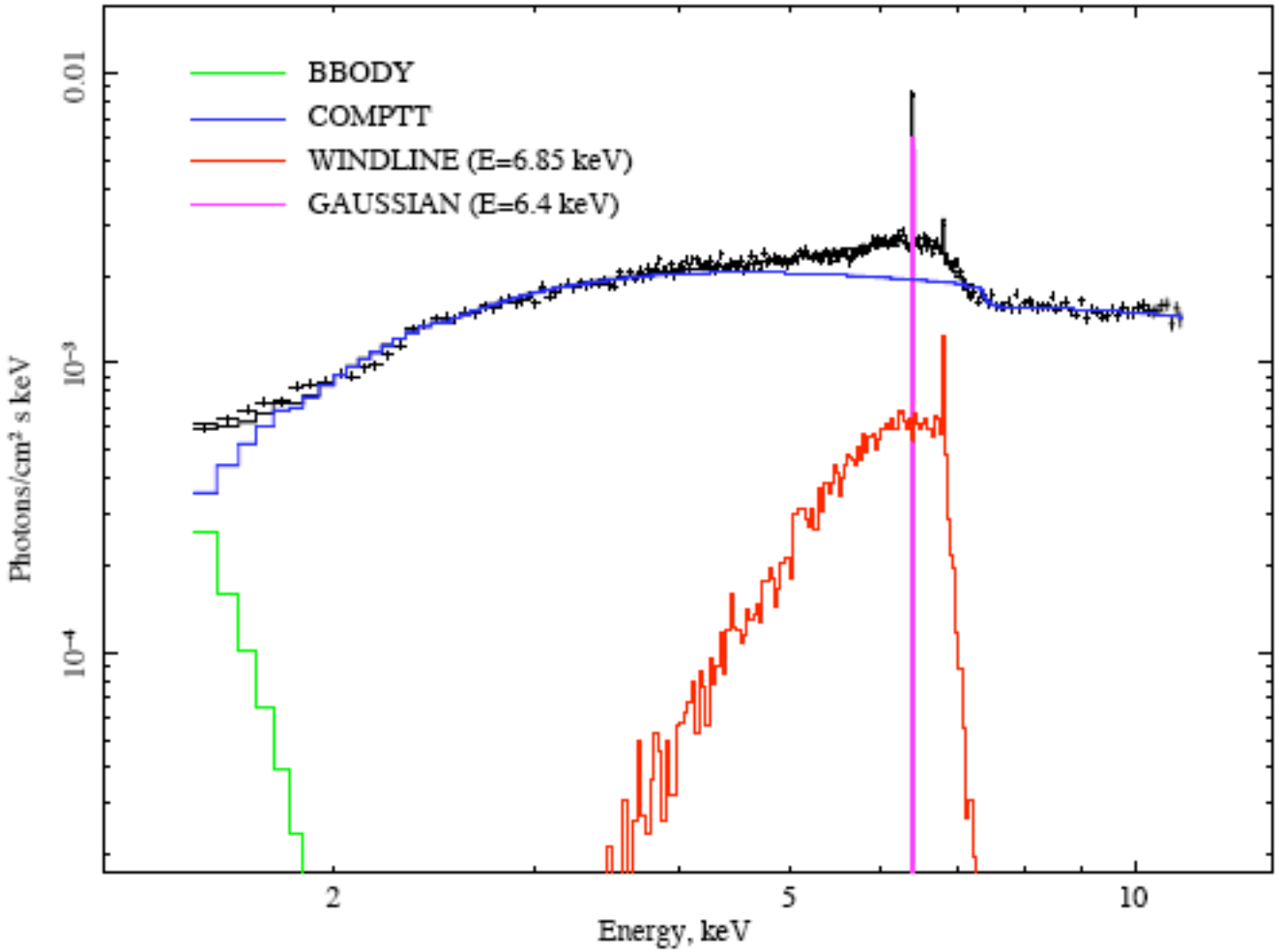

T, LAURENT & SHAPOSHNIKOV (2008)

Redskewed iron line profiles in CV (GK Per). ``Relativistic model''

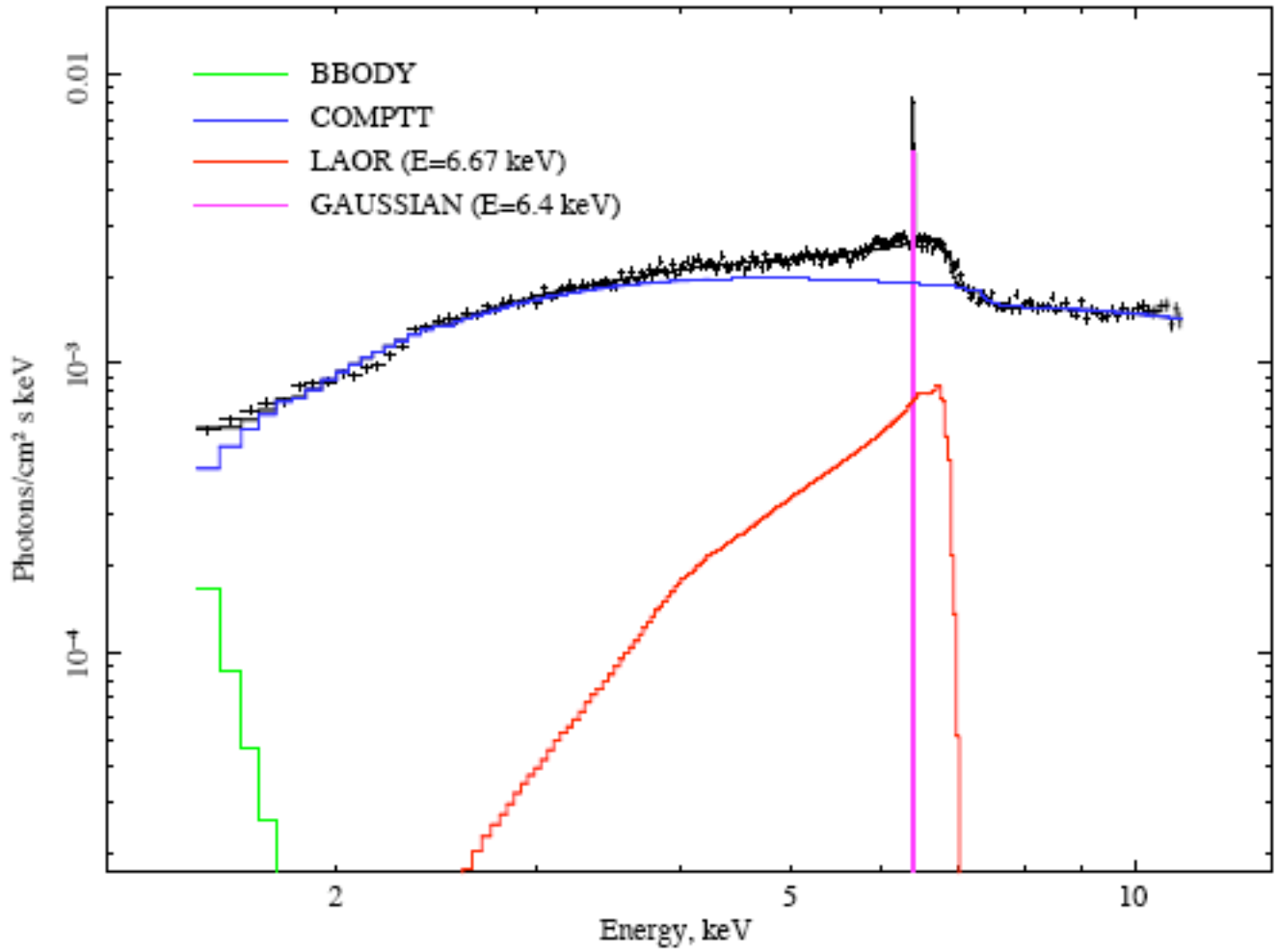

T, LAURENT & SHAPOSHNIKOV (2009)

Fit quality (GK Per). Wind model

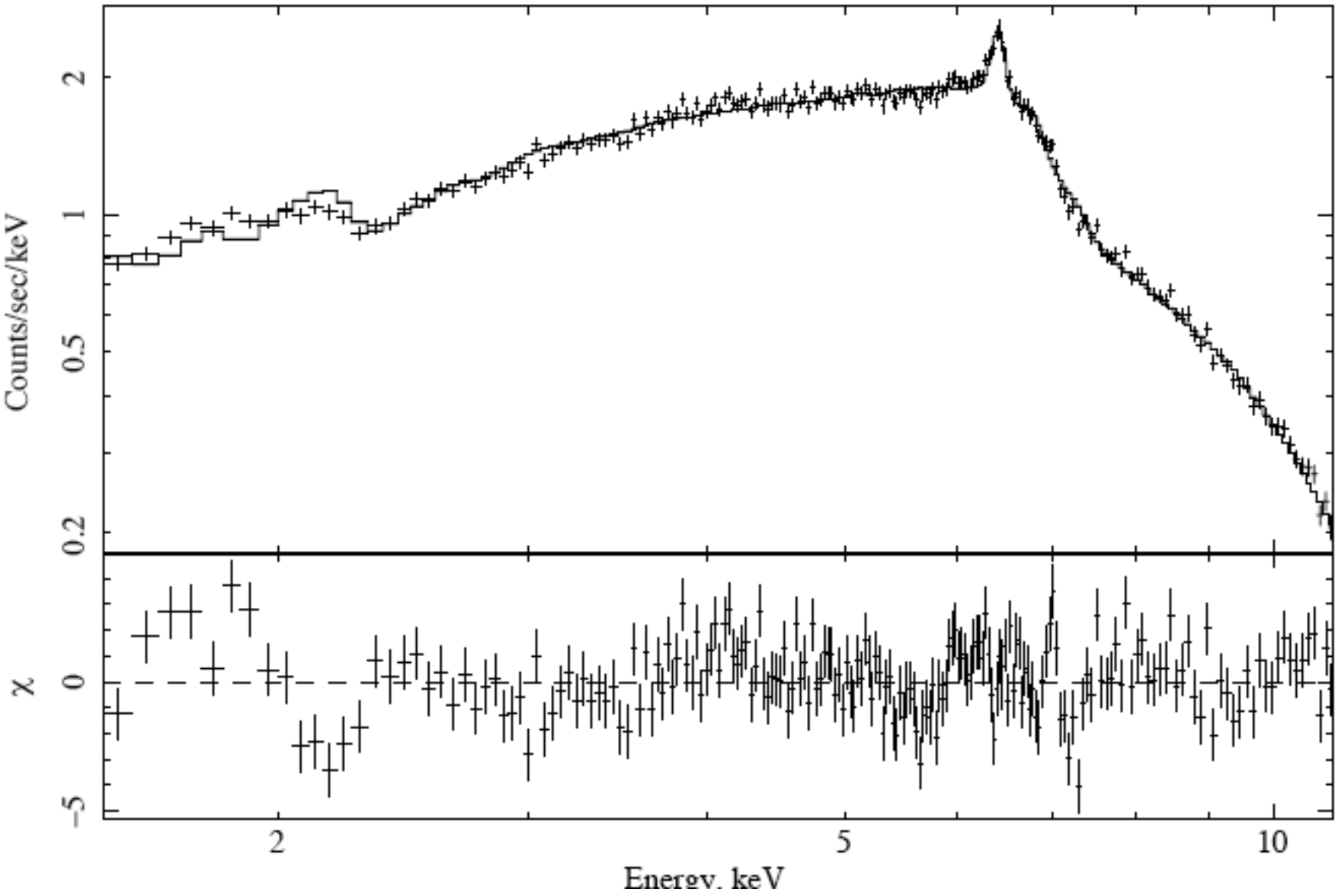

T, LAURENT & SHAPOSHNIKOV (2009)

Summary

1. A new method for evaluation of the BH mass using this observable index-frequency correlation is demonstrated.

2. In the soft state this index-QPO and Mdot correlations show the saturation to the photon index at high values of the low frequency which are identified as a black hole signature.

3. The K_α line iron emission with redskewed features in CV GK Per indicates that the red skewness of the line cannot be a BH particular signature related to the redshift effects of General Relativity (GR).

4. If the mechanism of the K_α line formation is the same in CVs, NSs and BHs then it is evident that the GR effects would be ruled out as a cause of red skewness of the iron line.

Condition for supression of pulsed signal

$$||F_W(\omega_p)||^2 / ||F_W(\omega_p)||^2_{max} = [(\omega_p t_0)^2+1]^{-1} << 1$$

which leads to inequality

NS case:

$$0.7\tau_e^2(\nu_p/400\ \text{Hz})^2\,(L/10^7\ \text{cm})^2 >> 1$$

$$\text{or } \tau_e > 1$$

BH case:

$$(\tau_e/0.02)^2(\nu_p/100\ \text{Hz})^2\,(L/10^{11}\ \text{cm})^2 >> 1$$

$$\text{or } \tau_e > 0.02.$$

The above relations are for scattered component of the resulting signal. The direct component of the pulsed radiation is attenuated as exponential $\exp(-\tau_e)$.

T, Laurent & shaposhnikov (2008)

GK Per XMM Spectrum

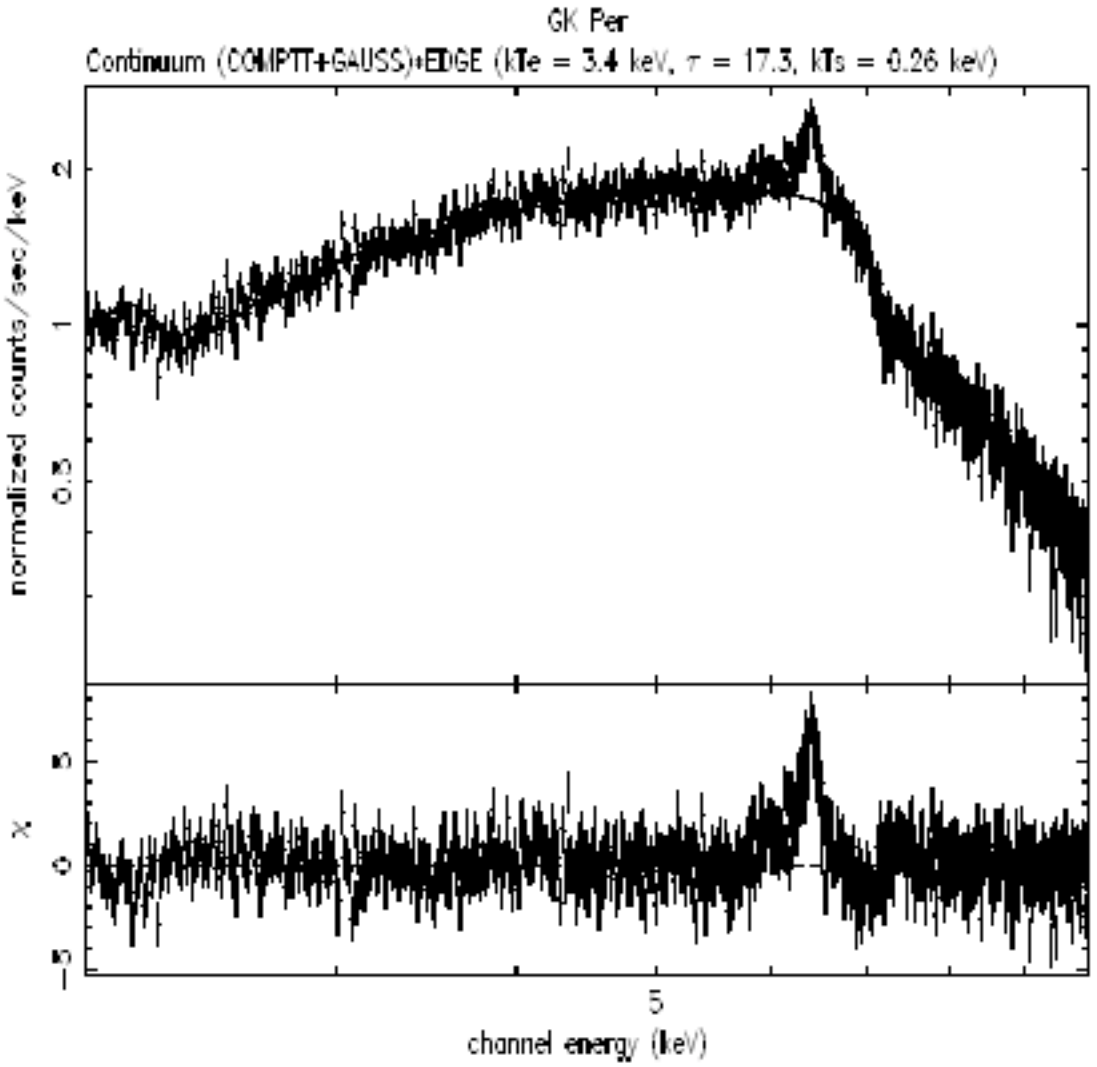

The XMM- *Newton* observation of GK Per on March 9 2002 (revolution 412)

T, Laurent & Shaposhnikov (2008)

Best-fit parameters of the XMM Iron Line Spectra for GK Per, Ser X-1 and GX 339-4

Table 2. Best-fit parameters of the XMM-*Newton* Line Spectra for GK Per, Ser X-1 and GX 339-4

Source	Best-fit parameters[a] of the Wind Line Model
GK Per	$\beta = 0.01 \pm 0.005$, $\tau_W = 0.9 \pm 0.2$, $T_W = 0.1 \pm 0.05$, $E_{KL} = 6.4$
Ser X-1	$\beta = 0.02 \pm 0.01$, $\tau_W = 0.5 \pm 0.1$, $T_W = 0.45 \pm 0.1$, $E_{KL} = 6.67$
GX 339-4 (rev. 514)	$\beta = 0.27 \pm 0.04$, $\tau_W = 0.32 \pm 0.2$, $T_W < 2$, $E_{KL} = 6.47$
GX 339-4 (rev. 594)	$\beta < 0.008$, $\tau_W < 0.2$, $T_W < 0.1$, $E_{KL} = 6.45$

[a]Energy of line and plasma wind temperatures in keV.

Summary II of first part

1. QPO-spectral index data contain information about the mass of compact object.
2. QPO-index scaling is a good alternative to dynamical mass measurement.
3. QPO-Index scaling method applied gives:

$M_{\text{GRS 1915+105}} = (15.6 \pm 1.5)\, M_{SUN}$

$M_{\text{Cygnus X-1}} = (8.7 \pm 0.8)\, M_{SUN}$,

$M_{\text{H1743-322}} = (10 \pm 1) M_{SUN}$ BHC -> BH

$M_{GX\ 339\text{-}4} \approx M_{XTE\ J1859+226} \sim (9.7 \pm 0.8)\, M_{SUN}$ BHC -> BH

4. Simultaneous timing and spectral analysis is essential for diagnostics of astrophysical compact objects. Missions like RXTE and BeppoSAX are crucial.

Diffusive propagation of the perturbation in the disk

Formulation of the problem

The diffusion equation for the time variable quantity $W(R,t)$, related to the surface density perturbations $\Delta\Sigma(R,t)$, $W(R,t) = \Delta\Sigma(R,t)$, can be written in an operator form

$$\frac{\partial W}{\partial t} = \mathbf{\Lambda_R} W + \varphi(t) f(R) \tag{2}$$

where R is a radial coordinate in the disk and $\mathbf{\Lambda_R}$ is the space diffusion operator. Equation (2) should be combined with the appropriate boundary conditions at $R = 0$, $R = R_0$ and initial conditions at $t = 0$. For homogeneous initial conditions, namely for $W(R,0) = 0$ the solution at any R and t can be presented as a convolution

$$W(R,t) = \int_0^t \varphi(t') X(R, t-t') dt'. \tag{3}$$

The kernel of convolution (3), $X(R, t-t')$ is a solution of the initial value problem for the homogeneous equation

$$\frac{\partial X}{\partial t} = \mathbf{\Lambda_R} X \tag{4}$$

with the following initial conditions

$$X(R, t-t')_{t=t'} = X(R,0) = f(R) \tag{5}$$

The power spectrum $||F_W(\omega)||^2$ of $W(R,t)$ can be presented as a product of the power spectra $||F_\varphi(\omega)||^2$ and $||F_X(\omega)||^2$ of $\varphi(t)$ and $X(R,t)$ respectively:

$$||F_W(\omega,R)||^2 = ||F_\varphi(\omega)||^2||F_X(\omega,R)||^2, \tag{6}$$

The X-ray resulting variable signal is determined by the fluctuations of the luminosity $\Delta L_x(t)$. We assume that the mass accretion rate variations $\Delta\dot{M}(0,t)$ is converted with efficiency ε_{eff} into the variations of the X-ray luminosity, i.e. $\Delta L_x(t) = \varepsilon_{eff}\Delta\dot{M}(0,t)$.

W01 show that for the function $\mathcal{W}(x,t) = x\hat{\nu}W(x^2,t)$ using a new variable $x = R^{1/2}$ the diffusion equation (2) can be presented in the form

$$\frac{\partial\mathcal{W}}{\partial t} = \frac{3\hat{\nu}(x)}{4x^2}\frac{\partial^2\mathcal{W}}{\partial x^2} + \varphi(t)\mathcal{F}(x)$$

where $\hat{\nu}(x)$ is viscosity in the disk, $\mathcal{F}(x) = x\hat{\nu}(x)f(x^2)$. The convolution, similar to Eq. (3), presents the solution $\mathcal{W}(x,t)$

$$\mathcal{W}(x,t) = \int_0^t \varphi(t')\mathcal{X}(x,t-t')dt'$$

where $\mathcal{X}(x,t)$ is a solution of the initial value problem (compare with Eqs. 4, 5)

$$\frac{\partial\mathcal{X}}{\partial t} = \frac{3\hat{\nu}(x)}{4x^2}\frac{\partial^2\mathcal{X}}{\partial x^2}$$

with the following initial conditions

$$\mathcal{X}(x,0) = \mathcal{F}(x).$$

The boundary condition at the outer boundary $\dfrac{\partial \mathcal{X}}{\partial x} = 0 \quad \text{at} \quad x = x_0$

Assumed that at the inner boundary $x_{\rm in} \ll x_0,\ W = \Delta\Sigma = 0,$ *which is equivalent to*

$$\mathcal{X} = 0 \quad \text{at} \quad x = x_{\rm in}.$$

We assume that perturbations of the mass accretion rate at the inner disk edge is converted with efficiency $\varepsilon_{\rm eff}$ *into perturbations of the X-ray luminosity, i.e.*

$$\Delta L(t) = \varepsilon_{\rm eff} \Delta \dot{M}(t, R_{in})$$

Because $\Delta \dot{M} = 3\pi \dfrac{\partial \mathcal{X}}{\partial x}$ *then* $Y(t) \propto \Delta L_x(t) \propto \dfrac{\partial \mathcal{X}}{\partial x}(t, 0).$

Now we consider a general case of problems where $\hat{\nu}(x) = (\hat{\nu}_0 / x_0^{\psi}) x^{\psi}.$

a. Viscosity linearly distributed over radius: $\psi = 2$

$$Y(t) \propto \sum_{k=1}^{\infty} \exp[-\pi^2 (2k-1)^2 t / 4t_0].$$

where the viscous time scale $t_0 = 4x_0^4 / 3\hat{\nu}_0 = 4R_0^2 / 3\hat{\nu}(R_0).$

Then the power spectrum of Y(t) *is:* $||F_Y(\nu)||_\nu^2 \propto \sum_{k=0}^{\infty} \dfrac{1}{(8t_0\nu/\pi)^2 + (2k+1)^4}.$

The series in the right hand side of this equation can be calculated exactly

$$||F_Y(\nu)||^2_\nu \propto \frac{\pi}{2^{3/2}a^{3/2}} \frac{\sinh 2^{1/2}\pi a^{1/2} + \sin 2^{1/2}\pi a^{1/2}}{\cosh 2^{1/2}\pi a^{1/2} - \cos 2^{1/2}\pi a^{1/2}} -$$

$$- \frac{\pi}{2^{5/2}a^{3/2}} \frac{\sinh \pi a^{1/2}/2^{1/2} + \sin \pi a^{1/2}/2^{1/2}}{\cosh \pi a^{1/2}/2^{1/2} - \cos \pi a^{1/2}/2^{1/2}}$$

where $a = 8t_0\nu/\pi.$

As it follows from this formula that

$$||F_Y(\nu)||^2_\nu = C_N \times \pi^4/96 \qquad \text{when} \quad \nu \ll \pi/8t_0$$

and $$||F_Y(\nu)||^2_\nu = C_N \times \frac{1}{2^7\pi^{1/2}t_0^{3/2}} \frac{1}{\nu^{3/2}} \qquad \text{when} \quad \nu \gg \pi/8t_0.$$

General case

Although the series of power spectrum

$$||F_Y(\nu)||^2_\nu \propto \sum_{k=1}^{\infty} \frac{[2k-(10-3\psi)/2(4-\psi)-\varepsilon_k/\pi]^{2\delta}}{(8t_0\nu/\pi)^2+[2k-(10-3\psi)/2(4-\psi)-\varepsilon_k/\pi]^4}$$

has to be calculated numerically the asymptotic form of PDS can be easily evaluated analytically:

$$||F_Y(\nu)||^2_\nu = C_N \times \mathcal{A}_L \qquad \text{when} \quad \nu \ll \pi/8t_0$$

$$||F_Y(\nu)||^2_\nu = C_N \times \frac{\mathcal{A}_H(\nu)}{\nu^{(3-2\delta)/2}} \qquad \text{when} \quad \nu \gg \pi/8t_0$$

where

$$\mathcal{A}_H(\nu) = \frac{1}{2(8t_0\pi)^{(3-2\delta)/2}} \int_{x_1(\nu)}^{\infty} \frac{x^{2\delta}dx}{1+x^4},$$

$$\alpha = \frac{3}{2} - \delta = \frac{16-5\psi}{2(4-\psi)} \quad \text{for} \quad \psi > 0$$

and $\alpha = 2 \quad \text{for} \quad \psi < 0.$

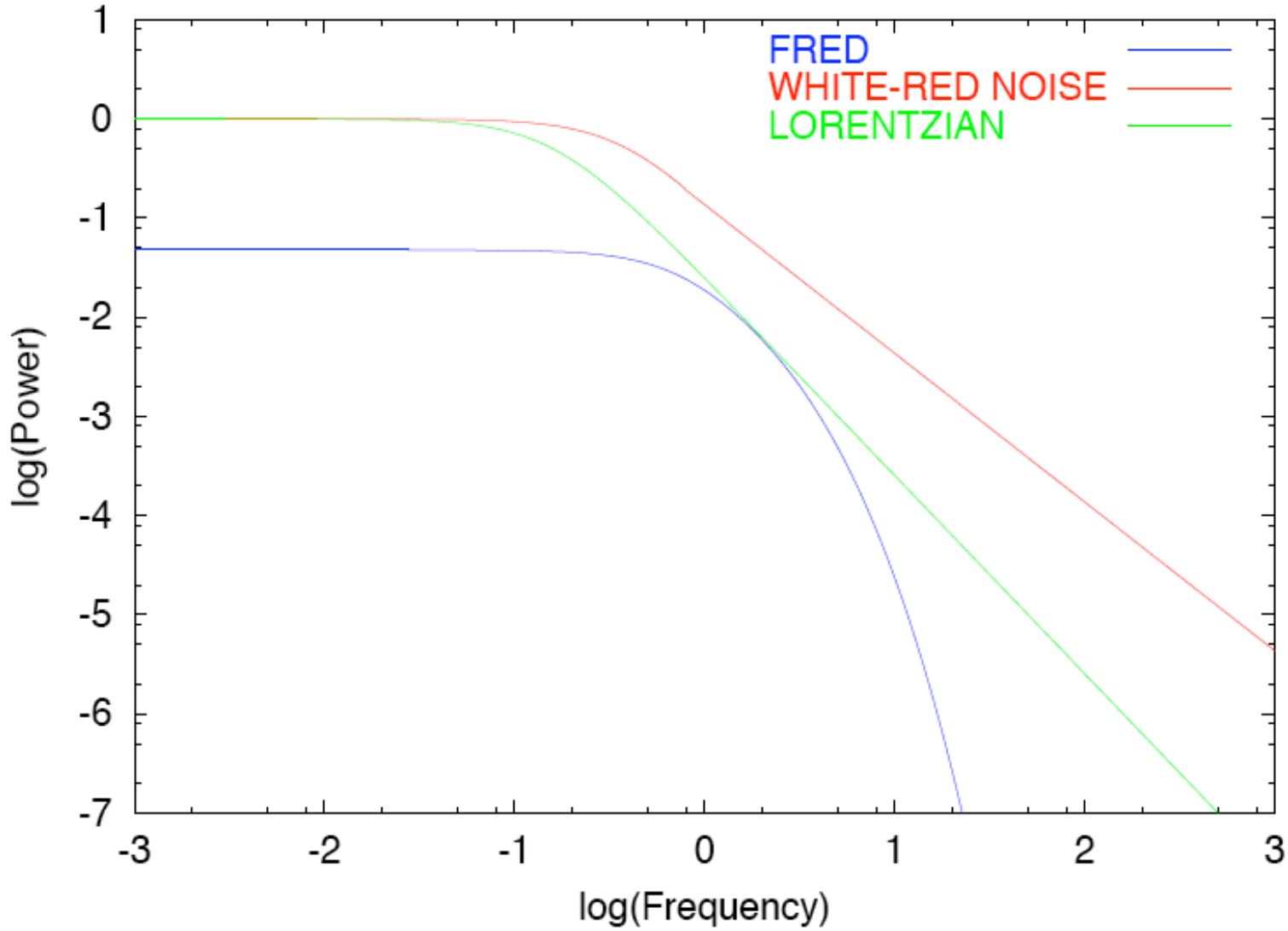

Fig. 1.— Examples of PDS models: PDS of fast rise and exponential decay (FRED) (blue line), PDS of white-red noise (red line) and Lorentzian PDS (green line).

Integrated Power of X-ray emission vs total integrated power of the disk configuration

We obtain that the integrated total power of X-ray resulting signal

$$P_x = \int_0^\infty ||F_x(\omega)||^2 d\omega \sim \frac{1}{D\mathcal{Q}} \frac{P_{dr}}{\omega_{dr} t_0}.$$

We arrive to the conclusion that the resulting integrated power P_x, which is related to the perturbation amplitude at the inner disk edge, is much less than the total integrated power of the driving oscillation in the disk P_{dr}

$$\frac{P_x}{P_{dr}} \sim (D\mathcal{Q}\omega_{dr} t_0)^{-1} \ll 1.$$

Evolution of Power density spectrum and energy spectrum

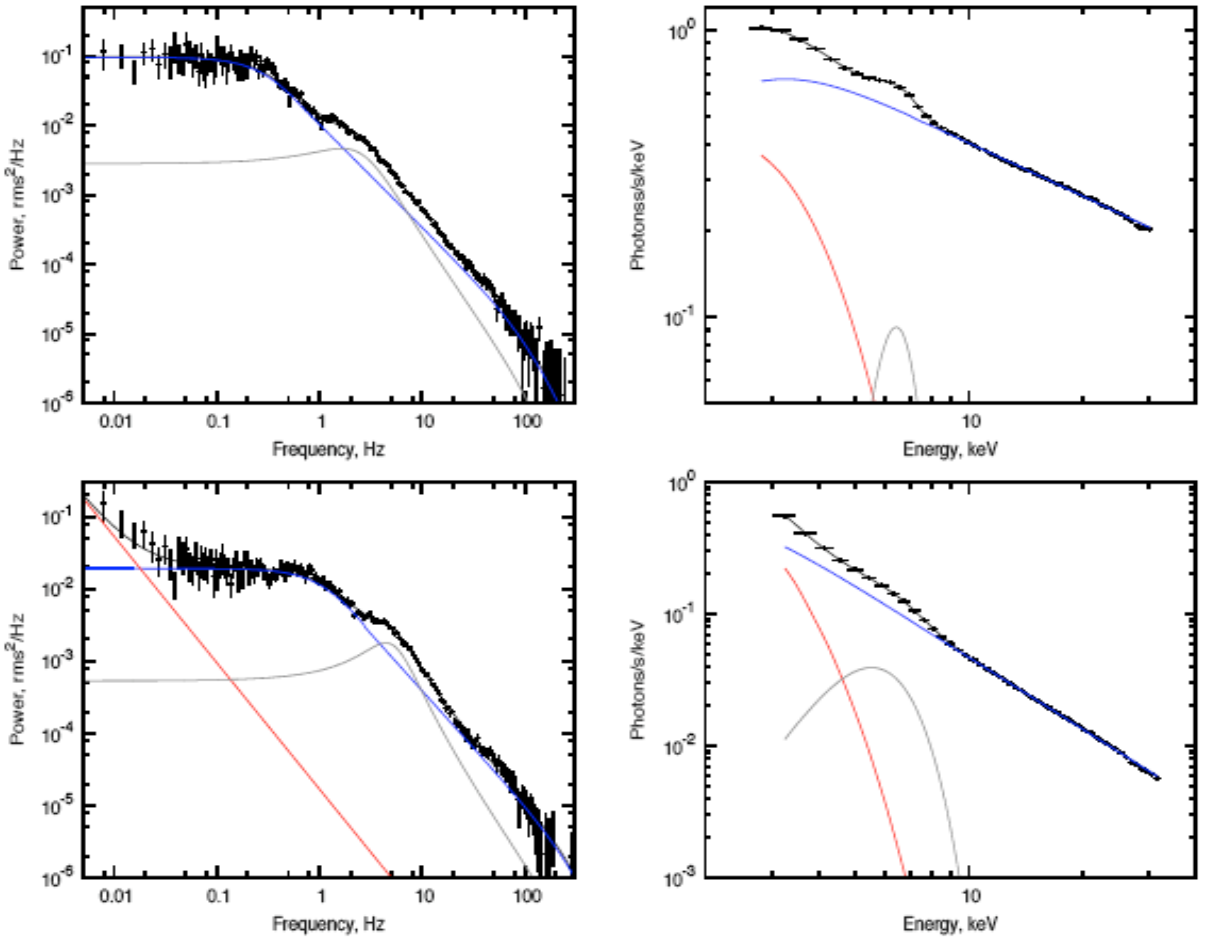

Cyg X-1: Observable power spectrum (PDS) (left panel) vs photon spectrum (right panel). The first observation is a pure low/hard state with no LF WRN component in the PDS. During the second observation the source energy spectrum is still hard, but LF WRN is already detectable.

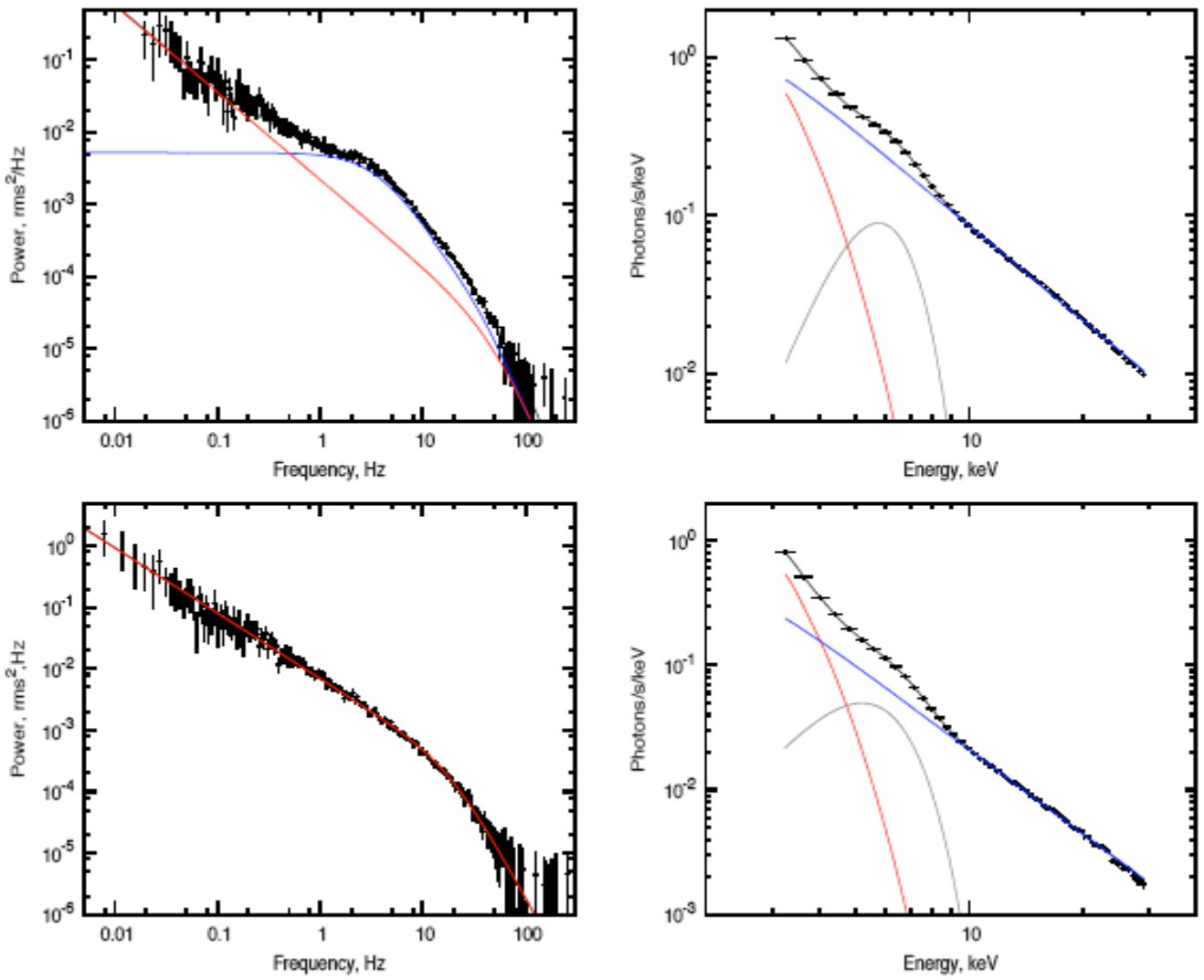

The first observation is taken during the intermediate state just before the transition to high/soft state, which is presented by the second observation.No HF WRN is present in PDS during high/soft state.

Power spectra of Cyg X-1: Hard and intermediate states

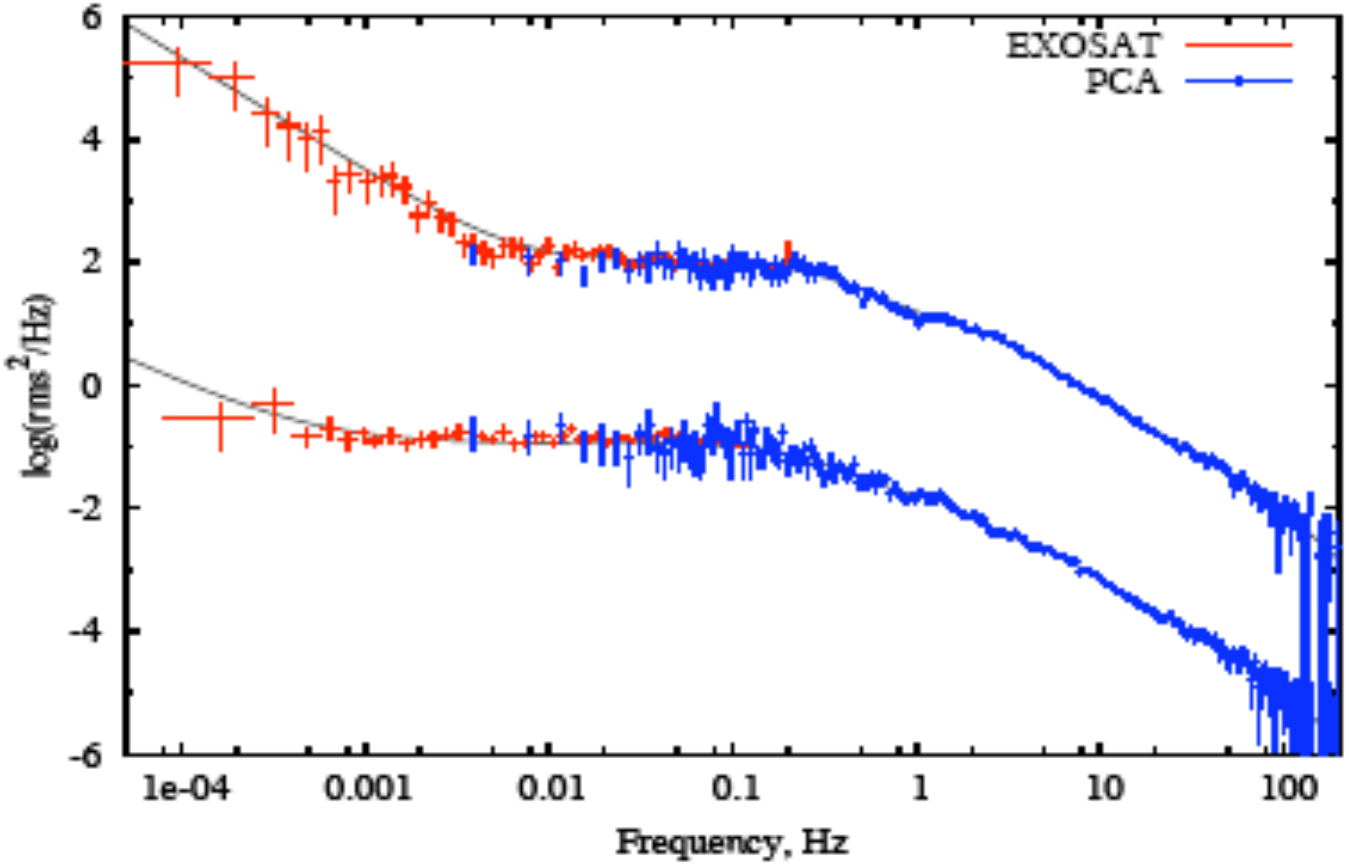

Two composite PDSs: EXOSAT spectra with matching high frequency PCA PDS. Data are fitted by LF-HF diffusion model:
χ_2/N_{dof} = 250.1/267 = 0.94, ψ_{corona} = 2.32 ± 0.12, $t_{0,C}$ = 1.8 ± 0.3, ψ_D = 2.5 and
χ_2/N_{dof} = 278.5/267 = 1.04, ψ_{corona} = 2.07 ± 0.7, $t_{0,C}$ = 1.24 ± 0.12, ψ_D= 0.3 ± 0.3.

Reynolds number of the flow and Shakura-Sunyaev disk - alpha parameter as observable quantities

Using the best-fit parameters of the PDS model we can infer the evolution of the physical parameters of the source such the disk diffusion time t_0, magnetoacoustic QPO frequency and Reynolds number of the accretion flow Re, with the change of photon index. We can relate t_0 with Re and magnetoacoustic QPO frequency ν_{MA}

$$t_0 = \frac{4}{3}\frac{4}{(4-\psi)^2}\left[\frac{V_{MA}R_0}{\hat{\nu}(R_0)}\right]\left(\frac{R_0}{V_{MA}}\right) = \frac{4}{3}\frac{4}{(4-\psi)^2}\frac{\mathrm{Re}}{a_{MA}\nu_{MA}},$$

because

$$\nu_{MA} = V_{MA}/(a_{MA}R_0)$$

These formulas leads to equation

$$\mathrm{Re} = a_{AM}\frac{3}{4}\frac{(4-\psi)^2}{4}(\nu_L t_0)$$

that allows us to infer a value of Re using the best-fit model parameters t_0 and the QPO low frequency ν_L presumably equals to ν_{MA} .

Determination of Reynolds number of accretion flow from Observations I

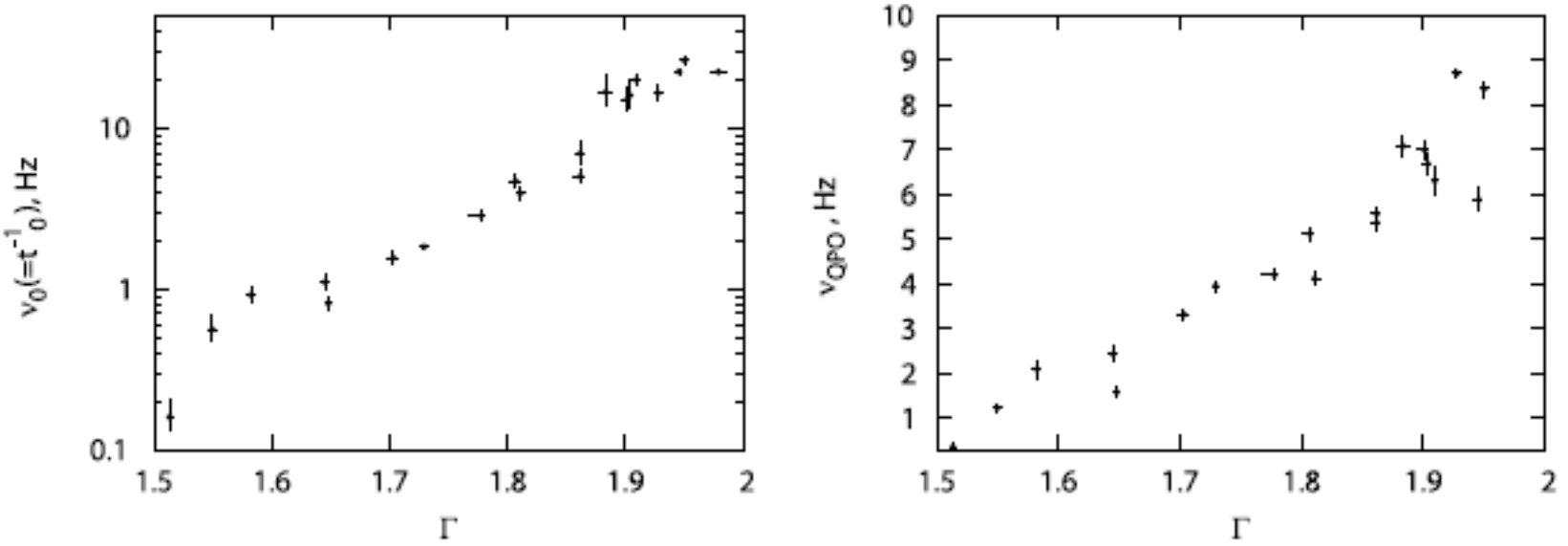

Fig. 8.— Cyg X-1: HF white-red noise component: the best-fit diffusion frequency $\nu_0 = t_0^{-1}$ vs Γ (upper left panel), QPO low frequency ν_{QPO} (ν_L) vs Γ (right upper panel)

T, Shaposhnikov & Arefiev 2007

Determination of Reynolds number of accretion flow from Observations II

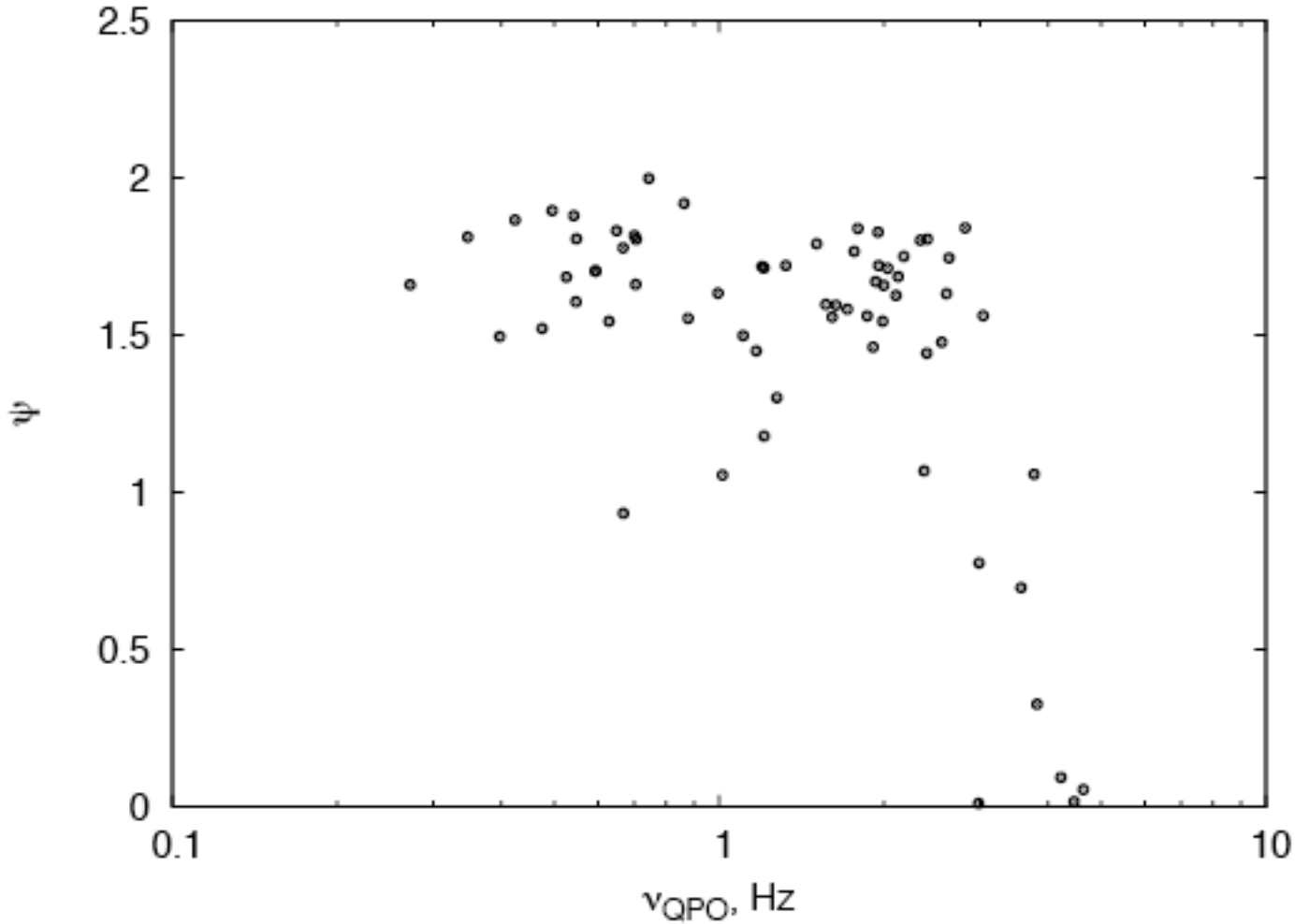

Determination of Reynolds number of accretion flow from Observations III

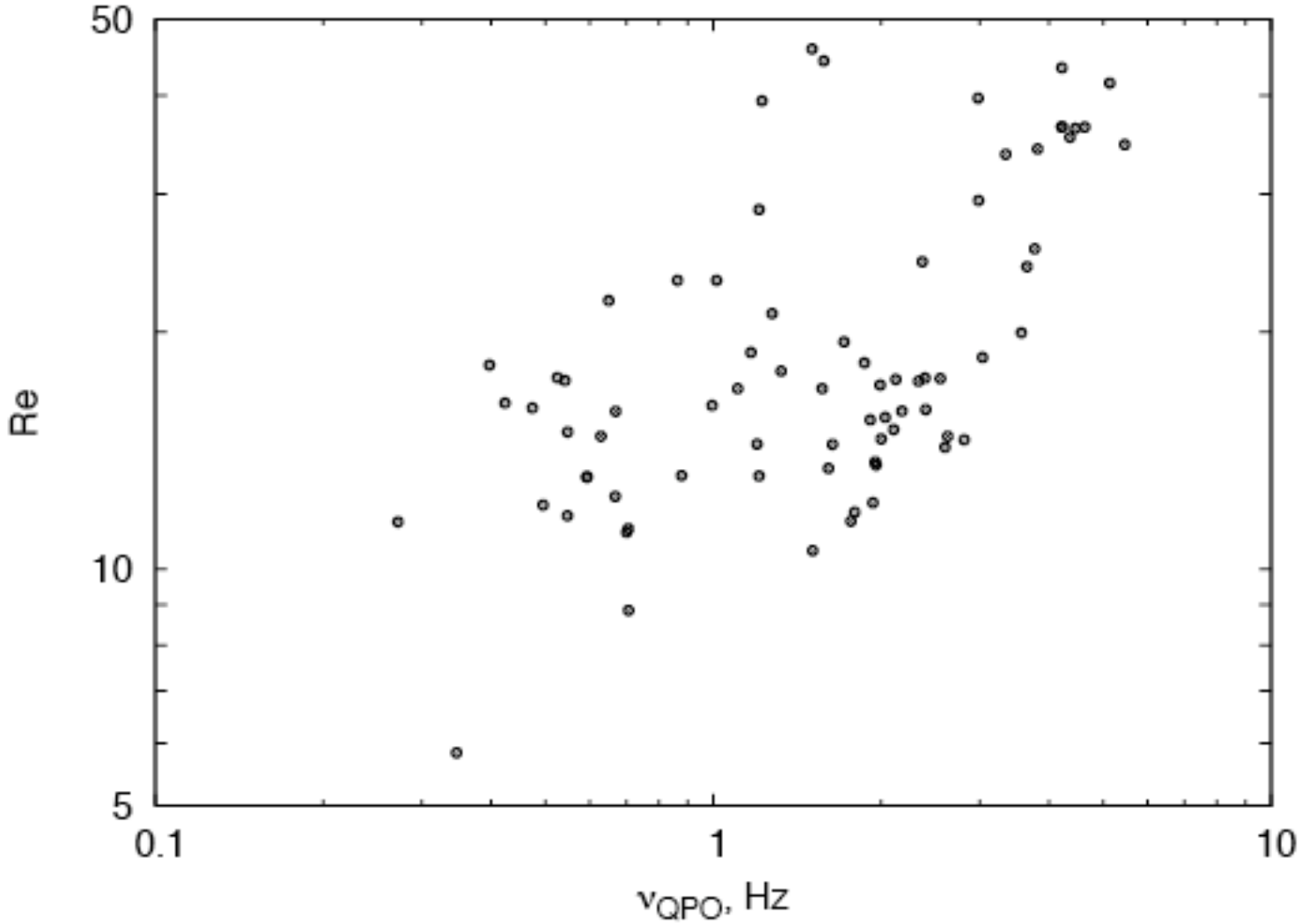

Observational Evidence of Compton Cloud Contraction

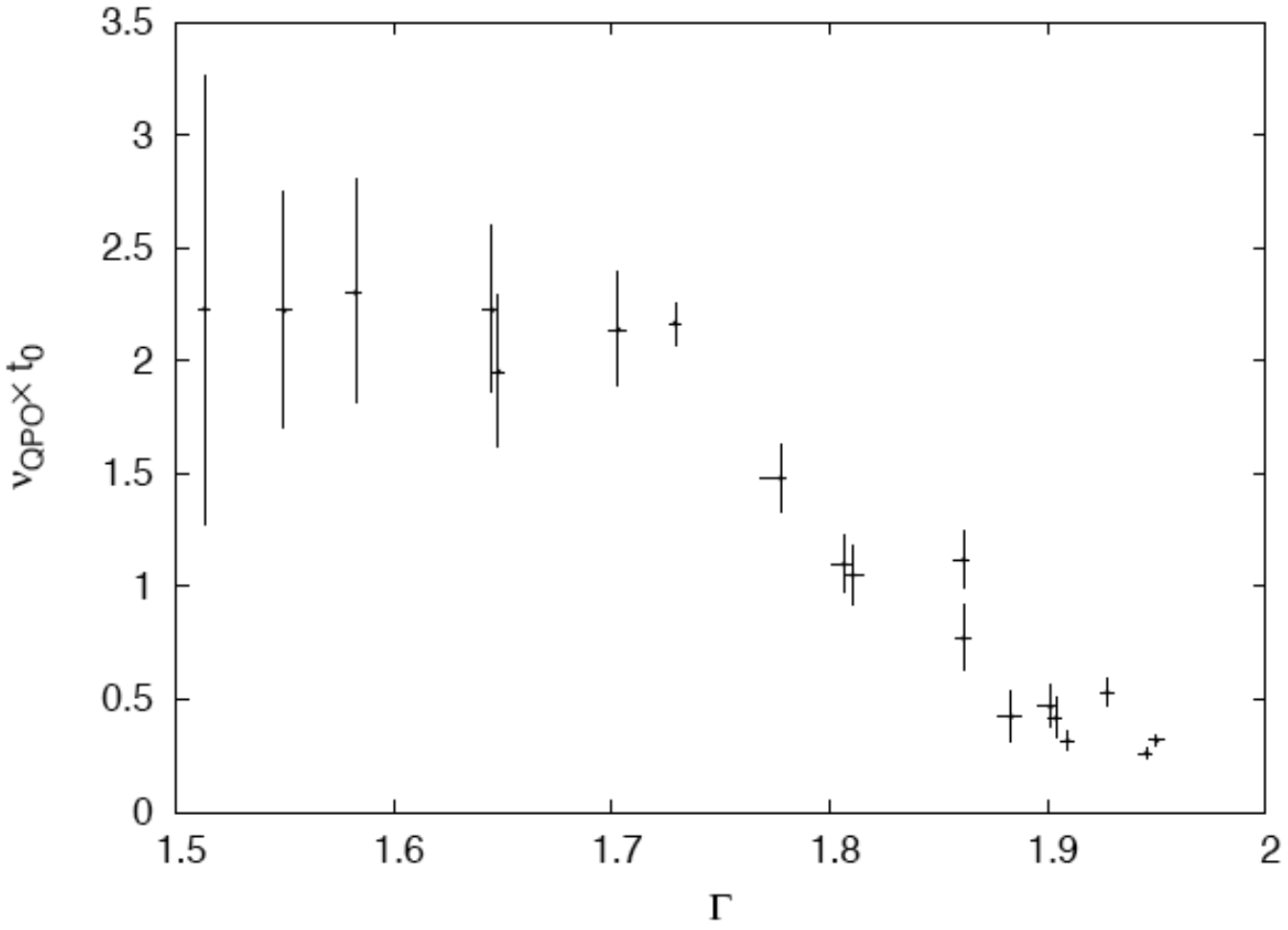

Cyg X-1: a product of QPO low frequency $\nu_{QPO}(\nu_L)$ and the best-fit diffusion time of HF WRN t_0 vs Γ. Decrease of $\nu_{QPO} \times t_0$ with Γ implies that Compton cloud contracts when the source evolves to the softer states.

Driving QPOs in the observed power spectra

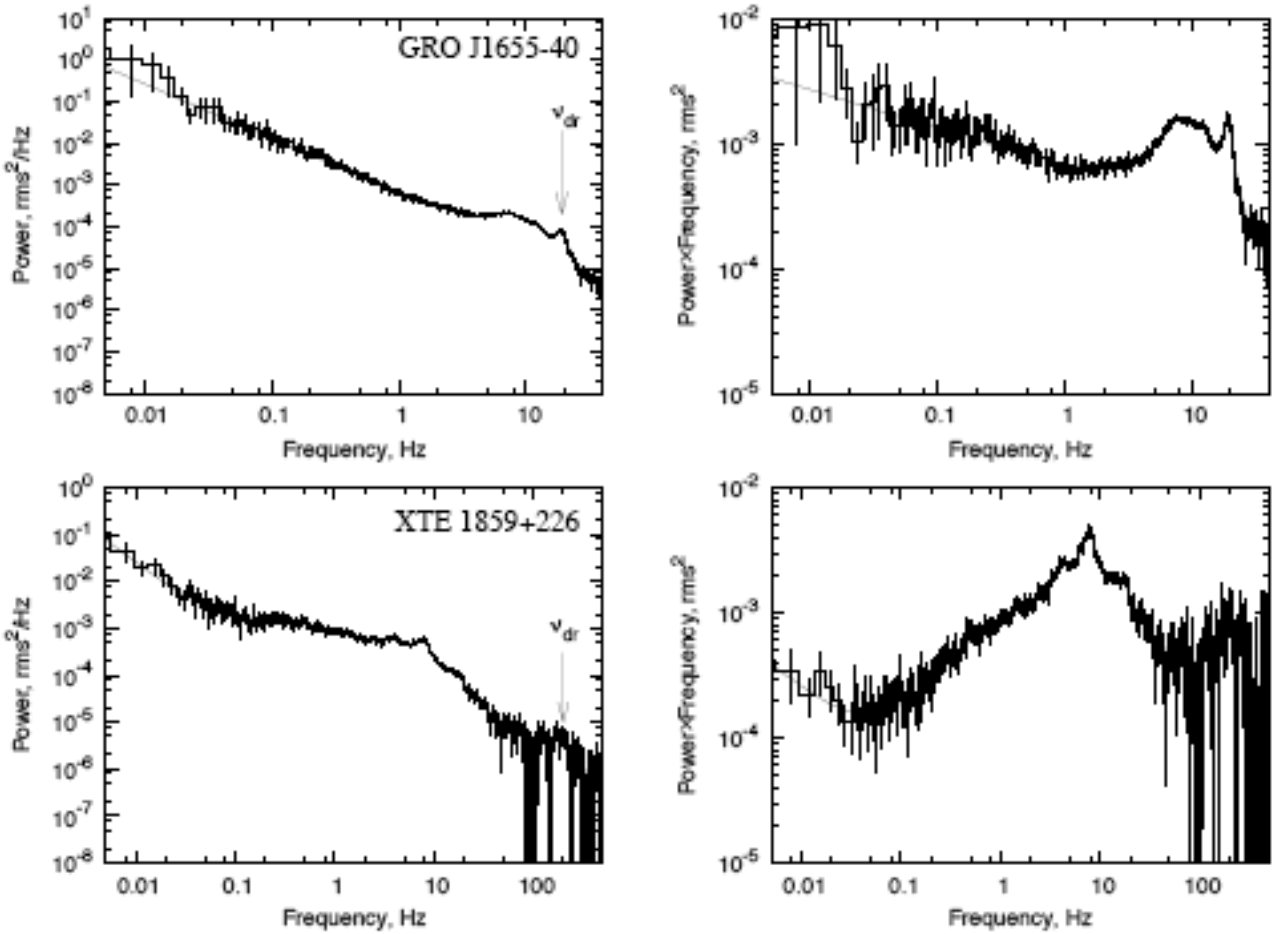

RXTE/PCA power spectra (left panels) and power×frequency diagrams (right panels) of GRO J1655-40 (top) and XTE 1859+226 (bottom). One can clearly see QPO frequencies dr at 10 – 20 Hz for GRO J1655-40 and 185 Hz for XTE 1859+226 before a high-frequency cut-off. The rms^2 power at ν_{dr} is comparable (GRO J1655-40) or higher (XTE 1859+226) than that at low frequencies (see right panels).

Power vs Driving QPO frequency

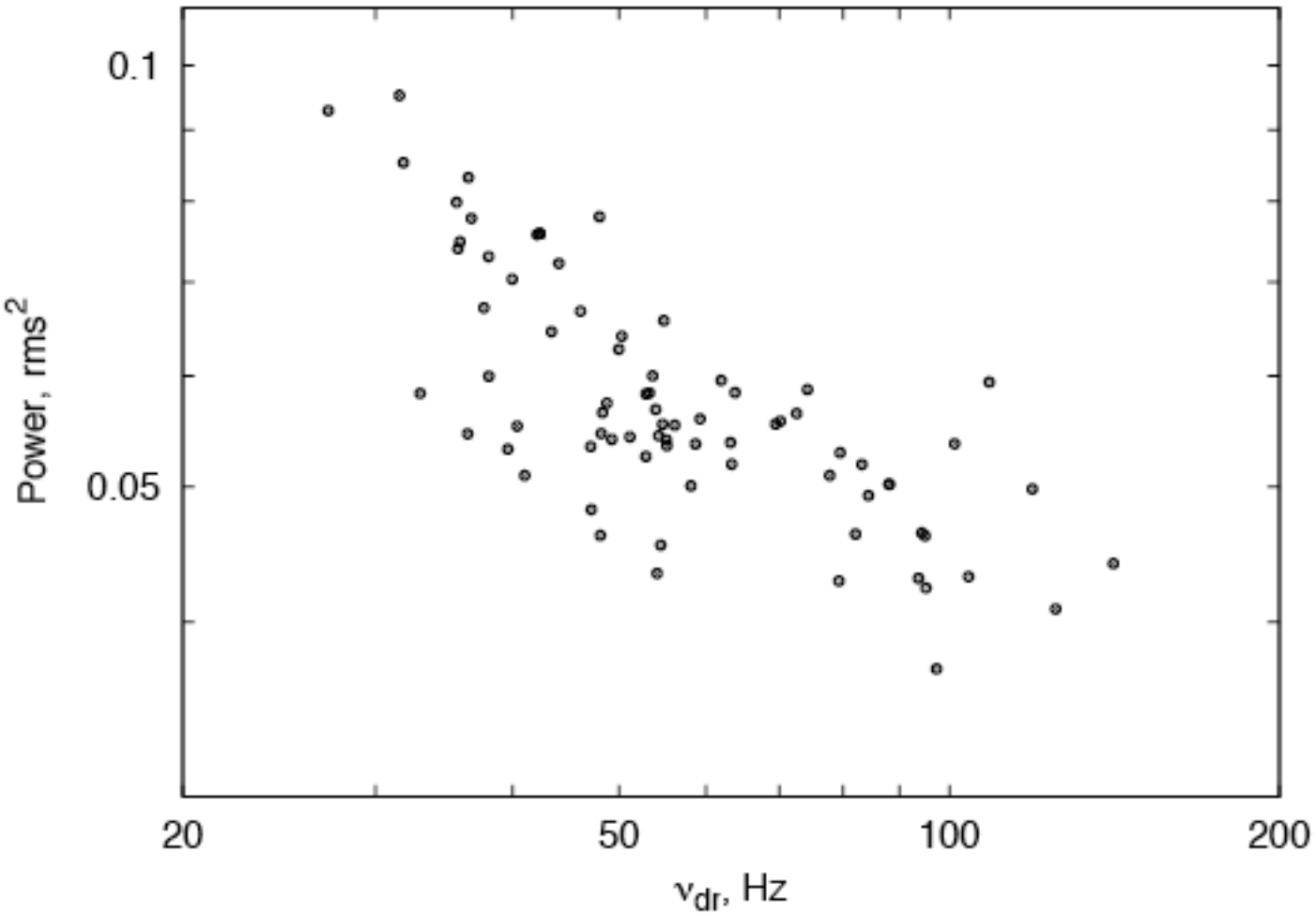

Low QPO frequency vs Driving QPO frequency

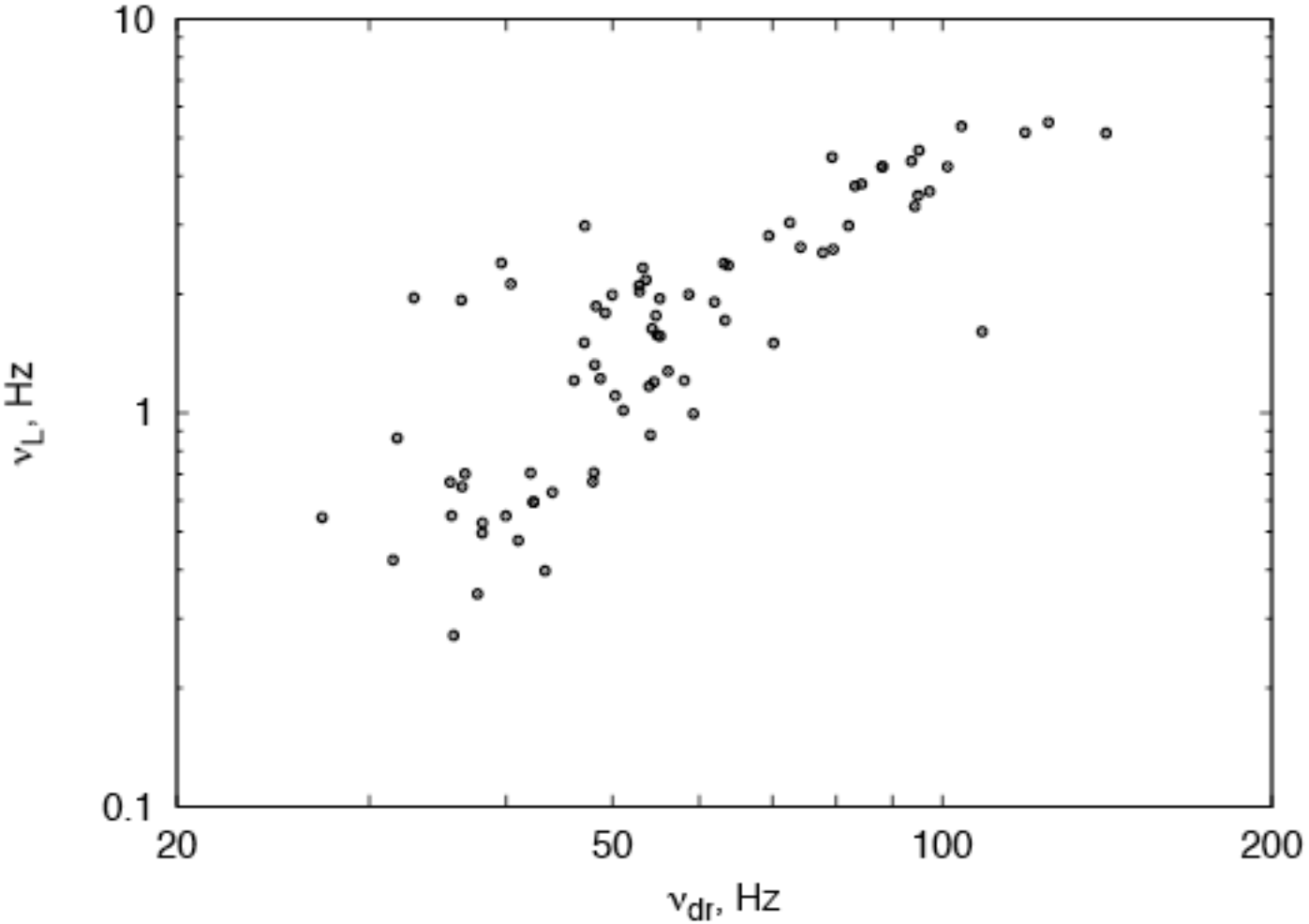

Summary I.

We present a model of Fourier Power Density Spectrum (PDS) formation in accretion powered X-ray binary systems derived from the first principles of the diffusion theory.

The resulting PDS continuum is a sum of two components, a low frequency (LF) component is presumably originated in an extended accretion disk and a high frequency (HF) component is originated in the innermost part of the source (Compton cloud).

Summary II.

The LF PDS component has a power law shape with index about 1.5 at higher frequencies ("red" noise) and a flat spectrum below a characteristic (break) frequency ("white" noise).

This white-red noise (WRN) continuum spectrum holds information about physical parameters of bounded extended medium, diffusion time scale and dependence of viscosity vs radius.

We offer a method to measure an effective Reynolds number, Re using the basic PDS parameters (PDS index and characteristic frequencies).
We obtain that the inferred Re increases from 8 in low/hard state to 70 high/soft state.

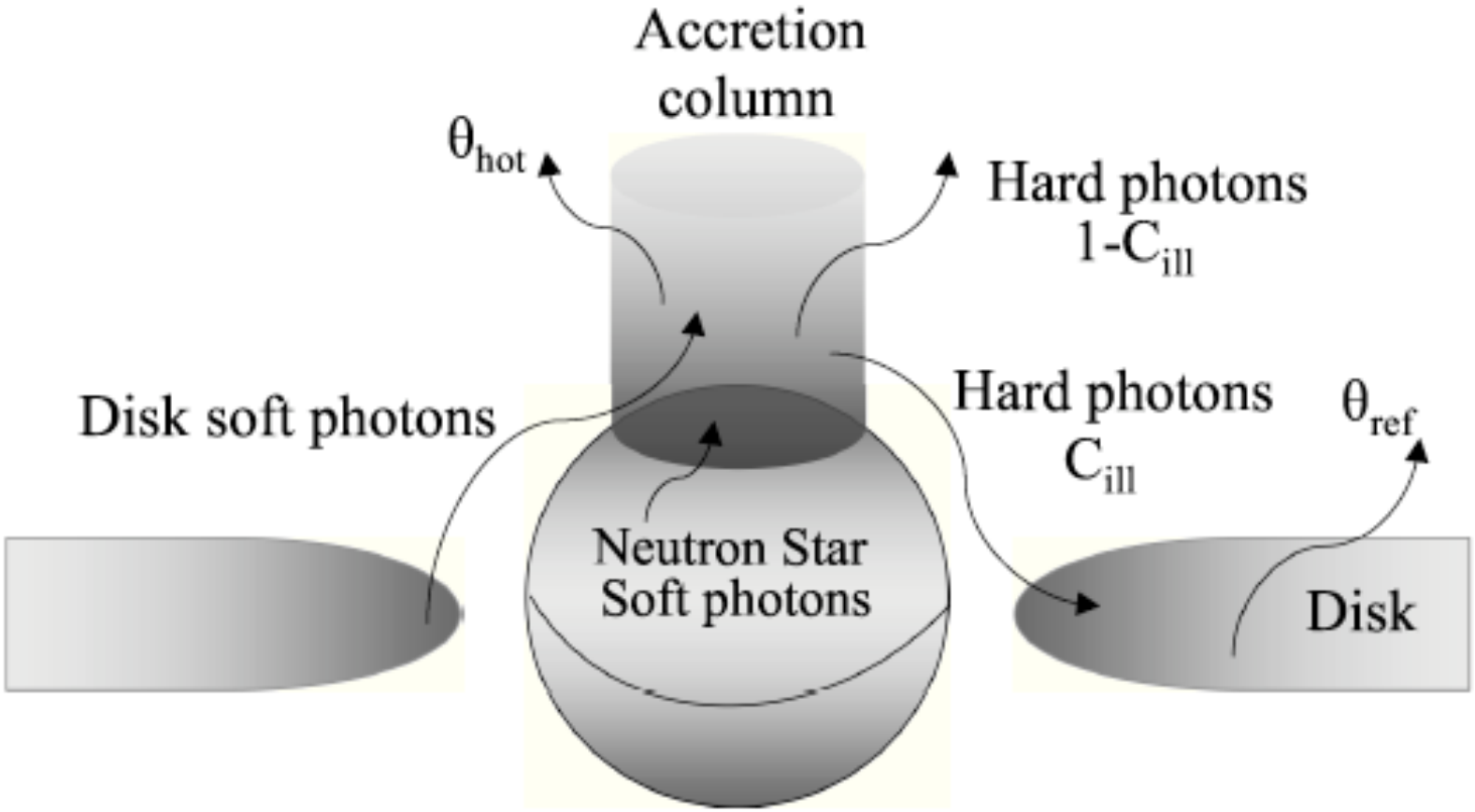

This cartoon illustrates the different emission patterns responsible for the time lags of the pulsed emission. Cill is the disk illumination fraction. Soft time lag of the pulsed emission is the result of downscattering of hard X-ray photons in the relative cold plasma of the disk. A fraction of hard X-ray photons 1- Cill that are upscattered soft disk photons coming from the disk and NS and directly are seen by the Earth Observer.

Time lags and density variations in compact objects

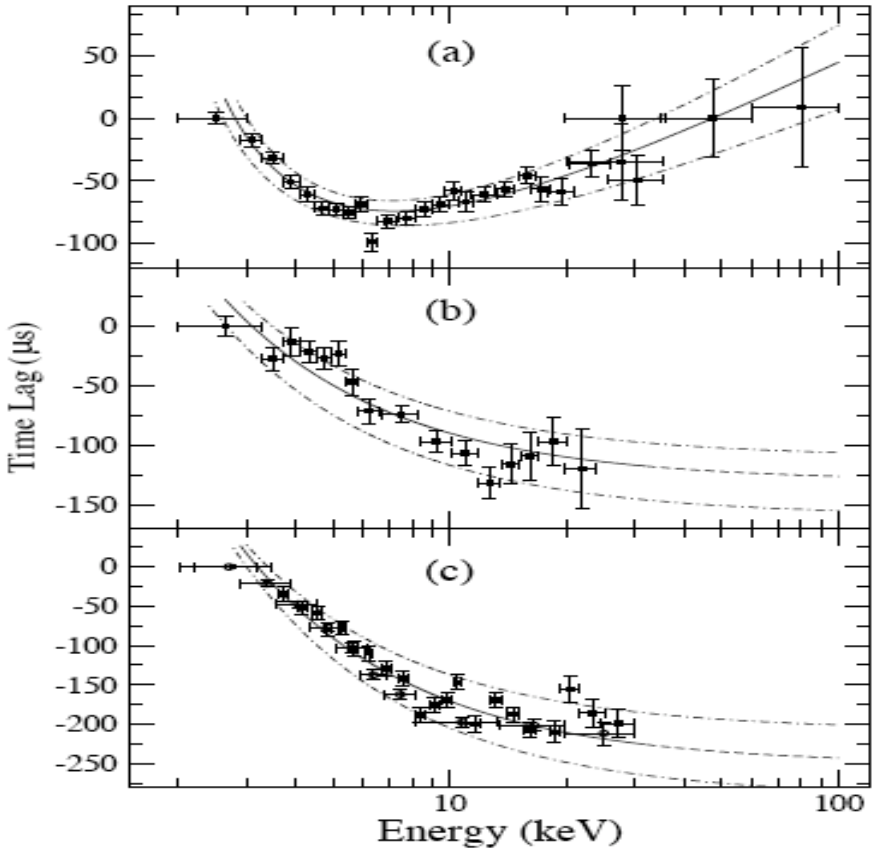

The measured soft time lag of the pulse profile versus energy (crosses) with respect to the first energy channel. The best- fit curve using the Comptonization model is shown with the solid line. The upper and lower limit of the electron number density of the Comptonization emission area, are given in dot-dashed line 1.6-2.6 x 10^{18} cm^{-3} . The panels corresponds (a) for IGR J00291+5934 including also the upper and lower limit of the electron number density of the reflector, 6.1-8 x 10^{18} cm^{-3}, and (b) that for XTE J1751-305, 6-6.6 x 10^{18} cm^{-3} and (c) that for SAX J1808.4-3658, 2.9-3.6 x 10^{18} cm^{-3}.

Time lag model

$$\Delta t = -\frac{C_{\rm ill}}{\sigma_{\rm T} n_{\rm e}^{\rm ref} c} \times$$

$$\left[\frac{1}{4\theta_{\rm ref}} \ln \frac{1 - 4\theta_{\rm ref}/z}{1 - 4\theta_{\rm ref}/z_*} - \frac{n_{\rm e}^{\rm ref}}{n_{\rm e}^{\rm hot}} \frac{1 - C_{\rm ill}}{C_{\rm ill}} \frac{\ln(z/z_*)}{\ln[1 + (3+\alpha)\theta_{\rm hot}]} \right] \quad (5)$$

where $n_{\rm e}^{\rm ref}$ is the electron number density of the reflector, $n_e^{\rm hot}$ is the electron number density of the Comptonization emission area (accretion column). $\theta_{\rm ref} = kT_e^{\rm ref}/(m_e c^2)$ is a dimensionless temperature of the reflector. We assume a typical value of $\theta_{\rm ref} < 0.7$ keV/511 keV. $kT_{\rm e}^{\rm hot}$ and α are the best-fit parameters for the hot plasma temperature and spectral index of the Comptonization spectrum, and $\theta_{\rm hot} = kT_e^{\rm hot}/(m_e c^2)$.

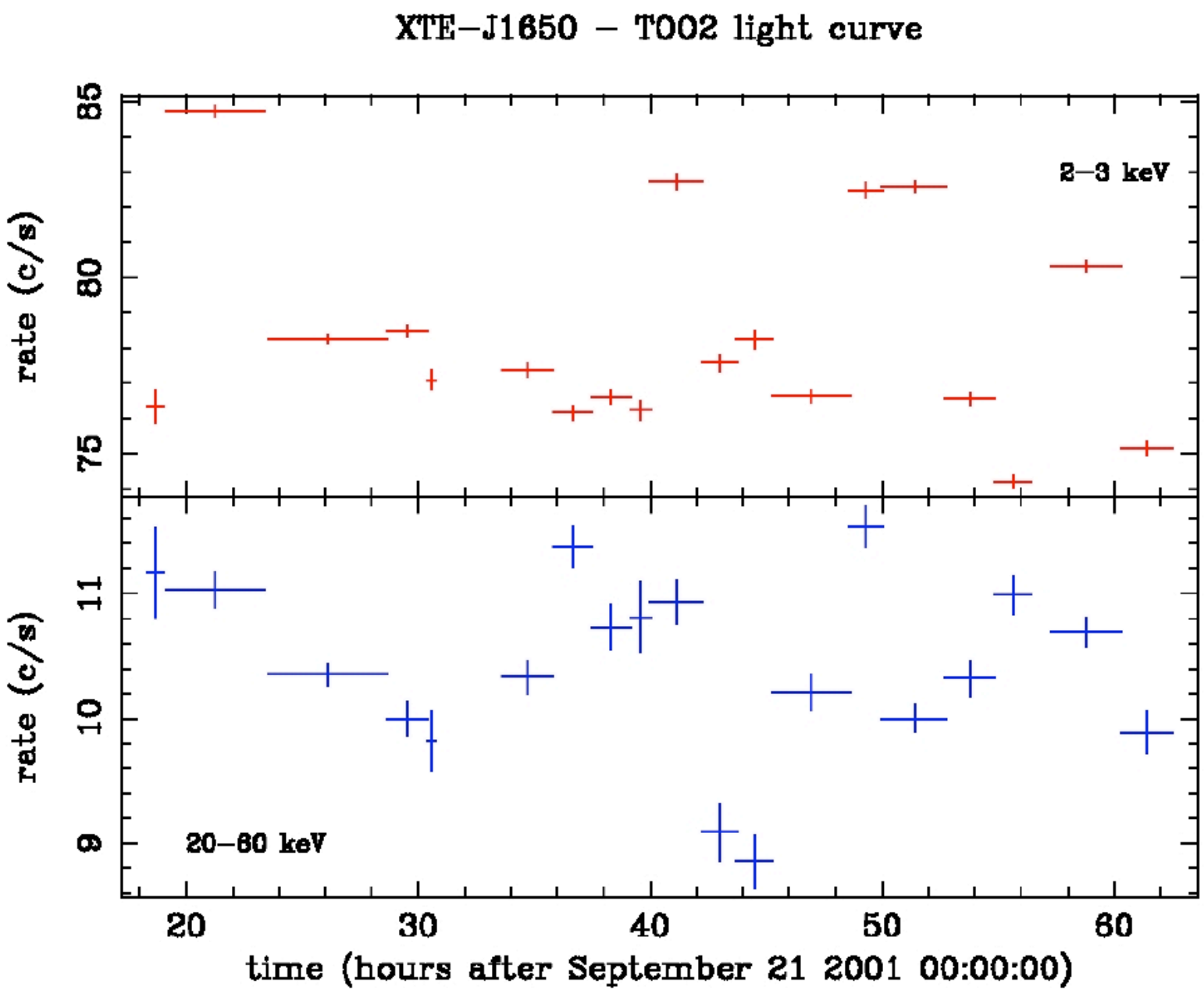
XTE−J1650 − T002 light curve
rate (c/s)
85
80
75
2−3 keV
rate (c/s)
11
10
9
20−60 keV
20
30
40
50
60
time (hours after September 21 2001 00:00:00)

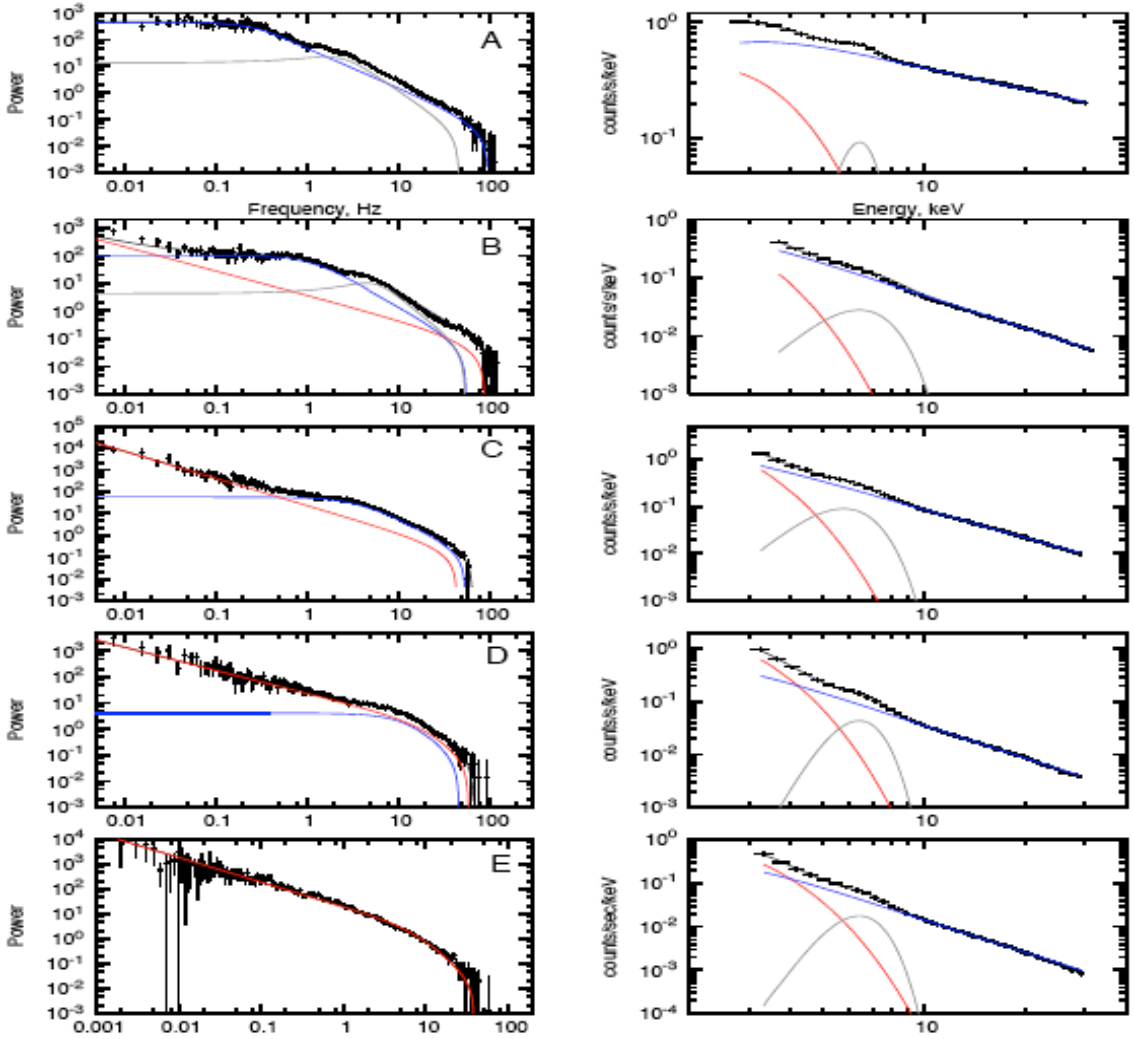

Fig. 2.— Cyg X-1: Observable power spectrum (PDS) (left panel) vs photon spectrum (right panel) from low/hard to soft state of Cyg X-1. Data points are shown with error bars. PDS is fitted by a product of sum of LF and HF white-red noise power spectra and Lorentzian (see formula 67). We also use Lorentzians to fit QPO features. Black line is for the resulting PDS as red and blue lines present LF and HF components respectively. Photon spectrum is fitted by BMC+GAUSSIAN model. Black line is for the resulting spectrum as red and blue lines present BMC blackbody and Comptonization components respectively. Grey line presents GAUSSIAN of K_α line located at 6.4 keV.

W01 demonstrated that the mass accretion rate in the disk $\dot{M}$ *can be calculated as*

$$\dot{M} = 3\pi \frac{\partial V}{\partial x}.$$

Furthermore, we assume that the mass accretion rate at the inner disk edge is converted with efficiency ε_{eff} *into the X-ray luminosity, L(t) i.e.*

$$L(t) = \varepsilon_{\text{eff}} \dot{M}(t, R_{in})$$

and thus

$$X(t) = L(t) \propto \frac{\partial V}{\partial x}(t, 0).$$

Now we consider a general case of problems where $\hat{\nu}(x) = (\hat{\nu}_0 / x_0^{\psi}) x^{\psi}.$

a. Viscosity linearly distributed over radius: $\psi = 2$

$$X(t) \propto \sum_{k=1}^{\infty} \exp[-\pi^2 (2k-1)^2 t / 4t_0]$$

where the viscous time scale $t_0 = 4x_0^4 / 3\hat{\nu}_0 = 4R_0^2 / 3\hat{\nu}(R_0).$

Then the power spectrum of X(t) is:

$$||F_X(\nu)||^2 \propto \sum_{k=0}^{\infty} \frac{1}{(8t_0\nu/\pi)^2 + (2k+1)^4}$$

where $F_X(\omega) = \int_0^{\infty} e^{-i\omega t} X(t) dt$

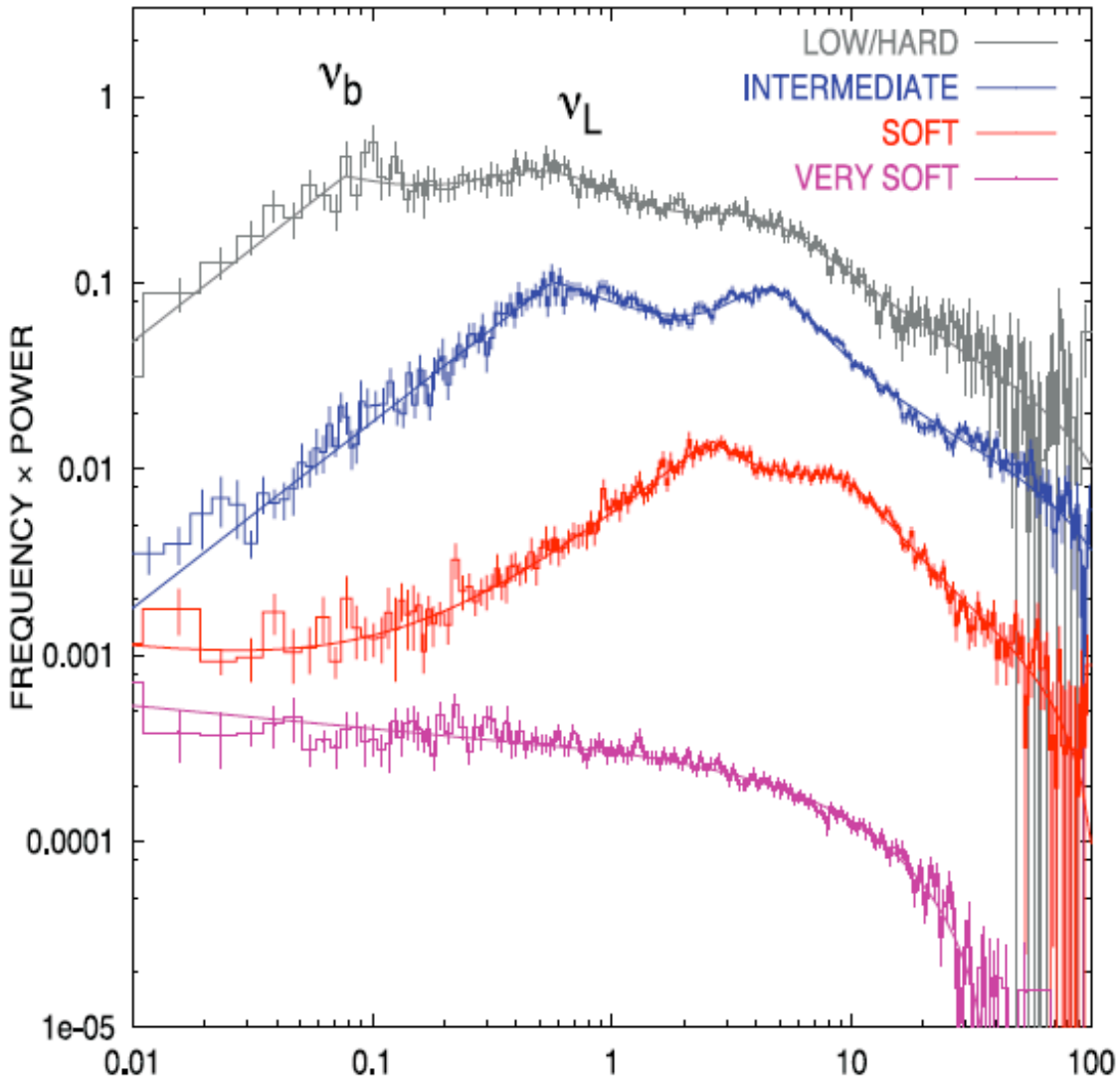

Shaposhnikov & T (2006)

FIG. 6.—Power spectrum (PDS) evolution of the source from the low/hard state (*gray lines*) through the intermediate state (*blue lines*) and soft state (*red lines*) to the very soft state (*purple lines*). The break frequency ν_b and the low QPO frequency are clearly seen in the low/hard, intermediate, and soft states. In the very soft state the power spectrum is featureless; neither QPO nor break are present. Any break and QPO features are washed out.

PDS for different energy ranges for TOO1

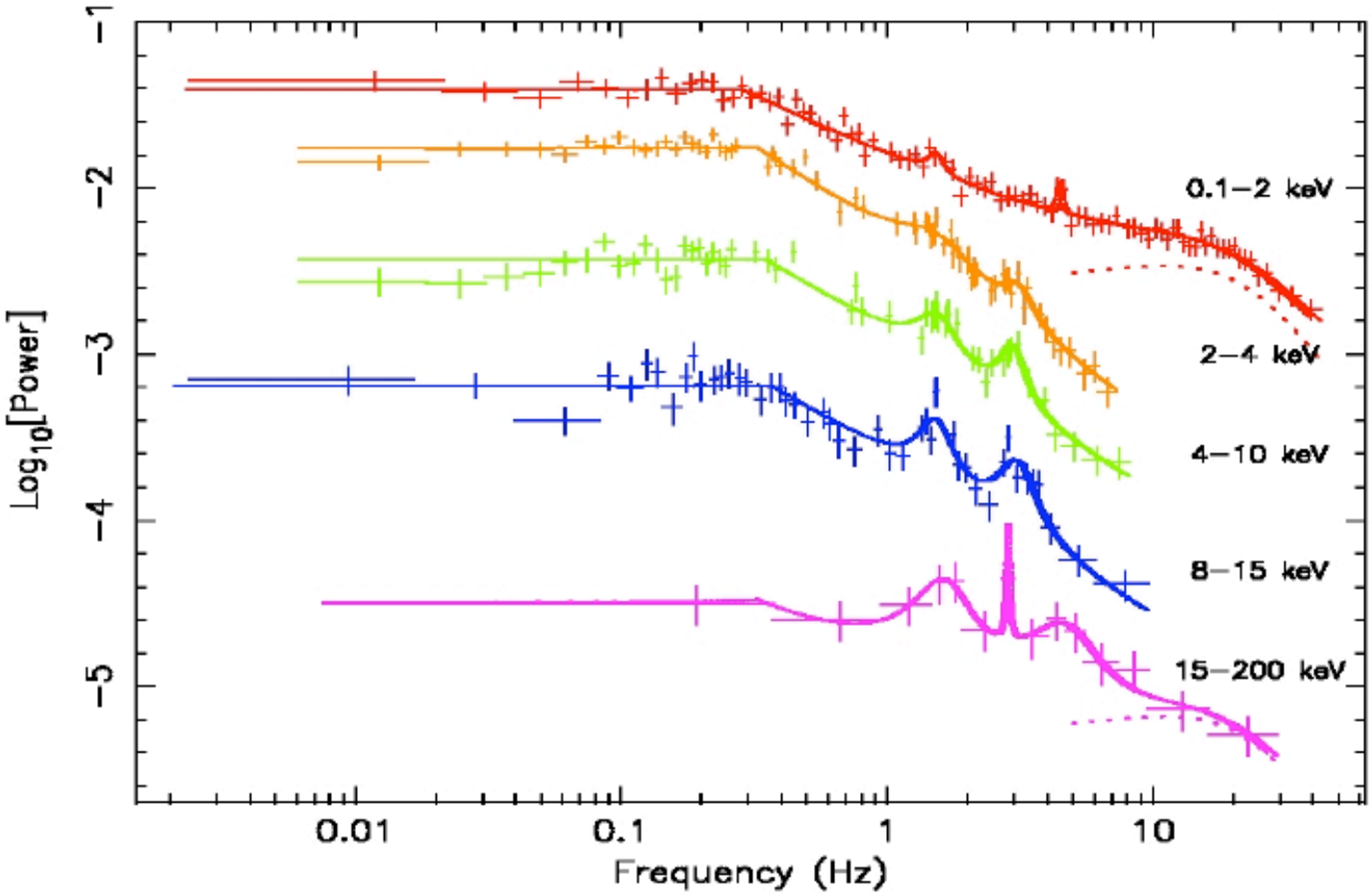

Montanari, T & Frontera 2006

BH mass determination:Cyg X-1

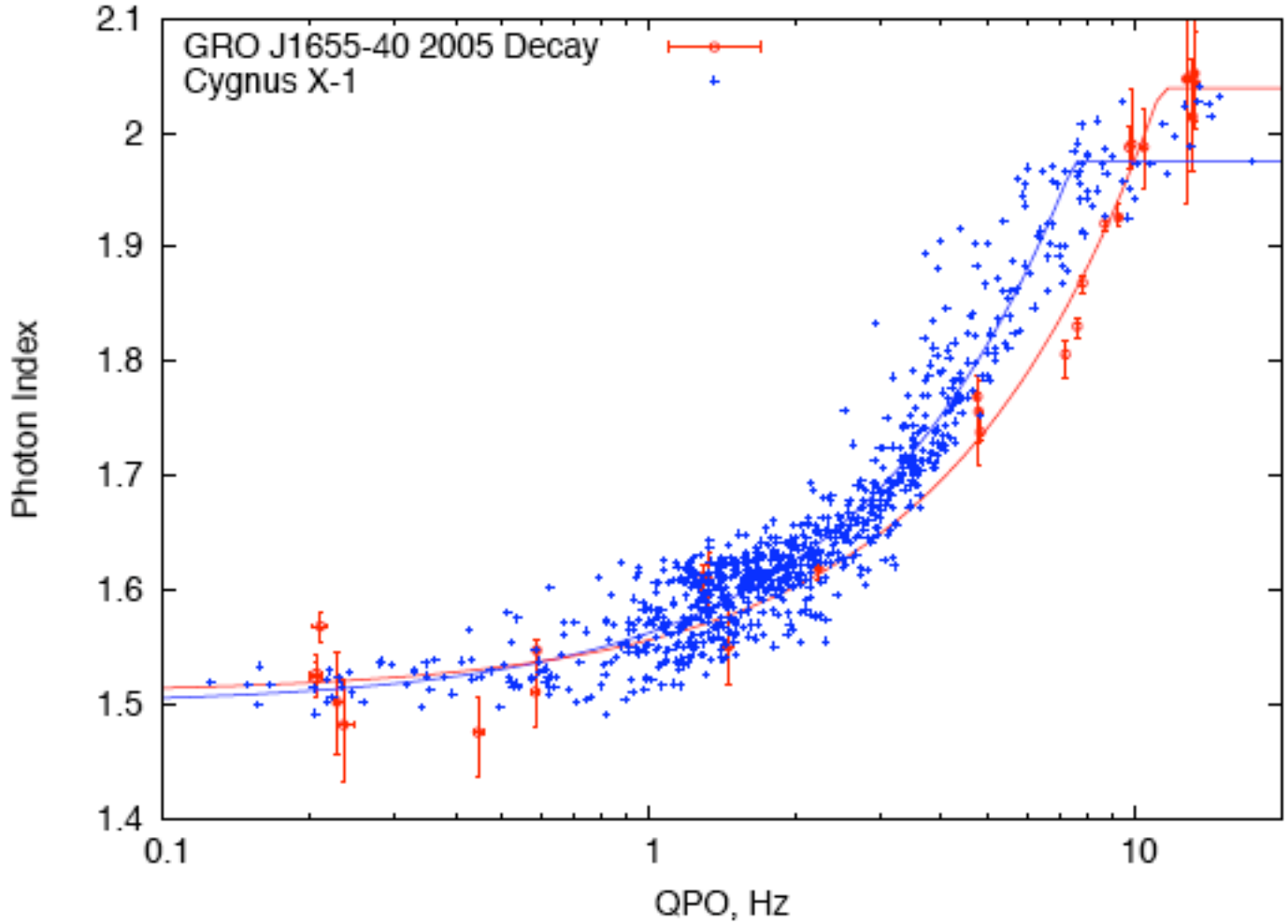

Fig. 2.— Determination of BH mass in Cyg X-1. Correlations for Cyg X-1 comprises RXTE-mission-long data from ST06 (blue color). Data for GRO 1655-40 is for the 2005 outburst decay. The sources show similar saturation levels for both ends of correlation. Index-QPO correlation scaling gives for the BH mass in Cyg X-1 $M_{CygX-1} = 8.5 \pm 1.2\, M_{\odot}$.

BH Candidate: GX 339-4

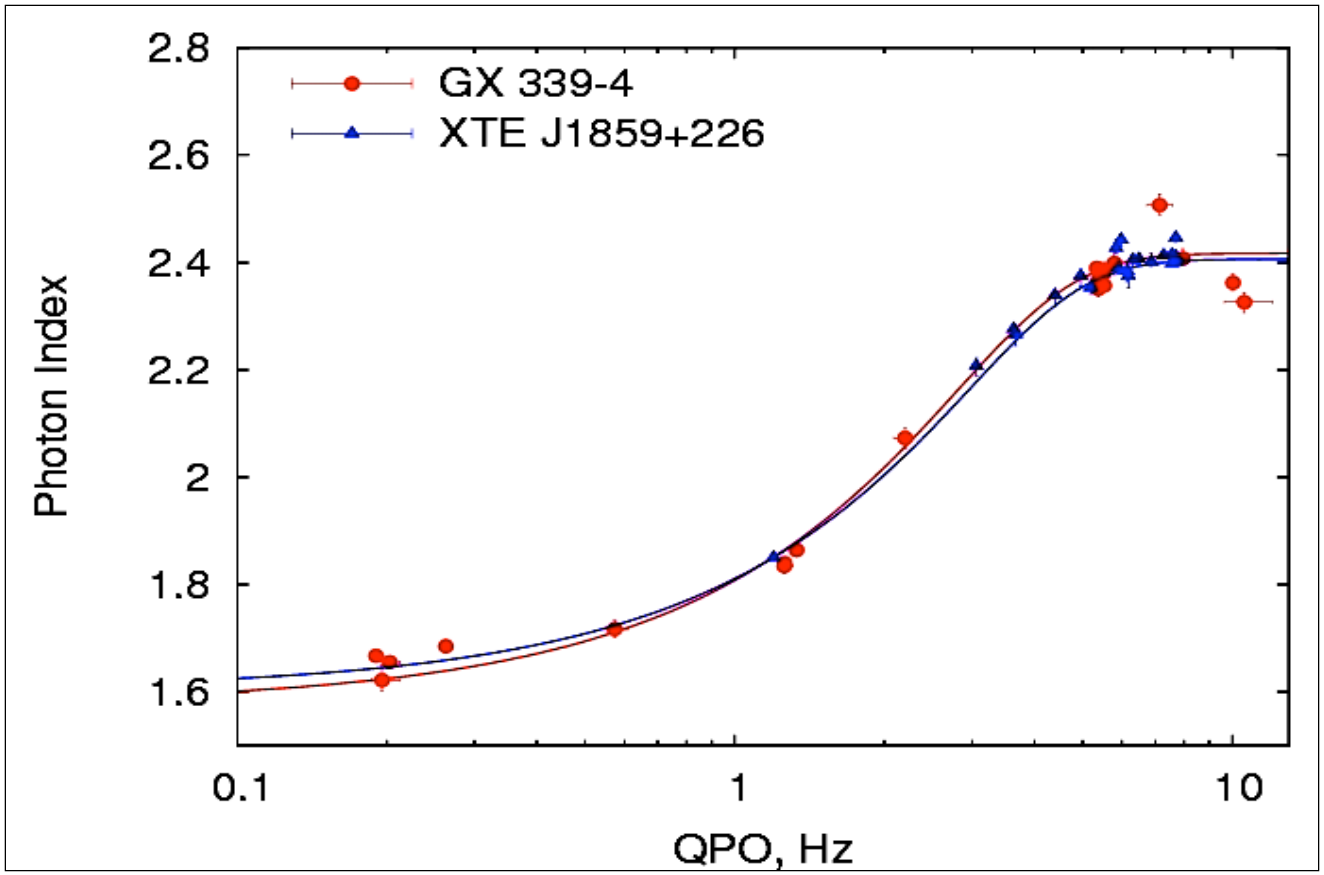

$M_{GX\ 339\text{-}4} \approx M_{XTE\ J1859+226} \sim (9.7 \pm 0.8)\ M_{SUN}$

QPO-Photon Index Correlations in BH sources

Cygnus X-1

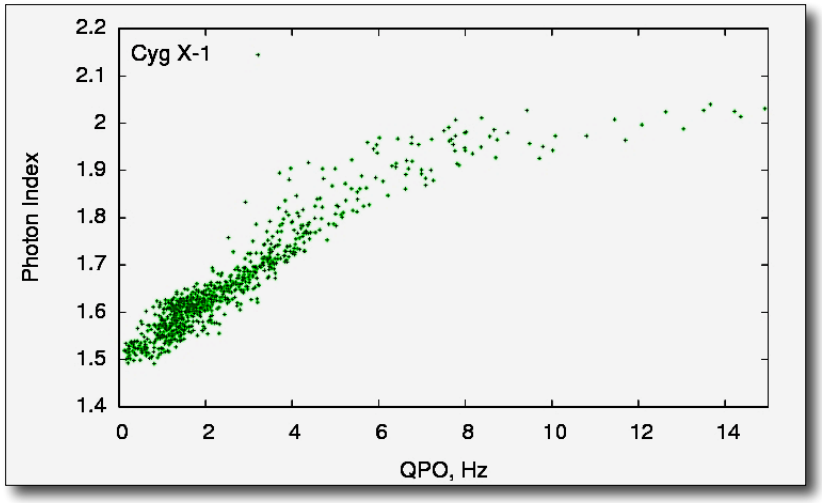

GRS 1915+105

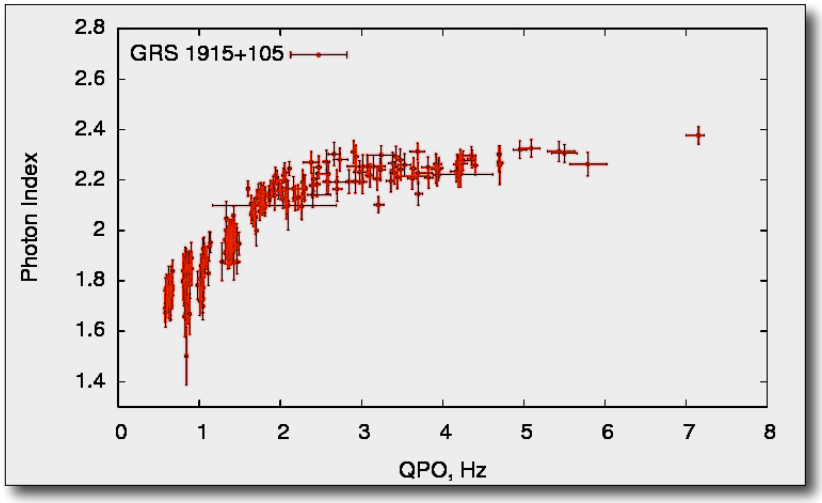

J1859+226 and 1550+564

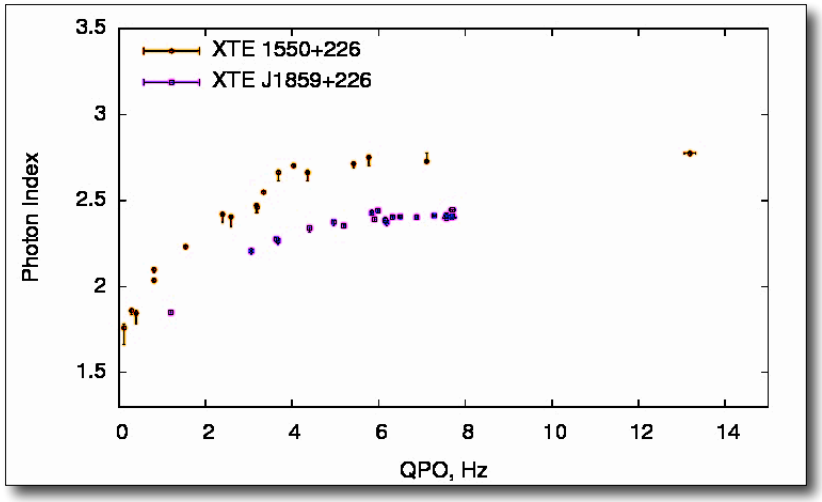

GRO J1655-40

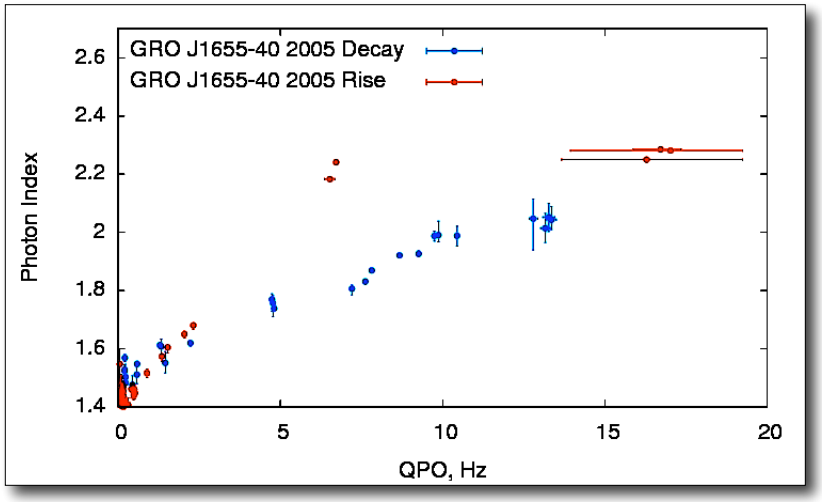

Index-Mdot saturation. GRS 1915+105

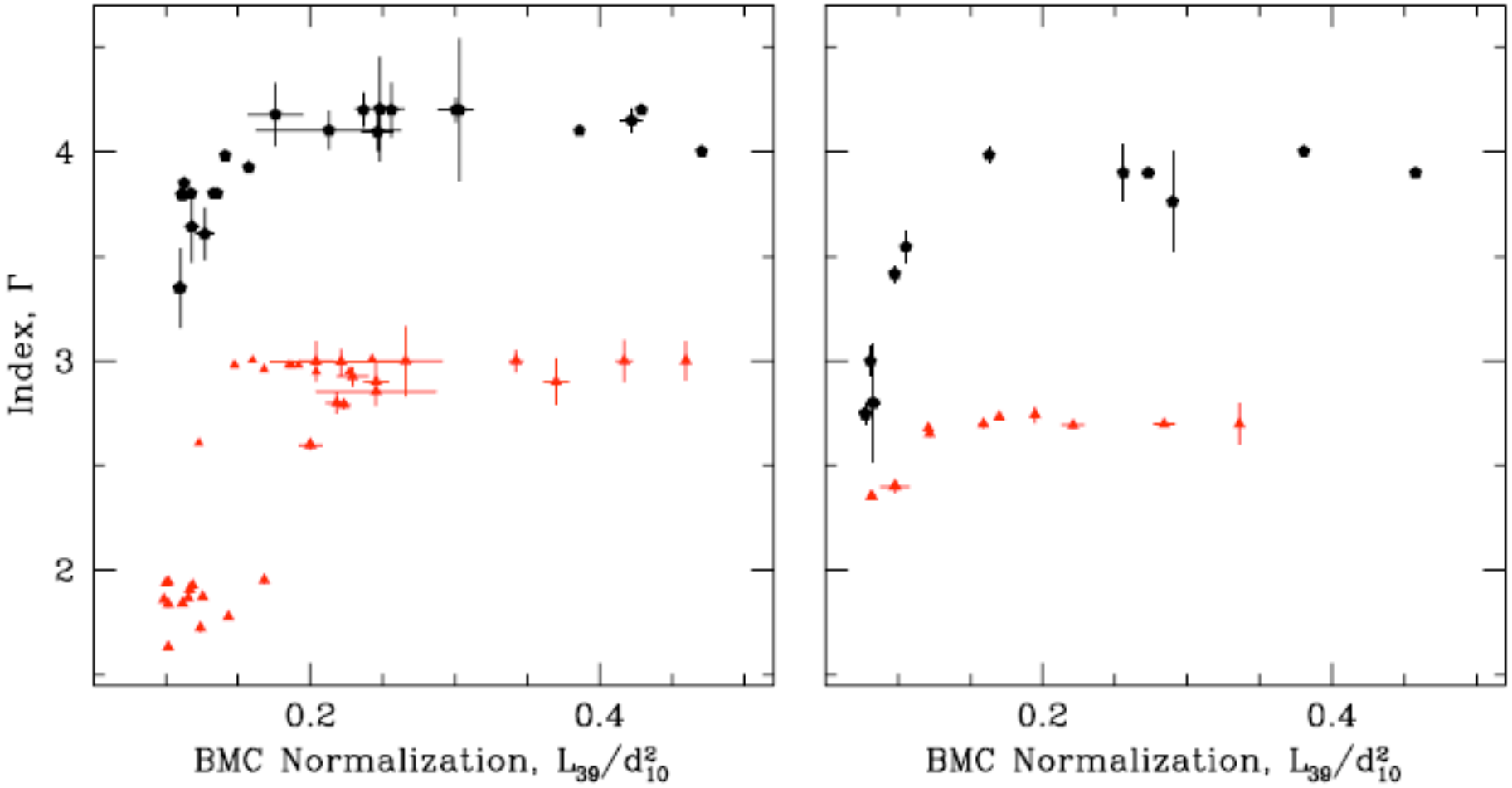

Seifina & T (2009)